Studies of Laser Cooled Calcium Ions in the Penning and Combined Traps

Jake Sudbery

A thesis submitted for the degree of Doctor of Philosophy

Imperial College of Science Technology and Medicine

March 18, 2003

Abstract

This thesis details work performed on trapping and laser cooling calcium ions in a Penning trap. Only two species of ion (beryllium and magnesium) have previously been laser cooled in a Penning trap. Singly charged calcium ions have a significantly different level structure to these two ions, but are similar to the heavier alkaline earth elements often used for frequency standards applications and quantum information processing in an rf trap. Laser cooling of calcium in the Penning trap requires the use of a novel laser scheme involving two cooling lasers.

Long term motivation of the work is discussed, with reference to quantum information processing. A brief literature review is also presented with an introduction to ion traps and their place within quantum information processing. Results are presented from the computer simulation of laser cooling in the four and two level atomic systems. This work uses the rate equation approach, iterating over discrete time steps to model the laser cooling. The novel aspects of laser cooling calcium (a four level system) are discussed with reference to the use of two cooling lasers.

Experimental work on setting up a Paul trap to laser cool calcium is discussed. New work on laser cooling calcium in a combined rf/Penning trap is presented. This is studied as a novel system in itself and as a stepping-stone to the full Penning trap. Trapping and cooling in the Penning trap itself is demonstrated. Finally, work on stabilising a Ti:sapphire laser using the Pound Drever Hall method is presented. Future work is discussed, including the use of this laser for sideband cooling and addressing the narrow qubit transition.

For my parents, John and Adrienne.

Acknowledgements

First of all, I would like to thank Danny and Richard for supervising me over the last three years, and also for the time and effort they have put into discussing ideas and possible problems with the experiments. I would also like to thank the other members of the ion trapping group, particularly Eoin for acting as the resident technomancer to bring our errant (and decidedly classical) computers into line.

I would like to thank my friends. Notably those in the Imperial Big Band for providing musical stimulation and the whole Queen's posse, especially the medics for letting me know how many lives they had saved whilst I was intrepidly pursuing ions to trap and tame. And Helen for also having a penchant for drinks beginning with 'G' and providing plenty of opportunities to indulge to excess.

Finally, I would like to thank my family who have always been supremely supportive; particularly my parents for all their encouragement. And last but certainly not least to Morwenna, for being Morwenna.

Contents

Chapter 1

Introduction

Ion trapping has a history of forty years. Fundamentally, there are two types of trap which are in common use. These are the Penning trap which uses static magnetic and electric fields to trap ions and the rf trap which uses time varying electric fields to trap ions. In both traps, ions can be trapped in a very clean environment with a pressure of less than 10^{-9}mbar; this allows the ions to be relatively free of interactions with other matter. Cooling of the ions can be achieved by applying lasers with frequencies close to those of transitions within the ions. In this way it is possible to localise a single ion of an element in relative isolation. This has been of interest for studying fundamental physics as well as producing frequency and time standards by performing accurate spectroscopy.

Quantum information processing has provided a new way to look at computation. Instead of coding information as classical bits (i.e. either 'on' or 'off' states), it is possible to code information in terms of qubits. A qubit may be in a superposition of an 'off' and 'on' state rather than purely in one state or the other, allowing for quantum parallelism in computation. Additionally, quantum systems have the ability to entangle qubits, a resource which is not available to classical systems. Certain tasks may therefore be completed in a fundamentally quicker way using quantum information processing than classical information processing will allow. These tasks appear to be rare but include important problems such as factorising large numbers and searching disordered lists.

Recently, there has been increased interest in using trapped ions as one possible system for performing quantum information processing. This is being attempted by several groups in rf traps, but there has so far been much less interest in attempting similar work in Penning traps. Penning traps have been less favoured because the magnetic field causes complications in both the ion motion and the atomic level structure of ions. However, it is possible that the Penning trap will have an intrinsically lower level of decoherence than rf traps, which could prove vitally important for realisations of quantum computers.

1.1 Description of thesis

This thesis describes the work done over the first three years of a new long-term project within the ion trapping group at Imperial College. Our group is part of a pan-European consortium to investigate the practicality of quantum information processing (QIP). The ultimate goal of the project, is to measure the coherence of motional quantum states in a Penning trap. This may turn out to be fundamentally different from that in an rf trap and as such may provide an interesting new direction for ion trap quantum computers.

The thesis is primarily designed to present the work done so far, but care has been taken to make this a useful document for new students to our group by introducing the subject matter and providing a blueprint for how to operate the equipment in our lab. In light of this, the thesis starts with two chapters describing the background to this research. The first of these should be seen as a general overview of quantum information processing and should help one to understand the motivation behind studying this exciting and relatively new discipline. The second of these chapters considers ion trapping more explicitly. It explains the basics of ion trapping in both the Penning and rf traps and some of the ion dynamics associated with these traps. Laser cooling schemes and implementations of quantum gates are considered explicitly. Overall, these chapters should constitute both a review of the current literature in the field and a tutorial for anyone new to the subject.

Following on from this is a chapter describing some computer simulations which I have performed. These simulations were carried out in Excel using a rate equation approach and are concerned with laser cooling a four level system using two cooling lasers. They afford a view of a novel system whereby two equivalent cooling lasers are used and complement our experimental studies of Ca^+ in a Penning trap.

The three subsequent chapters describe the experimental research undertaken to trap and laser cool Ca^+ in a Penning trap. This work was done jointly with K Koo, another PhD student in our group. The first of these chapters describes the apparatus used. At the start of this project the optical table was bare and all the apparatus used is either new to the group or has been modified in some way. The exception is the conventional electro-magnet used to create the magnetic field for the Penning trap.

The second of these chapters describes how to set up the apparatus to trap and laser cool Ca^+ ions in a Paul trap. This was a necessary step on the road to operating a Penning trap, allowing us to gain experience with diode lasers and Ca^+ ions in a less critical environment than the Penning trap. Trapping single ions is described at the end of the chapter. The work in the Paul trap in this chapter is not fundamentally different to that done by several other groups.

The final of these three chapters describes the trapping and laser cooling of Ca^+ in the combined and Penning traps. Only two species of ion (Be^+ and Mg^+) had ever been trapped and laser cooled in a Penning trap before this. These two species of ions share a level structure which allows Doppler cooling to be achieved using a single laser frequency. Ca^+, however, requires two equivalent cooling lasers or optical pumping will occur into an unaddressed state.

The final chapter of this thesis describes the locking of a Ti:sapphire laser to an ultra-stable cavity using the Pound Drever Hall scheme. This laser will be used for sideband cooling by addressing the $S_{1/2}$-$D_{5/2}$ transition in Ca^+ at 729nm. Locks to two separate systems are described, one implemented during a stay at the National Physical Laboratory with S Webster, the other at Imperial College.

Two articles have been written and will be submitted soon. One paper on the simulations described in Chapter 4 and one on the experimental work on trapping and laser cooling Ca^+ in the Penning and combined traps.

Chapter 2

An introduction to quantum information processing

This chapter provides a broad overview of the field of quantum information processing. It includes some of the history of the area as well as discussing motivation for the subject. It should be thought of as a brief introduction to the subject matter for anyone who may be unfamiliar with some of the background and in particular is written with students who are just starting within our group at IC in mind. This chapter will deal primarily with the theoretical fundamentals, whilst the next will deal more concretely with the background of ion trapping and its place in quantum information processing. This chapter may be thought of as motivating the long term study of quantum information processing and the reasons for wishing to realise a quantum computer.

2.1 Introduction

Currently, there is much interest in the subject of quantum information processing, which has grown from almost nothing in the early nineties to the point where there are many groups in Europe and America who are working on both the theory and realisations. Although the origins can be traced back to Richard Feynman [1] [2] and even further to P Benioff [3] [4], who considered how a Turing machine may be simulated in a quantum system, J I Cirac and P Zoller [5] provided much of the current impetus. Their seminal paper linked ion trapping with a realisation of quantum computing which is now almost universally seen as a starting paradigm from which to build a quantum information processor. Significant progress has been made in recent years, but the end goal of practical quantum computing to solve classically ‘hard’ problems, would still appear to be many years away. However, the outlook appears brighter now than before the discovery [6] [7] of error correcting codes in 1996. Indeed, before 1996 many people thought that building a useable realisation would be impossible. Quantum algorithms have been found to utilise the power of a quantum computer (Shor’s factorisation algorithm and Grover’s search algorithm). As such, two major theoretical discoveries have changed the outlook for quantum computation: quantum algorithms and error correction. They have respectively motivated the study and provided hope that a useful system could one day be built.

Experimentally, progress has also been made, with D J Wineland’s group at NIST and R Blatt’s group at Innsbruck leading the field in ion trapping. C-NOT operations have been implemented which are discussed in the next chapter. NMR studies are able to perform very simple quantum algorithms [25]. Unfortunately due to the collective nature of the quantum bit states it is not seen as a realistic alternative for large scale computation since it is not obviously scalable. There are many other approaches now being considered to implement quantum information processing. These include such diverse ideas as superconducting junctions, trapping ions in fullerene structures on chips, using cavity QED and holding atoms in optical lattices.

2.2 Overview of information theory

Classical information theory is concerned with the nature of information and how to describe the information content within a statement. Traditionally it has been a branch of mathematics rather than physics and as such operations are carried out with little reference to physical systems. The unit of classical information is the bit*[1]. One bit* carries information equivalent to the state of one element of a system which can be either ‘on’ or ‘off’. These ‘on’ and ‘off’ states are usually referred to as ‘0’ and ‘1’. Now, the maximum information that N bistable elements could hold is N bits*. However, as will be shown, this is only the case if the states are completely uncorrelated. The string of N elements could hold much less information if there is correlation between them. As an extreme example, consider the case where either all N bits are 0 or all N bits are 1. Checking the state of the first bit would then automatically tell you the state of all N elements so you would gain no more information by looking at the other $(N-1)$ elements. The system would contain one bit* of information. Since the addition of more bistable elements does not necessarily mean a corresponding linear increase

---

[1] Throughout this chapter, ‘bit*’ will be used in the strict sense to denote a unit of information, whilst ‘bit’ will be used in a looser sense.

in the amount of information stored, it would therefore make sense to define a mutual information between two bistable elements (bits).

First, consider a reasonable definition of the information content of N bits. Note that if the probability p_α of a bit being 1 is unity then there is no information gained from reading the bit. Conversely if $0 < p_\alpha < 1$ then there is information gained by reading the bit. So the amount of information (I) contained in the bit would be a function of p_α.

i.e. $$I_\alpha = f(p_\alpha)$$

Similarly for an independent second bit

$$I_\beta = f(p_\beta)$$

Now consider the bits together. If their values are independent then $p_{\alpha\beta} = p_\alpha p_\beta$ where $p_{\alpha\beta}$ is the probability of both α and β being in state 1. The total information would be

$$I_{\alpha\beta} = I_\alpha + I_\beta$$

So

$$f(p_\alpha . p_\beta) = f(p_\alpha) + f(p_\beta)$$

This implies that f must be some form of logarithmic function. Therefore define the information as

$$I = -\log_2(p)$$

Extrapolating to a system which outputs words of N bits each (i.e. $2^N = M$ possible outputs), then the information gained by reading a single word is

$$I_i = -\log_2(p_i) \qquad\qquad i = 1, 2, \dots .M$$

where p_i is now the probability of the N bit word i. We could also calculate an average information per word for this system

$$H(X) = \sum_{i=1}^{M} p_i \log_2(1/p_i)$$

which we will call the source entropy.

2.2.1 Entropy and classical information

It has already been remarked that classical information theory pays little attention to physical realisations. However, there is one very close link to classical physics in the entropy. The entropy of a system in statistical mechanics provides a measure of the disorder or uncertainty in a system [9]. The uncertainty is also a measure of the information (cf. $I_i = \log_2(1/p_i)$ the higher the uncertainty, the lower p_i so the higher I_i). Thus we have a link with which to use the idea of information to solve some physical problems. One such problem which was unsolved before the application of information theory was that of Maxwell's demon.

Maxwell's demon

Maxwell's demon was a 'paradox' which seemed to contradict the laws of thermodynamics. Consider a box partitioned into two compartments with a door in the partition. Both compartments are initially filled with gas. Obviously there is a distribution of speed in the gas molecules. Now, suppose that every time a fast molecule approaches the door from the left, Maxwell's demon opens the door to let it through the partition. This would cool the first compartment and heat the second. Since no work is done, this would directly contravene the second law of thermodynamics. The resolution had to wait over a hundred years, although Szilard [10] made considerable steps toward the answer.

The reason the second law isn't violated depends fundamentally on our earlier definitions of information. For Maxwell's demon to be able to open the door at the correct moment, he must have some information about the speed of the molecules. This would be stored in its memory, so each time a molecule is let through, the memory has to store more information and its entropy increases. If the demon should erase its memory, then this would cost energy and so the 'paradox' is resolved. This approach was proposed by Bennett [11]. It relied on Landauer's [12] principle which essentially states that there is an energy cost to erasing information.

2.2.2 Classical computing

Now we have discussed a general formulation for information it is sensible to put computing on a similar footing. Computing involves the manipulation of information. Again, the challenge is to define the subject in a mathematical way so as to generalise the notion of computability. Turing and Church [13] [14] proposed that any device which could realistically be called a (classical) computer could be simulated perfectly[2] by a simple device performing operations on an infinite data tape. This device became known as a Turing machine.

A Turing machine can be visualised as in Figure 2.1. Through the box runs a tape which is divided into a series of boxes. Each box is either blank or contains an 'X' which the machine can read. The machine can also write an 'X' or erase an 'X' from a box. The machine has a finite number of internal states, which are represented by a rod which passes through the machine. At any given time the machine is in one of its internal states.

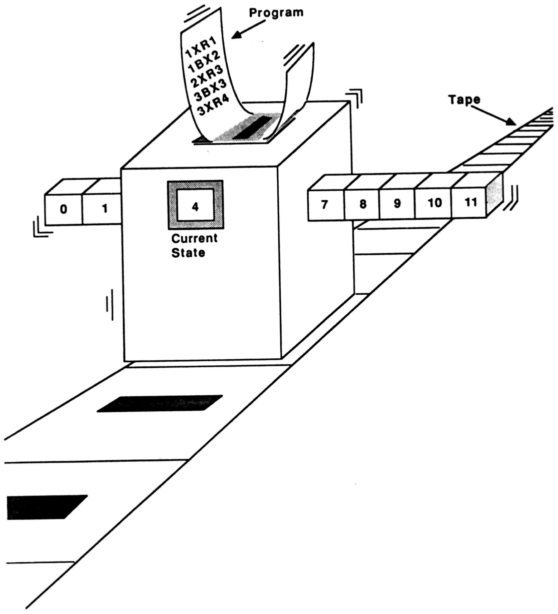

Figure 2.1: Diagram showing a possible design of a Turing machine, from [29]

To operate the machine, it is fed a program and some initial data (which takes the form of marks on the tape). The program is a list of four-character codes (e.g. 2XR1, 1BX2) which tell the machine what to do in any given situation. The first two of the four symbols refer to the present internal state of the machine (a number) and the state of the current box on the tape (B- blank, X- marked) respectively. The program then implies a mapping from the given internal state (ie. the first two symbols) to the action to be taken. The action to be taken is encoded in the third and fourth symbols: B is erase mark in box; X is mark box; R is move tape one box to the right; L is move

---

[2] This is achieved without exponential slow down as the size of a problem to be computed is increased.

tape one box to the left and the numbers represent the new internal state of the machine. The machine operates as follows:

(i) read internal state and state of the current data box on the tape
(ii) look up the correct action for these states in the program
(iii) perform the required actions
(iv) go to (i)

The internal state 0 is reserved for 'off' and is used when the machine has finished a computation.

The concept of the Turing machine allowed concentration to switch away from particular systems and onto more general properties of computational problems. Two of the most fundamental issues are whether a problem is computationally 'hard' and whether a problem is solvable.

Problems can be divided into classes depending on whether they are 'hard' or not. This is a precisely defined term in information theory. It depends critically on the dependence of the time taken to solve a problem with the information content of the input. For instance a typical problem may be

'Given x, find its prime factors'

where x is the input and contains information $I = \log_2 x$ (i.e. the number of bits needed to specify x). The time taken to solve the problem is a function of the size of the input. If the time taken can be written as a polynomial with finite number of terms then the problem is not considered 'hard'. However, if the time taken depends on an exponential function of I, then it is considered 'hard'. 'Hard' problems suffer from a dramatic increase in the time typically taken to solve the problem as I increases.

Take $T(I)$ to be the time typically required to complete a problem. Consider two cases

$$T_1(I) = I^2 + I^3 \qquad \text{Polynomial dependence}$$

$$T_2(I) = e^I \times 10^{-21} \qquad \text{Exponential dependence}$$

So, for instance, if x has twenty digits then $x \sim 10^{20}$ and $I \sim 20 \log_2(10) \sim 60$ So $T_1(I) \sim 2.2 \times 10^5$ and $T_2(I) \sim 1.1 \times 10^5$

But for a forty digit x then $x \sim 10^{40}$ so $I \sim 40 \log_2 10 \sim 120$ which gives $T_1(I) \sim 1.7 \times 10^6$ and $T_2(I) \sim 1.3 \times 10^{31}$

This dramatic difference between hard and easy problems completely alters the feasibility of the solution. It is this which explains why the concept of the Turing machine is a useful one. Any classical computer can be simulated by a Turing machine in such a way that hard problems are mapped to hard problems and easy problems are mapped to easy ones. This is the Church-Turing hypothesis [13] [14].

However 'hard' a problem may be, knowing that there is a computable algorithm to solve the problem can still be of benefit. There is another class of problems which are uncomputable. The question of whether a problem is computable can be re-framed in terms of a Turing machine. The Turing machine is given a program such that it will only halt in a finite time if it solves a given problem. If the Turing machine will ever halt, then the problem is computable. Unfortunately in general there is no possible way to check if an algorithm will halt which is shorter than running the algorithm and waiting. This has deep links to the foundations of mathematics and Gödel's and Chaitin's theorems[3].

2.2.3 Encoding and error correction

As was discussed earlier, the number of bits* of information is not the same as the number of bits in the string. This naturally gives rise to considerations of encoding information, redundancy and error correction.

If a message is to be transmitted then the information must be encoded (e.g. as a series of bits). There is a maximum amount of information that can be encoded in a string of this length and the information content of the message will be less than this. Sending more bits than there are bits* allows there to be information encoded about the string of bits itself. This redundancy facilitates error correction schemes such as the Hamming code (see table).

The Hamming code is a common way of encoding four-bit words. Each of the sixteen four-bit words corresponds to a seven-bit Hamming code label. The sixteen seven-bit labels are constructed such that flipping any single bit will result in a seven-bit word which is not a Hamming label. The erroneous bit can then be reset since only by flipping the erroneous bit can a Hamming label be reached.

The number of bit flips before one code word becomes another is the Hamming distance between the words. This system can be thought of as points in a seven-dimensional space, where there are 2^7 points corresponding to the vertices of a seven-dimensional cube. However, only sixteen points are allowed as codewords so traversing to any adjacent vertex goes to an unallowed state.

---

[3] Gödel's (second incompleteness) theorem asserts that any formal system complex enough to include number theory can express valid theorems which it cannot prove. It is encapsulated as a result of Chaitin's theorem which places limits on the complexity of any string which can be proved within a finitely stateable system [29].

These error correction schemes will take on greater significance for the quantum theory of information, since this is more directly concerned with the physical world than classical information theory. Error correction may prove vital in countering the unavoidable errors caused by the decoherence of quantum states.

four bit word	seven bit Hamming code
0000	0000000
0001	1010101
0010	0110011
0011	1100110
0100	0001111
0101	1011010
0110	0111100
0111	1101001
1000	1111111
1001	0101010
1010	1001100
1011	0011001
1100	1110000
1101	0100100
1110	1000011
1111	0010110

2.3 Quantum information

Classical information theory is concerned with bits*, which are either in a ‘1’ or ‘0’ state. Now, consider physically representing a bit so as to be able to perform computations. One might consider using a high or low voltage at an electrode; a bistable switch; or perhaps a smaller system would be adequate, such as the ground and an excited state in an atom. This raises another point. The atom need not be completely in the ground state ($|0\rangle$) or the excited state ($|1\rangle$) but could be in an arbitrary superposition $|\psi\rangle$ of the two states

$$|\psi\rangle = a|0\rangle + b|1\rangle$$

By considering fundamental physical principles we have come to new ideas which may broaden the scope of information theory.

Define a new unit of quantum information, the qubit*. This is a quantum analog to the bit* and is the amount of information that can be encoded in one two state system (where quantum mechanical laws hold). The orthogonal states $|0\rangle$ and $|1\rangle$ are vectors in Hilbert space and so the state $|\psi\rangle$ is also a vector in Hilbert space. The $|0\rangle$ and $|1\rangle$ states form a basis, so one qubit exists in a two dimensional Hilbert space. It is natural to think of N independent qubits with states $|\psi_i\rangle,\ i = 0, 1, \ldots, N-1$ as spanning a Hilbert space of 2^N dimensions since the state of the whole system corresponds to a superposition of 2^N orthogonal states. The basis states can be labelled as a binary number representing definite $|0\rangle$ and $|1\rangle$ states for each qubit (i.e. $|10011\rangle$ represents $|1\rangle \otimes |0\rangle \otimes |0\rangle \otimes |1\rangle \otimes |1\rangle$ where $\otimes$ is the tensor product).

So a general state of a two qubit system could be written

$$|\psi\rangle = a|00\rangle + b|01\rangle + c|10\rangle + d|11\rangle$$

It follows that the general state for N qubits is

$$|\psi\rangle = \sum_{i=0}^{2^N-1} \alpha_i |i\rangle$$

This is fundamentally different from a classical register of N bits, which can only be in one of 2^N states at any given time. A quantum register of N qubits can store 2^N values simultaneously. Conceptually, it is plausible that this could greatly change the nature of computation.

A classical algorithm can be viewed as a many to one function. For some input x, the output is $f(x)$

$$x \longrightarrow f(x)$$

Now for a quantum system, in a superposition

$$|\psi\rangle = \alpha_0|0\rangle + \alpha_1|1\rangle + \ldots \alpha_{N-1}|N-1\rangle$$

$$\begin{array}{ccc} \alpha_0|0\rangle & & \alpha_0 f(|0\rangle) \\ \alpha_1|1\rangle & \longrightarrow & \alpha_1 f(|1\rangle) \\ \alpha_2|2\rangle & & \alpha_2 f(|2\rangle) \\ \vdots & & \vdots \end{array}$$

So the properties of the function for any state $|i\rangle$, $f(|i\rangle)$ are present in the output. However, since measurement of the output would necessarily collapse the state into only one of the output basis states, it may take considerable ingenuity to access this untapped information. This illustrates the parallel nature of quantum computing.

Whilst this is a departure from the classical digital computing, it does not tell the full story of quantum computing. A superposition may be created classically (for instance, the polarisation of light) and quantum systems have another resource important for the new ideas in computing. This resource is entanglement between systems, whereby the wavefunction of the system as a whole cannot be written as a product state between the separate subsystems. Experimental progress in creating entangled states on demand is important for quantum information processing and will be considered in the next chapter.

2.3.1 Quantum computing

The Church-Turing hypothesis established the idea of universality in classical computing. We made reference to the Turing machine as an example of a universal computer. Another representation of a universal classical computer is as a network of gates. These gates typically take one or two bits of input and produce one bit of output. Typical gates are AND, NOT, OR (represented by functions $a.b$, $a+1$, $a+b-a.b$ (all mod 2) for inputs a and b in binary notation). It is easy to show that any of these gates could itself be made from a network containing only NAND gates ($\mathrm{mod}_2[a.b+1]$). Thus a NAND gate can be considered a universal gate. This is much closer to how a PC actually works. A universal quantum computer can be represented by a similar network of quantum gates [15] [16].

These quantum gates should be represented by unitary operators since unitary operators describe the time evolution of an isolated quantum system. Several simple gates are

$$\begin{array}{rcll} I & = & |0\rangle\langle 0| + |1\rangle\langle 1| & \text{identity} \\ X & = & |0\rangle\langle 1| + |1\rangle\langle 0| & \text{NOT} \\ Z & = & |0\rangle\langle 0| - |1\rangle\langle 1| & \begin{array}{l}\text{phase change of any part of super-}\\ \text{position corresponding to state } |1\rangle\end{array} \\ Y & = & |1\rangle\langle 0| - |0\rangle\langle 1| & \begin{array}{l}\text{NOT with phase change for any}\\ \text{part corresponding to state } |1\rangle\end{array} \end{array}$$

However these do not include important gates with more than one input qubit. An example of a universal quantum gate (when combined with the arbitrary rotation of a single qubit) is the controlled-NOT gate (C-NOT)[17].

This has two inputs and has a truth table similar to that of a classical XOR gate. This can be written as

$$(|0\rangle\langle 0|) \otimes (|0\rangle\langle 0| + |1\rangle\langle 1|) + (|1\rangle\langle 1|) \otimes (|0\rangle\langle 1| + |1\rangle\langle 0|)$$

operating on the arbitrary state

$$a|0\rangle \otimes |0\rangle + b|0\rangle \otimes |1\rangle + c|1\rangle \otimes |0\rangle + d|1\rangle \otimes |1\rangle$$

(where the tensor product for two qubits is now written explicitly) which gives

$$a|0\rangle \otimes |0\rangle + b|0\rangle \otimes |1\rangle + c|1\rangle \otimes |1\rangle + d|1\rangle \otimes |0\rangle$$

By inspection this has the truth table

$$\begin{array}{ccc} |00\rangle & \longrightarrow & |00\rangle \\ |01\rangle & \longrightarrow & |01\rangle \\ |10\rangle & \longrightarrow & |11\rangle \\ |11\rangle & \longrightarrow & |10\rangle \end{array}$$

The C-NOT gate flips the second (target) qubit if the first (control) qubit is $|1\rangle$ otherwise it acts like the identity.

2.3.2 Quantum algorithms

Given that a quantum processor can behave in ways fundamentally different from a classical one, we must now ask whether we can harness that difference. However, we must also realise that a classical computer can simulate any quantum system to arbitrary precision. This means that it is possible for a classical computer to calculate anything which a quantum computer can and so the set of computable problems remains the same. This is not to say that some problems may not move complexity class. An example would be the factorisation of large numbers, which appears to be in the class NP for classical computation but in class P for quantum computation[4]. Such algorithms where quantum information processing is manifestly more efficient than classical information processing are rare, although significant efforts have been expended trying to find more. I will briefly describe three of the major applications of quantum information processing which have been discovered so far.

---

[4] For class NP, the time needed to *verify* the answer increases polynomially with information content of the input. For class P, the time needed to *compute* the answer increases polynomially with information content of the input

Simulation of quantum systems [18] [19] [20]

Simulation of a quantum system by a classical computer is in general a hard problem. It would require 2^N complex numbers to specify the state vector in a 2^N dimensional Hilbert space. To manipulate such a state vector would require using matrices of dimension $2^N \times 2^N$, and so the time taken would rise as 2^{2N}. A quantum computer could perform the same calculation with N qubits [17], but it would still take 2^{2N} operations to form an arbitrary unitary transformation. However for certain problems involving only short range interactions the unitary transformations are far from arbitrary and the time required to evolve the system becomes polynomial in N. Examples of such problems include the Ising and Heisenberg models for spin lattices as well as the hard sphere and Van der Waals gases. This is similar to Feynman's original conception of a quantum computer [1] [2] and could be considered as the greatest advantage of a quantum computer over a classical one. It is possible that with as little as 20 qubits, it would be possible to perform simulations of quantum systems that would be intractable at present.

Grover's search algorithm [21]

This algorithm is for searching through an unordered list. Consider a list of N items α_i where $i = 1 \cdots N$ which includes one and only one item which satisfies

$$A(\alpha_j) = 1 \text{ for some } j < N \text{ but } A(\alpha_i) = 0 \text{ for } i \neq j$$

where performing $A(\alpha_i)$ is a computationally easy task. The problem is to find j. Classically there is no more optimal solution than trying each member α_i individually. This must take on average $N/2$ evaluations of $A(\alpha_i)$ since this is an unordered list (ie. the time taken is $O(N)$). However, the Grover search algorithm can find the answer in $O(\sqrt{N})$ tries. This does not exponentially increase the efficiency, but does speed up the process quadratically. The importance of this method can be seen for all problems in complexity class NP, where if nothing else an exhaustive search of all the solutions could be completed.

Shor's factorization algorithm

Shor's factorization algorithm [22] is the most well known application for a quantum computer. It displays an exponential speed up from the best classical algorithm (the number field sieve) for a problem believed to be in class NP classically. If it became routine to factorize large numbers, this would have profound consequences for the widely used RSA (Rivest, Shamir, Ableman) public key encryption system. It would then be a simple matter to decode the vast majority of ‘secret’ transmissions produced today. Shor’s algorithm can solve the problem in time $O[(\ln n)^3]$ whereas the number field sieve takes time $\exp[c(\ln n)^{1/3}(\ln \ln n)^{2/3}]$.

This algorithm uses both the parallelism inherent in a quantum superposition and entanglement of the qubits to produce the required result. The full extent of the difference between quantum and classical information theory can thus be seen in this algorithm.

2.3.3 Error correction

For quantum algorithms to attain significant advantage over classical ones would require very large problems using perhaps 10^{10} gates. For this huge number of gates, error correction is essential since even a small probability of error on each operation would cause a considerable number of errors by the end of the calculation. It is possible to prove [23] that some errors are unavoidable due to decoherence in the system i.e. if two or more qubits are coupled together then they must also be coupled to their environment. The evolution of the system is then not unitary and the correlations between the qubits can be distributed through the environment and lost altogether.

Classical schemes for error correction include dissipation and amplification of the states. Amplification of an unknown state is not allowed in quantum mechanics due to the no-cloning theorem. This states that an unknown quantum state cannot be cloned. To prove that cloning would lead to contradiction, consider two qubits, one in state $|x\rangle$ which we wish to copy onto a second in state $|0\rangle$. So acting with a cloning operator C

$$C(|x\rangle|0\rangle) = |x\rangle|x\rangle$$

Also for a cloning operator

$$C(|y\rangle|0\rangle) = |y\rangle|y\rangle$$

But consider the state $|z\rangle = |x\rangle + |y\rangle$, then

$$\begin{aligned} C(|z\rangle|0\rangle) &= C\Big((|x\rangle + |y\rangle)|0\rangle\Big) \\ &= |x\rangle|x\rangle + |y\rangle|y\rangle \\ &\neq |z\rangle|z\rangle \end{aligned}$$

so the operator fails. This shows that it is impossible to create an exact duplicate of an unknown quantum state.

Now consider the possible errors which may occur during a computation [24]

▶ Bit flip errors cause a bit to rotate from a $|1\rangle$ state to a $|0\rangle$ or vice versa

$$\begin{aligned} |0\rangle &\longrightarrow |1\rangle \\ |1\rangle &\longrightarrow |0\rangle \end{aligned}$$

▶ Phase errors change the phase of one component of a superposition

$$\begin{aligned} |0\rangle &\longrightarrow |0\rangle \\ |1\rangle &\longrightarrow -|1\rangle \end{aligned}$$

▶ Small errors can occur in the coefficients of a superposition

$$a|0\rangle + b|1\rangle \longrightarrow \alpha|0\rangle + \beta|1\rangle \qquad \text{where } a \approx \alpha, b \approx \beta$$

▶ Any measurement to find errors will irrevocably disturb the system.

Example of a quantum error correcting code

Consider encoding each qubit as three qubits

$$\begin{aligned} |0\rangle &\longrightarrow |000\rangle \\ |1\rangle &\longrightarrow |111\rangle \end{aligned}$$

So the superposition $a|0\rangle + b|1\rangle$ becomes $a|000\rangle + b|111\rangle$. However if we measure the output of XOR ($\oplus$) on two of the qubits, then for state $|xyz\rangle$ if there is one error then $(x \oplus y, y \oplus z)$ will not only indicate the error, but indicate which of the qubits has been flipped. This does not disturb the superposition.

This scheme will also detect small errors. Consider the error

$$|000\rangle \longrightarrow \sqrt{1-\epsilon^2}\ |000\rangle + \epsilon|100\rangle \quad \text{where } \epsilon \text{ small}$$

then a measurement will either project the system back onto $|000\rangle$ or onto $|100\rangle$ (with probability ϵ^2). In the first instance the error is gone, in the second instance it can be corrected using the bit flip schema above. A similar redundancy can be used to encode the phase information using nine qubits [22] [6].

2.3.4 Realisations of a quantum computer

A classical computer has certain parts which would need to have some form of analogue in a realisation of a quantum computer. These would include:

- ▶ a memory to store data whilst it is being used in the computation
- ▶ data transfer to take the information from memory to processor
- ▶ gates to actually process the information
- ▶ a way to initialise the registers to put them into a known state
- ▶ a readout to measure the output of a calculation

The system of realisation will also have to exhibit a degree of robustness and isolation from the environment outside the system yet strong interactions coupling the qubits and precision in manipulating quantum states. Otherwise the computer will be plagued by errors so as to be unusable. These are very stringent requirements and could only ever be met in a few special systems. So far, a few candidates have been considered, which include: quantum dots; superconducting rings; NMR; cavity QED; atoms in optical lattices; and trapped ions. NMR will briefly be considered here as the only system to achieve any kind of computation so far. Ion trapping will be discussed in the next chapter and is arguably the best candidate for the medium term, having advantages of scalability over NMR.

Nuclear magnetic resonance [25]

Here the states of the qubits are represented by the spin of nuclei in a molecule. This is an ensemble method since individual nuclei are never measured. The system is a macroscopic sample of molecules in a liquid. The energy splitting between the $|\uparrow\rangle$ and $|\downarrow\rangle$ states of the nuclear spin is small in comparison to the thermal energy of the sample ($T \sim 300K$) so the states are equally populated. A magnetic field can be applied to order the spins and then subsequent magnetic pulses can rotate the spins predictably. These pulses must be precisely timed since they are exciting Rabi oscillations between the states. Special efforts must be taken to ensure that all of the molecules evolve identically, which limits the scalability of the realisation. With increasing numbers of qubits the signal drops off as 2^{-N} (where N is the number of qubits), which limits the technique to around 10 qubits. The signal drops off in this manner since the sample is initially distributed equally over 2^N levels and so the number in the required initial state drops as 2^{-N} as N is increased.

NMR is currently the most advanced realisation and has been used to demonstrate entanglement and in ‘toy’ problems. Notably, the generalised

Grover's algorithm has been demonstrated [27] and the number 15 has been factorised using seven qubits [30]. There are doubts as to whether it really is genuine quantum computation since the manipulation and measurement is done on a macroscopic level rather than on an individual clean quantum system. The techniques used for QIP in NMR are well established and have been in use for many years. It is the application and development of these techniques which has allowed the progress to be made.

Chapter 3

Introduction to ion trapping and the ion trap quantum computer

This chapter serves as an introduction to realisations of quantum information processing in an ion trap. It is roughly split in to three sections. The first discusses trapping in general and the commonly used traps. The second discusses various types of laser cooling, including schemes to cool ions to the motional groundstate of the trap. The third section discusses the present state of quantum information processing in ion traps.

Having discussed the motivation for research into quantum information processing in the last chapter, the third section shows how ion traps can be used in a realisation of a quantum computer with specific reference to the CNOT gate. This has already been implemented in a linear Paul trap. A brief discussion on decoherence and the problems it causes is given, along with the consideration of Penning traps as quantum information processors. Finally, a synopsis of the long term goals of this project is presented.

3.1 Ion traps

An ion trap is a device for confining charged particles within a region of space. To achieve this, some form of potential well must be created in that region. This is achieved by applying electromagnetic fields. Ion traps are now used extensively in many areas of physics, having been developed over the last forty years. One of the prime reasons for their popularity is the clean environment which they afford. Electromagnetic fields can be generated in ultra-high vacuum conditions which allow trapped particles to be free from interaction with other matter. This greatly facilitates the study of the fundamentals of quantum mechanics. Another byproduct is that the particles can be confined for long times ($\sim$ hours), which is highly desirable for precision measurements such as those required to implement frequency standards.

3.1.1 The Penning trap

The Penning trap uses static electric and magnetic fields to trap charged particles. It grew out of the work of Penning [31] who was studying electrical discharges in magnetic fields. He noted that the path length of the electrons in the discharge was very long. This was due to the cyclotron motion of the electrons around the magnetic field direction.

The potential needed to trap an ion in three dimensions cannot be made solely from electrostatic (or magnetostatic) fields. This is Earnshaw's theorem and follows directly from Maxwell's equations in free space ($\nabla.\mathbf{E} = 0$, $\nabla.\mathbf{B} = 0$). Instead of a three dimensional potential well, an electrostatic saddle point is used with an axis of cylindrical symmetry parallel to the z-axis. The particle is then confined in the axial direction but not in the radial direction. To create such a potential, conducting electrodes should follow the lines of constant potential. A suitable equation for the electrode surfaces is therefore

$$\frac{r^2}{r_0^2} - \frac{z^2}{z_0^2} = \pm 1 \tag{3.1}$$

where r is the radial distance from the symmetry axis and z the displacement along the axis. This corresponds to the geometry in Figure 3.1. This has three distinct electrodes which are usually called the 'ring electrode' and the 'endcap electrodes', the endcaps being kept at potential $+U_0$ compared to the ring electrode. r_0 is the smallest radius of the ring electrode and $2z_0$ is the distance between the endcaps. To confine a particle in all three dimensions, a magnetic field is added in the axial direction. The presence of a magnetic field *alone*, would cause the charged particles to exhibit circular cyclotron motion in the radial plane at frequency $\omega = eB/m$ and free motion in the z direction. The combination of the two fields allows the particles to be trapped. The full motion of the ions under application of both fields is seen to be epicyclic [32].

It can be shown [33] that the equations of motion for the trapped ion are

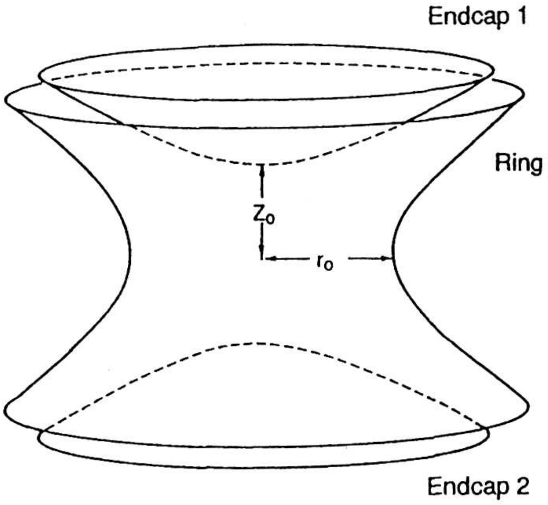

Figure 3.1: Electrode structure of a standard trap, from [34]

$$\begin{aligned} \ddot{x} &= \omega_c \dot{y} + 1/2\ \omega_z^2 x && (3.2)\\ \ddot{y} &= -\omega_c \dot{x} + 1/2\ \omega_z^2 y && (3.3)\\ \ddot{z} &= -\omega_z^2 z && (3.4) \end{aligned}$$

where $\omega_c = eB/m$ is the (angular) cyclotron frequency and $\omega_z = \sqrt{\frac{4eU_0}{m(2z_0^2+r_0^2)}}$ is the axial frequency. Obviously the motion in the axial direction is uncoupled from that in the x and y directions and represents a simple harmonic oscillation between the endcaps.

To find the motion in the radial plane it is easiest first to transform into a frame rotating at $\omega_c/2$ [34]. This effectively nulls the magnetic field, leaving the x and y motions uncoupled.

$$\begin{aligned} \ddot{x'} &= \left(\frac{\omega_z^2}{2} - \frac{\omega_c^2}{4}\right)x && (3.5)\\ \ddot{y'} &= \left(\frac{\omega_z^2}{2} - \frac{\omega_c^2}{4}\right)y && (3.6) \end{aligned}$$

The particle therefore moves in a two dimensional simple harmonic oscillator potential in the rotating frame. Obviously the potential in the axial direction is unchanged by the change of reference frame so the overall effect of the magnetic field is to create a potential minimum at the trap centre in this frame.

The frequency of the solutions in the radial plane in the rotating frame is

$$\omega'^2 = \frac{\omega_c^2}{4} - \frac{\omega_z^2}{2} \tag{3.7}$$

These solutions imply a rotation in either a clockwise or an anti-clockwise sense in the rotating frame and so transforming back to the lab frame gives two frequencies

$$\begin{aligned} \omega_c' &= \frac{\omega_c}{2} + \omega' && (3.8) \\ \omega_m &= \frac{\omega_c}{2} - \omega' && (3.9) \end{aligned}$$

depending on whether the sense of the rotating frame is in the same or opposing sense as the solution. These two frequencies are the modified cyclotron frequency (ω_c') and the magnetron frequency (ω_m)

The explicit solutions to the equations of motion in the radial plane are

$$\begin{aligned} x &= r_c\cos(-\omega_c' t - \alpha_c) + r_m\cos(-\omega_m t - \alpha_m) && (3.10) \\ y &= r_c\sin(-\omega_c' t - \alpha_c) + r_m\sin(-\omega_m t - \alpha_m) && (3.11) \end{aligned}$$

where r_c and r_m are the magnitudes of the cyclotron and magnetron motions respectively and α_c and α_m are the phases of the motions. The trajectory of a trapped particle will then be composed of two circular motions added together. This produces the epicyclic motion, an example of which is shown in Figure 3.2. For our typical trap parameters of $B = 1\text{T}$ $U_0 = 6\text{V}$ $M = 40\text{u}$

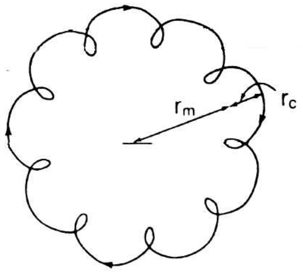

Figure 3.2: Epicyclic motion of an ion in a Penning trap, from [87]

$r_0 = 5\text{mm}$ this gives frequencies of $\omega_m/2\pi = 27\text{kHz}$, $\omega_z/2\pi = 140\text{kHz}$ and

$\omega_c'/2\pi = 356\text{kHz}$. Note that the magnetron frequency is very much less than the modified cyclotron frequency and that if $r_c < r_m$ then this gives the case in Figure 3.2.

Note that two frequency relations hold

$$\begin{aligned} \omega_c &= \omega_c' + \omega_m & (3.12) \\ \text{and} \quad \omega_c^2 &= \omega_c'^2 + \omega_z^2 + \omega_m^2 & (3.13) \end{aligned}$$

It has been shown [35] that the latter holds even for a trap in which the fields may be misaligned with respect to the ideal trap.

3.1.2 The Paul trap

Apart from the Penning trap the other common configuration for trapping charged particles is the Paul trap. This utilises time varying electric fields to circumvent Earnshaw's theorem.

Take the quadrupole field with potential

$$\phi = \phi_0 \frac{x^2 + y^2 - 2z^2}{4z_0^2} \tag{3.14}$$

which utilises the same electrode structure as Figure 3.1. Now apply the time varying voltage $-(U_0 - V\cos\Omega t)/2$ to each endcap and $+(U_0 - V\cos\Omega t)/2$ to the ring. This causes the potential to 'flap' at Ω. Just as the particle begins to be accelerated in the unstable direction, the potential changes so as to be unstable in a different direction. The particle must then begin to accelerate in this new direction, only to be thwarted as the potential changes again. The overall effect is to keep the particle confined so long as the trap parameters are chosen carefully.

This leads to the following equations of motion:

$$\begin{aligned} \frac{d^2x_i}{dt^2} + \left(\frac{e}{mr_0^2}\right)(U_0 - V\cos\Omega t)x_i &= 0 & (3.15) \\ \text{and} \quad \frac{d^2z}{dt^2} - \left(\frac{2e}{mr_0^2}\right)(U_0 - V\cos\Omega t)z &= 0 & (3.16) \end{aligned}$$

where x_i are the x and y directions. It is usual to parameterise these in terms of a and q, where

$$
\begin{aligned}
a_z &= -2a_i = -\frac{8eU_0}{mr_0^2\Omega^2} && (3.17)\\
q_z &= -2q_i = -\frac{4eV}{mr_0^2\Omega^2} && (3.18)\\
\tau &= \frac{\Omega t}{2} && (3.19)
\end{aligned}
$$

This gives the Mathieu equations

$$
\begin{aligned}
\frac{d^2x_i}{d\tau^2} + (a_i - 2q_i\cos 2\tau)x_i &= 0 && (3.20)\\
\frac{d^2z}{d\tau^2} + (a_z - 2q_z\cos 2\tau)z &= 0 && (3.21)
\end{aligned}
$$

which have an analytical solution [36].

The solutions of the Mathieu equations show stability only for certain regions of the (q, a) plane. The first stability region is used exclusively by groups using Paul traps (see Figure 3.3), but other, smaller regions of stability exist for higher values of a and q.

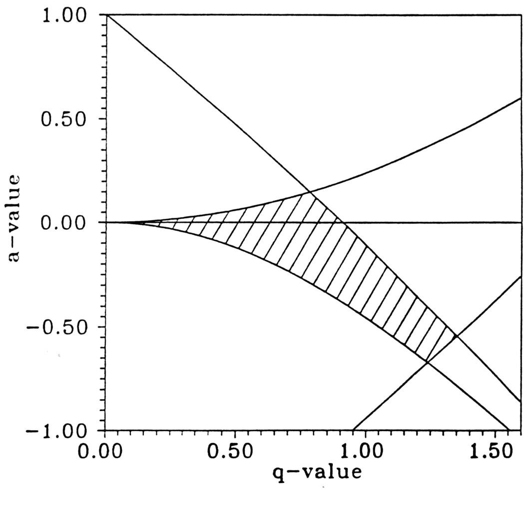

Figure 3.3: First stability region of a Paul trap for a_z and q_z, from [87]

The motion of the ions in the trap can be described in terms of two components: the secular motion and the micromotion. If the ion motion is averaged over the time period of the potential and only the components varying slowly compared to the applied frequency Ω are taken, then the particle appears to move in a harmonic potential. This is the pseudopotential [37] which gives rise to the secular motion. The micromotion is due to the fast oscillation frequency Ω. The frequency of the secular motion for $a = 0$ is

$$\omega = \frac{2\sqrt{2}eV}{m\Omega(r_0^2 + 2z_0^2)} \tag{3.22}$$

An ion sat at the centre of the trap will be free of micromotion.

It should be noted that the same trap electrodes can be used to create a Penning or a Paul trap. This feature is used in our work on Ca$^+$, in which we trap ions in both Penning and Paul traps using the same apparatus. Application of a magnetic field to a Paul trap creates a combined Paul/Penning trap. This hybrid trap is also used by us to facilitate the move from a Paul to a Penning trap.

3.1.3 The linear Paul trap

The linear Paul trap [41] is a variation in the geometry of the standard Paul trap. It is constructed from four rods to which the time-varying potential is applied across opposite pairs. Two endcaps are used to confine the ions axially using a static potential.

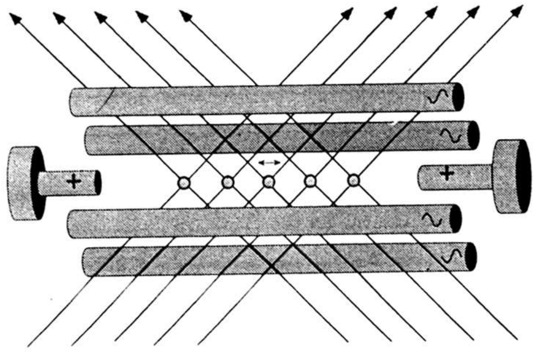

Figure 3.4: Electrode structure of a linear Paul trap, from [78]

The advantage of the linear Paul trap is that the rf component of the electric field is zero along the axis. This allows any ion sat on this axis to be free of micromotion (and thus rf heating[1]). This is in contrast to a

---

[1] /The radio frequency drive which is applied to the trap can transfer energy to the trapped ions. This is known as rf heating.

conventional Paul trap in which there is only one position of zero field and so only one ion can be free of micromotion. For this reason work on quantum computing has been carried out primarily in linear traps [38] [39] [40].

3.2 Laser cooling

When the ions in a trap are created from the ionisation of neutral atoms they are typically very hot. A rough estimate of their temperature could be given by $k_BT \sim E$, where E is their kinetic energy, and since trap depths are of the order of electronvolts this gives temperatures of thousands of kelvin. For most uses of traps it is desirable to cool the ions, usually to reduce the Doppler width (e.g. in spectroscopic applications) or to characterize the state of ions (e.g. in quantum information applications). Some of the most widely used cooling methods are: resistive cooling; buffer gas cooling; sympathetic cooling; and laser cooling.

Resistive cooling uses the ion motion in the trap combined with the electrode structure of the trap itself to form an LRC circuit which damps the 'current' which is the movement of the ions. This dissipation of energy cools the ions [50] [51]. Buffer gas cooling is achieved by introducing a gas at room temperature into the trap region and letting the trapped ions thermalise by collisions. This is most effective for light buffer gases, when energy transfer is greatest [52]. Laser cooling is a very effective method of cooling, but is only feasible for certain species due to the requirements on the electronic level structure of the ionic species and the availability of suitable lasers. Sympathetic cooling is achieved by laser cooling an auxiliary trapped species, whilst also trapping the primary species. Collisions between the two cause the primary species to be cooled [53].

3.2.1 Laser cooling free particles to the Doppler limit

Free particles can be cooled by radiation pressure. Each photon carries momentum $\hbar k$, so when a particle absorbs a photon it receives a kick in the direction of the photon velocity. If a beam of atoms and a beam of photons resonant with an atomic transition were counter-propagating then the atoms would slow down as the photons are absorbed. This deceleration of the atoms can be considered to be cooling. However, in a typical gas sample the atoms are moving in random directions. In general then, the photons could be either co-propagating or counter-propagating and the resonant light would not cool the sample.

To cool the gas, the radiation must be absorbed only by those atoms moving in a direction opposite to that of the laser beam. This is achieved by detuning the frequency to the red side of the transition. The Doppler shift then causes the counter-propagating atoms to absorb more strongly. In this way all three degrees of freedom can be cooled by six lasers [54]. The same can be done for trapped particles [55].

Before 1988, the lowest temperature that a free particle was thought to be able to reach by laser cooling was the Doppler limit. Consider a two level system as shown in Figure 3.5. When the ion absorbs a photon, an electron is promoted from level 1 to level 2. It can then absorb no more photons until the electron is brought back to level 1. There are two processes by which this could occur: spontaneous and stimulated emission. Stimulated emission will always occur in the direction of the laser beam and so the combined effect of the absorption and stimulated emission will be zero. However spontaneous emission will occur in a random direction, giving the ion a kick in a random direction, so the total effect of absorption and emission will be a momentum change of between $2\hbar k$ and 0.

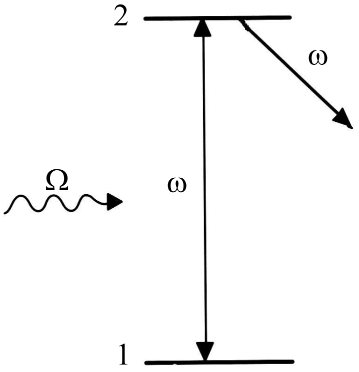

Figure 3.5: A two level atomic system

Now consider a system with natural linewidth γ rads^{-1}, level separation ω rads^{-1} and incident laser radiation at Ω rads^{-1}. Define a detuning $\Delta = \omega - \Omega$ and a transition dipole μE (where μ is dipole moment and E is the amplitude of the field), then the force on the ion in the low intensity limit is

$$
\begin{aligned}
F &= \left(\begin{array}{c} \text{momentum transfer} \\ \text{per photon} \end{array} \right) \times \left(\begin{array}{c} \text{rate of} \\ \text{absorption} \end{array} \right) \times \left(\begin{array}{c} \text{lineshape factor} \\ \text{for level} \end{array} \right) \\
&= \hbar k \left(\frac{\mu E}{\hbar \gamma} \right)^2 (\gamma) \left(\frac{\gamma^2}{(\Delta + kv)^2 + \gamma^2} \right) \qquad (3.23)
\end{aligned}
$$

Once the ion is cold and since the spontaneous emission is in a random direction, it executes a random walk in momentum space with a step length $\hbar k$. The volume of momentum space inhabited by the ion is characterized by this step length and so its temperature is limited by a rate equation comprising the cooling from the laser beam and the heating from the spontaneous decay. The Doppler cooling limit is

$$
T_D = \frac{\hbar \gamma}{2 k_B} \qquad (3.24)
$$

3.2.2 Sideband cooling

The above picture works well for trapped ions as well as free particles [56]. However, there is another way to view laser cooling of trapped ions in the resolved sideband limit. Like any quantum mechanically treated potential well, the trap will have discrete energy levels. For a harmonic potential these levels would be equally spaced by $\hbar\omega_t$ and they would be distinct if $\omega_t \gg \gamma$. This is the resolved sideband limit and can be reached by tight confinement in the trap, which increases the motional frequency ω_t. The resulting energy level diagram for the electronic levels of the atom and vibrational levels of the trap looks like Figure 3.6. Each electronic level has a ladder of vibrational states associated with it, where the vibrational states are separated by much less than the electronic states. A laser tuned to the first red sideband $(\omega - \omega_t)$ would promote an electron from the ground electronic state to the excited electronic state and reduce the vibrational state by one level. Spontaneous emission then causes the electron to return to the ground state having reduced the average vibrational energy in the system[2]. This can be repeated in a form of optical pumping until all the population is carried to the ground vibrational state. At this point, absorption on the red sideband will cease and the atom has been cooled into the ground state of the trap.

---

[2] The Franck-Condon principle will ensure that the strongest transition in spontaneous decay will not change the vibrational quantum number. This is due to the overlap of the wavefunctions.

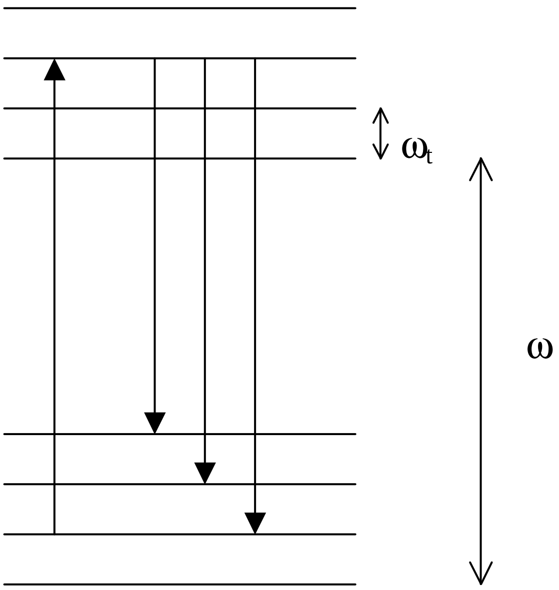

Figure 3.6: Diagram showing the trap and internal levels and radiation applied to the blue sideband

This was first achieved for ^{198}Hg$^+$ in a Paul trap in 1989 [57] for one degree of freedom. A narrow, single-photon quadrupole transition S$_{1/2}$ - D$_{5/2}$ was used as the carrier. This ultra-violet transition at 281.5nm was driven using a frequency doubled dye laser. Initially the ion was Doppler cooled on the S$_{1/2}$ - P$_{1/2}$ dipole transition such that the mean number of vibrational excitations present ($\langle n \rangle$), was $\langle n \rangle \approx 12$. After sideband cooling was applied, it was measured to be in the ground state 95% of the time (i.e. $\langle n \rangle = 0.05$). In order to increase the cooling efficiency, the D$_{5/2}$ state was mixed with the P$_{3/2}$ state using a laser at 398nm. This decreased the decay time from the excited state back to the ground state.

A similar single-photon method was used to cool a ^{40}Ca$^+$ ion in a Paul trap in 1999 [42] achieving occupation of the ground state with probability 99.9%. The scheme used here is similar to that used in the Hg$^+$ experiment. The ion is initially Doppler cooled on a strongly allowed transition (i.e. S$_{1/2}-$P$_{1/2}$) and then a forbidden (narrow) transition is used for sideband cooling (i.e. S$_{1/2} -$ D$_{5/2}$). The D$_{5/2}$ level has a lifetime of around 1s, which is so long that it must be mixed with the P$_{3/2}$ level with a laser at 854nm to provide a route for spontaneous emission back to the ground state for efficient cooling. Doppler cooling takes the average vibrational state to around $n = 10$ but this depends on the stiffness of the trap.

3.2.3 Stimulated Raman cooling

Sideband cooling on a quadrupole transition as above requires very narrow band lasers so as to resolve the sidebands. Another technique is to use stimulated Raman transitions on the sidebands to cool the ions [44]. This has been used to reach the ground state of a Paul trap [8].

This technique uses two-photon transitions between metastable hyperfine levels in the ground state of Be^+. This process is represented in Figure 3.7, where the frequency difference between the hyperfine levels is equal to the difference in frequency between the two beams plus the frequency associated with one motional quantum in the trap. Each transition therefore removes one vibrational quantum from the ion and so the ion is cooled. To achieve a narrow linewidth for the two photon transition, the lasers must be detuned (by Δ) from the frequency of the $S_{1/2} - P_{1/2}$ transition.

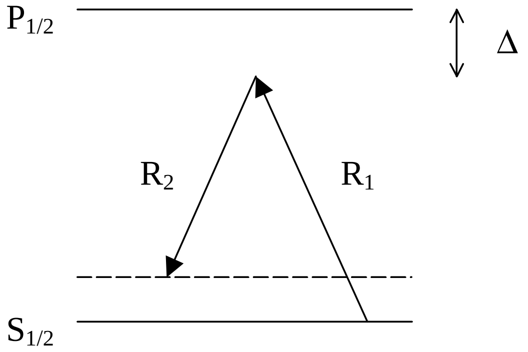

Figure 3.7: Diagram showing Raman cooling scheme

The two laser frequencies required can be derived from the same laser using an acousto-optic modulator. It takes advantage of the form of line broadening in dye lasers. Here the 'instantaneous' linewidth is very low[3], but continually jumps randomly giving a large linewidth (~MHz) over longer times. Since the two beams are derived from the same laser, the random jumps in frequency of the source laser are cancelled out in the combined effect of the two beams. Also, since the process is non-resonant, changes in Δ do not affect the absorption amplitude strongly.

Initial Doppler cooling on a strong dipole transition cooled the Be^+ ion to the Lamb-Dicke regime. The trap confinement was strong enough (and the transition quick enough) that $\omega \approx \gamma$ and the Doppler precooling left the

---

[3] Linewidth is transform limited over a sample time of the order of $\sim 10^{-3}$s which gives a linewidth of the order of kilohertz.

ion with an average motional excitation $\langle n \rangle \approx 1$. The Raman beams were then applied on the narrow Raman transition (to drive the red sideband), which cooled the ion to the ground state about 92% of the time. It should be noted that, whilst the above work on Hg^+ only cools in one dimension, this experiment on Be^+ was performed such as to cool all three degrees of motion. This was possible due to the cooling lasers being at an angle to the trap axes so has to have some component of the laser beam parallel to each axis and involved tuning the laser to the required frequencies to hit red sidebands for each of the motions along different axes.

Further work has improved the ground state cooling and two Be^+ ions have been cooled to the ground state [45] with probability 90% for the COM mode and 99% for the stretch mode. The method for measuring the ground state occupation is to look for absorption on the red sideband. The asymmetry between the absorption on the red and blue sidebands will increase as the ion approaches the ground state. Since there are no levels below the ground state, the laser will decouple from the ion and absorption will cease. Comparing the red and blue sidebands will give an average probability that the ion is in the ground state.

3.2.4 Cooling using electromagnetically induced transparency

Another scheme for cooling to the ground state of the trap was proposed in [46]. It builds upon the sideband cooling method but has several advantages. A three level system is used with two laser beams as shown in Figure 3.8. A strong laser is used to drive the transition $|r\rangle$ - $|e\rangle$. This laser has intensity I_r and detuning Δ_r to the blue side of the transition. A weak laser is used to probe the transition $|g\rangle$ - $|e\rangle$, with intensity I_g and detuning Δ_g (where $I_g \sim 0.01 I_r$ and the detuning is to the blue). The intense laser produces an AC Stark shift ($\Delta\omega$) on the transition which defines the spectrum which the weaker laser sees. As shown in Figure 3.8, if the weak laser is scanned over the transition, there is a broad absorption at $\Delta_g = 0$, no absorption at $\Delta_g = \Delta_r$ and strong absorption at $\Delta_g = \Delta_r + \Delta\omega$. The condition $\Delta_g = \Delta_r$ corresponds to a dark resonance. By choosing the parameters carefully, the bright resonance can be aligned with the first red sideband of the trap's motional frequencies and the dark resonance aligned with the carrier $\Delta n = 0$ transition. There is then strong cooling of the ion, without unwanted excitation of the carrier. This is highly desirable for cooling, since it removes some of the major problems associated with sideband cooling.

Excitations on the carrier can be a major source of heating. This is

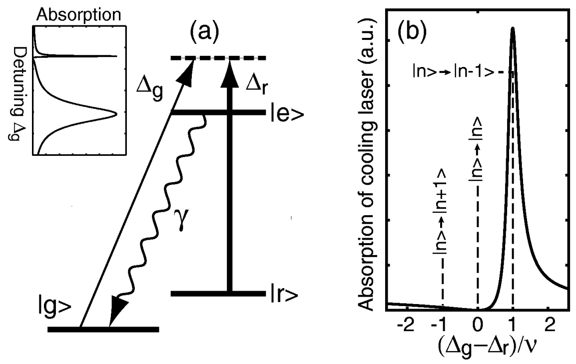

Figure 3.8: (a) shows the how the lasers are applied to the states of the ion. (b) shows the absorption in relation to the motional states of the trap. From [46].

particularly true if the laser power is increased and so attempts to increase the cooling rate by increasing laser power could be counter-productive. Removing the carrier absorption removes the major source of off-resonant excitation which causes this heating. Similarly, the laser does not need to be as highly stabilised for the EIT scheme as for sideband cooling. Again this is due to the fact that a wider laser linewidth will not cause transitions on the carrier. EIT cooling has several other advantage besides this. This scheme does not rely on strong confinement of the ions, and so strong dipole transitions can be used (i.e. they do not have to satisfy $\gamma \ll \omega_t$), which will increase speed. This scheme will also work for several modes of vibration at the same time.

The EIT cooling scheme was first demonstrated in Innsbruck [47]. A single Ca^+ ion was cooled to the ground state of a Paul trap with reasonable probability. A magnetic field of 0.44mT is applied to the ion. The Zeeman split ground state and the $P_{3/2}(m_J = 3/2)$ excited state serve as the three levels ($|g\rangle, |r\rangle, |e\rangle$) described above. Choosing the polarisation of the lasers allows the transitions to be selectively excited.

Initial Doppler precooling leaves the ion moderately close to the ground state (mean excitation numbers ~ 10). EIT cooling in one dimension then cools the ion to mean vibrational quantum numbers ~ 0.1 (ie. 90% ground state probability). Three-dimensional cooling was also demonstrated, but with slightly less success (ranging from 58 to 74% ground state probability). The apparatus was not designed for this experiment and so the cooling efficiency could be improved by altering the angle between the laser beam and the B-field [47].

3.2.5 Sympathetic cooling

Sympathetic cooling is a method of cooling an ion (or ions) without directly illuminating them with laser light. If there are several ions in the trap, then cooling one of them may sympathetically cool the others. This is achieved via the coulomb interactions between the charged ions. Sideband cooling one of a pair of calcium ions in a linear rf trap has cooled them both to close to the ground vibrational state [48]. Cooling only one of the modes (i.e. for use as the bus qubit) gives a probability of being in the ground state of 95%, whilst the other modes (spectator) have average vibrational quantum numbers between one and two.

Proposals for future experiments have included sympathetic cooling as a favourable technique for cooling the motional modes of ion strings [49]. If different species of ions are used for the qubits and the cooling, then the laser light used for cooling will not interfere with entangled qubit states needed for quantum information processing. The Coulomb interactions which mediate sympathetic cooling are of sufficiently long range that the delicate entangled states should not be disturbed.

3.3 Ion traps in quantum computing

Any classical computer can be modelled as a network of logic gates (for instance the NAND gate) which will fundamentally act the same (in certain ways defined by information science) as any other classical computer. Similarly, any quantum computer can be modelled in terms of a universal system of gates which in some sense reproduces the properties of any quantum computer. An example set of operations would be CNOT, SWAP and universal rotation, which apply to states in a Hilbert space.

Ion traps were first put forward as promising candidates for a realisation of a quantum computer in 1995 [5]. The ion trap has several features which may facilitate such a realisation:(i) it is scalable in such a way as to allow, in principle, any number of qubits to be used in a calculation (ii) decoherence is naturally lower than in some other systems suggested (iii) the final measurement on the system to retrieve the answer can be made with arbitrary efficiency. Ion traps must deal with two conflicting requirements of quantum information processing. To minimise decoherence, the qubits must be decoupled from the environment and in an ion trap, they are cooled so as to be well localised in ultra-high vacuum conditions. The qubits must also be able to interact strongly with one another to allow exchanges of information between them, which is achieved by the Coulomb interaction between the ions. Decoherence is seen to be one of the major hurdles to be overcome if a large scale quantum computer is ever built.

3.3.1 The Cirac-Zoller scheme

All of the proposals for quantum information processing in ion traps have in some way built upon the CZ (Cirac and Zoller) scheme proposed in [5]. That scheme is described here first and then some of the new proposals are considered. In the CZ scheme, each ion in the trap acts as one qubit. Consider the energy level diagram for calcium (Figure 3.9). The ground $S_{1/2}$ level and the metastable (lifetime $\sim$ 1s) $D_{5/2}$ level form the $|0\rangle$ and $|1\rangle$ states of the qubit. The $S_{1/2}$–$P_{1/2}$ transition is used to detect the state of the ion and also for Doppler cooling. So far only rf traps have been used for experiments in the field of ion trap quantum information processing. In a linear rf trap, the ions are cooled to lie in a linear crystal (string) along the axis of the trap, where heating from the micromotion is minimal. However, due to imperfections (e.g. patch potentials) in the trap, compensation electric fields may be needed to ensure that the ion crystal lies along the axis of the trap where the micromotion is theoretically zero. The ions should be kept far enough apart by Coulomb repulsion that they can be considered to be well localised. It is then possible to address the ions independently with

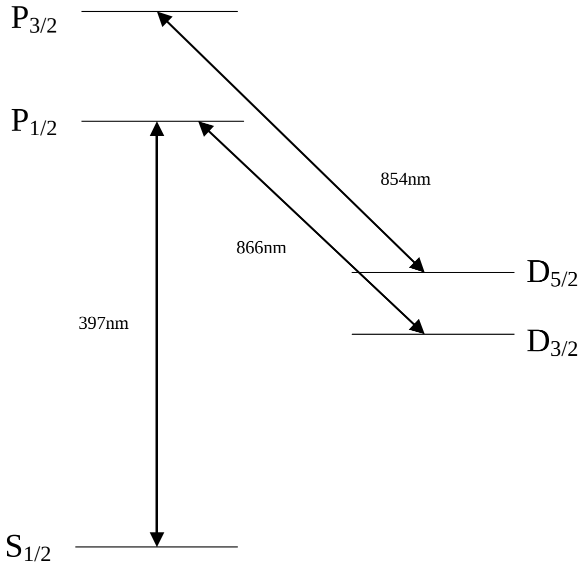

Figure 3.9: Energy level diagram of calcium

a suitably focussed laser beam. So far this has only been achieved for a maximum string of two ions by one group [58].

When the ions are sufficiently cool, the normal modes of vibration will become apparent. As long as the frequencies of the normal modes are well separated, they can be excited separately. The centre of mass motion can then be used as a means of transferring information between the ions, acting as a bus qubit.

The CNOT operation is somewhat similar to the classical XOR and can be represented as $|a, b\rangle \longrightarrow |a, a{\oplus}b\rangle$ where $\oplus$ is XOR (addition modulo 2) and $a, b\ \epsilon\{0, 1\}$. Only two groups [59] [60] have so far demonstrated the CNOT operation in an ion trap. This was done in an rf trap using only a single ion. The two qubits were the internal (electronic) state and the vibrational state. The method is still applicable to greater numbers of qubits using the SWAP operation. Here any two internal states of the ion can be processed by CNOT by swapping the internal state of one of the ions (a) with the bus qubit. The CNOT operation can then be used as described below with the bus as the target qubit and ion (b) as the control. Finally, the states of the bus and ion (a) can be swapped, completing the operation. The CZ scheme requires individual addressing of the two ions, but this requirement may be relaxed under certain circumstances.

We can write the state due to the excitation of the trap normal modes as $|n_1\ n_2\ n_3 \ldots\rangle$ and the internal state as $|i\rangle,\ i = 0, 1$. So the four states of the system are

$$|0\ 0\rangle \equiv |0\ 0\ 0 \ldots\rangle \otimes |0\rangle \tag{3.25}$$

$$|0\ 1\rangle \equiv |1\ 0\ 0 \ldots\rangle \otimes |0\rangle \tag{3.26}$$

$$|1\ 0\rangle \equiv |0\ 0\ 0 \ldots\rangle \otimes |1\rangle \tag{3.27}$$

$$|1\ 1\rangle \equiv |1\ 0\ 0 \ldots\rangle \otimes |1\rangle \tag{3.28}$$

This scheme requires an extra (auxiliary) level (see Figure 3.10) to facilitate some of the operations. It is assumed that the system is initialised such that there are no vibrational quanta present in the trap.

To execute the CNOT operation between the vibrational state and the internal state of the ion the following scheme could be used

(i) a $\pi/2$ pulse at the carrier transition ($\Delta n = 0$) with frequency ω_0. This mixes the $|0\ 0\rangle$ and $|0\ 1\rangle$ with the $|1\ 0\rangle$ and $|1\ 1\rangle$ states respectively.

(ii) a 2π pulse at frequency $\omega_{aux} + \omega_t$ which is the blue sideband of the transition between the excited electronic state and the auxiliary level and will simply change the sign of the coefficient of $|1\ 1\rangle$ state (assuming all levels not given in Figure 3.10 are empty).

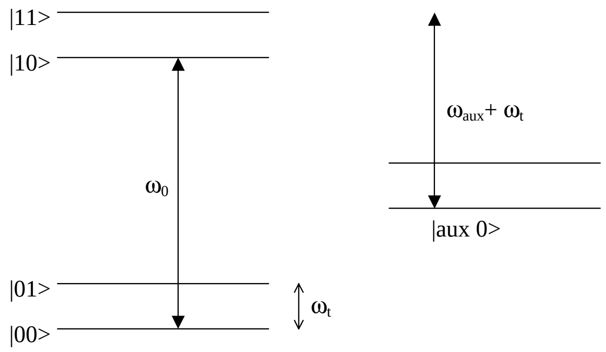

Figure 3.10: Energy levels used in executing the CNOT operation

$$|0\ 0\rangle \longrightarrow \quad |0\ 0\rangle \tag{3.29}$$
$$|0\ 1\rangle \longrightarrow \quad |0\ 1\rangle \tag{3.30}$$
$$|1\ 0\rangle \longrightarrow \quad |1\ 0\rangle \tag{3.31}$$
$$|1\ 1\rangle \longrightarrow \ - \ |1\ 1\rangle \tag{3.32}$$

(iii) a $\pi/2$ pulse at frequency ω_0 displaced in phase by π from the first. This will undo step (i) for any portion of the wavefunction not affected by step (ii), but for the portion which has changed sign in step (ii), it will continue the rotation started in step (i) and the electronic state will be flipped.

Thus the overall operation is that the motional state $|n_1\ n_2\ n_3 \ldots\rangle = |0\ 0\ 0 \ldots\rangle$ will be left unchanged since steps (i) and (iii) will simply cancel each other out. However if the state $|1\ 1\rangle$ is occupied then this component will change sign in step (ii) and steps (i) and (iii) add constructively causing the internal state to be flipped. This gives the truth table

$$|0\ 0\rangle \longrightarrow |0\ 0\rangle \tag{3.33}$$
$$|0\ 1\rangle \longrightarrow |0\ 1\rangle \tag{3.34}$$
$$|1\ 0\rangle \longrightarrow |1\ 1\rangle \tag{3.35}$$
$$|1\ 1\rangle \longrightarrow |1\ 0\rangle \tag{3.36}$$

Detection of the final state of the ion after the operation may be achieved by looking for fluorescence on a strongly allowed transition. For instance in Ca^+ this may be done on the 397nm ($S_{1/2}$–$P_{1/2}$) transition (see Figure 3.9). If a laser is applied at 397nm then if population is present in $S_{1/2}$ ($|0\rangle$) then fluorescence will be detected at 397nm perpendicular to the laser beam due to spontaneous decay as the electron cycles between the two levels. If it is in the $D_{5/2}$ ($|1\rangle$) state then there will be no fluorescence. Although the CNOT operation can be applied to superpositions of the states (and superpositions synthesised by fractional π/x pulses) the detection will obviously collapse the state into one of the basis states.

This scheme has several constraints placed upon it. Notably, that the ions must be cooled to the ground state of the trap with high probability; the required presence of an auxiliary electronic level; the need to address the ions individually; and speed considerations due to the number of laser pulses required to operate the gate. The work described in the next sections considers how some of these constraints may be relaxed.

3.3.2 The wave-packet CNOT gate

This proposal [61] was published by NIST in 1997. It eliminates the need for an auxiliary level (which may be a problem in elements without hyperfine structure e.g. $^{40}\mathrm{Ca}^+$). It also only requires one laser pulse to apply the CNOT transformation between the motional state and the electronic state. This may increase the speed of the gate.

This scheme relies on the fact that the dependence of the Rabi frequency on the Lamb-Dicke parameter (η) is different for different states. The Rabi frequencies (Ω)for the different motional states are given by [62]

$$\begin{aligned} \Omega_{0,0} &= \Omega e^{-\eta^2/2} && (3.37) \\ \Omega_{1,1} &= \Omega e^{-\eta^2/2}(1-\eta^2) && (3.38) \end{aligned}$$

where the subscripts refer to the number of vibrational quanta in the lower and upper levels which are being driven. By careful choice of η, it is therefore possible to arrange that

$$\Omega_{0,0}/\Omega_{1,1} = (2k+1)/4m \qquad (3.39)$$

where k and m are integers. Applying laser light on the carrier which acted as a 4π pulse on the state with vibrational quantum number $n = 0$ (Rabi frequency $\Omega_{0,0}$) would then automatically apply a π (or 3π) pulse on the state with vibrational quantum number $n = 1$ (Rabi frequency $\Omega_{1,1}$). This would obviously change the electronic state for any ion in the $n = 1$ state, but not for those in the $n = 0$ state. This is precisely the operation of a CNOT gate.

This scheme has been demonstrated experimentally [63]. The Lamb-Dicke parameter is changed by altering the strength of the trap. The $n = 0$

and $n = 2$ vibrational levels are used as the control qubit. The fidelity of the operation is given as 95%.

3.3.3 Hot gates

Both Cirac and Zoller [64] and Sørensen and Mølmer [65] have proposed schemes for quantum logic gates which do not require that the ions are initially cooled to the ground state of the trap. The former scheme relies on providing an impulse to an ion, the direction of which depends on its state. If the ion is in a superposition, then a Schrödinger cat-like state is formed. With the wave packets spatially separated, the state of a second ion may be conditionally changed to complete a CNOT gate. This scheme may be hard to generalise to large numbers of ions.

The Sørensen and Mølmer scheme has received more interest. This scheme can be used to perform quantum gates by applying a series of pulses to the ions. Fundamentally, the scheme allows the coherent manipulation of the electronic states of two ions irrespective of the motional state. It uses two lasers to excite two photon transitions for the two ions, which pass through intermediate vibrational states without populating them (Figure 3.11). Different paths interfere constructively such that the Rabi frequencies of the transitions are independent of the vibrational quantum number. It requires that the ions are deep into the Lamb-Dicke regime.

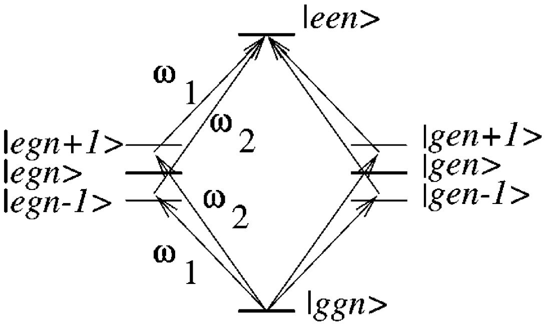

Figure 3.11: Diagram showing the excitations needed to create entanglement between two hot ions (from [65]). $|ggn\rangle$ is the state where both ions are in the ground state and there are n vibrational quanta, $|een\rangle$ is the state where both ions are in the excited electronic state and there are n vibrational quanta.

3.3.4 Other schemes

Several other schemes for quantum information processing in ion traps have been proposed. A scheme which may allow faster gates by harnessing the AC Stark shift was put forward in [66]. In the CZ scheme, increasing the laser power to increase the speed of the operations may cause the gate to fail due to the shift in the resonant transition and excitation of off-resonant transitions. This is circumvented by carefully choosing to use specific laser intensities where the AC Stark shift allows the transfer of vibrational quanta as the electronic transitions are excited. This was extended [67] to work for ions not cooled to the ground state by using an interference method over several paths through the motional states similar to that of Sørensen and Mølmer [65].

3.3.5 Entanglement and manipulation of trapped ions

Entanglement is an important resource in quantum information processing, as it is what, in large part, separates quantum information processing from what can be achieved in the classical world. Producing entangled states deterministically is necessary for quantum information processing to become a reality. This was first demonstrated using two Be^+ ions in a rf trap in 1998 [69]. The ions were entangled using precisely timed laser pulses.

An additional scheme to produce entanglement was proposed in 1999 [70]. This scheme was similar to that proposed for hot gates and does not require that the ion is in a well-defined motional state of the trap. It relies on the interference between different paths through the vibrational levels, but does not populate any of the intermediate states. It leaves the vibrational state as it found it and is independent of the vibrational quantum number. A similar scheme was used to entangle four ions [71]. This scheme was not immune to heating due to the small detunings used for the two-photon transitions, but did produce the first demonstration of entanglement of four ions. The fidelity of the entanglement is quoted as 0.57 for four ions.

Coherent manipulation of the ions to give arbitrary rotations has also been demonstrated at Innsbruck [60]. The $\mathrm{S}_{1/2}$-$\mathrm{D}_{5/2}$ transition is driven in a Ca^+ ion to produce an arbitrary state. The coherence of these states is measured by Rabi oscillations and is discussed below. Rather than use a single operation to generate an arbitrary superposition (of trap and internal states), it is possible to use a sequence of simple operations [72]. This has been used experimentally to produce various superpositions [73]. To see how it works, consider the process in reverse. Start with an arbitrary (but known) superposition between two electronic states and the lowest four motional states. It is necessary that there is no extraneous population in higher motional states. The first step is to coherently drive the population from $|\uparrow\rangle|n=3\rangle$ to $|\downarrow\rangle|n=3\rangle$ to empty the $|\uparrow\rangle|n=3\rangle$ state. This can be done by applying a Rabi pulse for a specific duration since the state is known. The second step is to coherently drive the $|\downarrow\rangle|n=3\rangle$ population into the state $|\uparrow\rangle|n=2\rangle$. This two step clearing process can be repeated for successive levels until the ground state is reached. Simply reversing the order of the pulses will create an arbitrary superposition from ions cooled to the motional ground state.

Experiments have also been performed showing that an ion has been coupled to the modes of a high finesse cavity [74]. The ion thus interacts with a standing wave optical field. By placing the ion at an antinode (node) the carrier (sideband) excitation can be suppressed. This suppression of the unwanted carrier excitation may allow greater laser intensities to be used to increase the speed of the gates. Although this was proposed in the original CZ scheme, experimental realisations have so far only used a travelling wave schema. This work involved the cooling of a single trapped ion and then positioning it with nanometer precision at either a node or antinode.

The overall architecture of a quantum computer has had comparatively little attention so far due to the difficulties of even operating a single gate. However, a recent proposal has been made for such an architecture [75]. Here ions are stored in miniature traps which act as a memory. As the ions are required in the computation, they are moved to a separate linear trap interaction region. Quantum gates would then be performed in the interaction region and then the ions split and moved back to the memory region. The next set of ions would then be moved into place. Whilst much of this is still several years away, both the movement of one ion between traps and the splitting of two ions from a single trap to two distinct traps has been demonstrated [76]. Moving a single ion caused no additional heating over an ion left in a single trap. For splitting two ions, the heating was considerable (~ 150 quanta in 10 ms), but the process was successful 95% of the time.

3.4 Decoherence

Decoherence has been identified as the major hurdle to overcome in the quest to build a working quantum computer [77] [78]. It is inherent in any physical system which can contain information in the form of quantum superpositions and is a problem since in time it will distribute the information throughout the whole environment. The operations of a quantum computer are taken to be governed by unitary evolution. In fact, it is thought that the description of any isolated quantum system is unitary. However in general, any subsystem will not undergo unitary evolution. To achieve unitary evolution of a subsystem, the matrix describing evolution of the universe must be block diagonal i.e. there must be no interaction between the subsystem and anything outside the subsystem. In practice, this impossible goal motivates us to consider the 'cleanest' systems available, although quantum error correction should also be considered to reduce the impact of any remaining decoherence. Ion traps fare well under these considerations [79]. Some possible sources of decoherence in ion traps are listed below. For further discussion see [88].

3.4.1 Possible sources of decoherence

Here, decoherence is considered to be any reason why the reliability of a quantum computer realised using an ion trapping method could be compromised. The concept of decoherence will be split roughly into two kinds: (i) decoherence of the quantum state of the register and (ii) errors introduced due to applying imperfect evolution.

3.4.2 Decoherence of the register

The state of the ions in the trap is given by two different degrees of freedom, the vibrational state in the trap and the internal (electronic) state of the ion. Decoherence of the internal state has been studied for many years due to its importance in frequency standards experiments and in atomic clocks. Spontaneous decay can be ignored by suitable choice of qubit levels such as the ground state and a metastable state (e.g. $\mathrm{D}_{5/2}$ in calcium which has a lifetime of ~ 1.2s [80]), which have long decay times.

Externally applied fields may also contribute to decoherence of the internal state. Any applied magnetic field will alter the energy difference between the electronic states (i.e. the Zeeman effect) which could lead to errors if the magnetic field strength is not known precisely. The internal levels are less sensitive to electric fields (i.e. the Stark effect) than to magnetic fields.

The vibrational levels of the trap are likely to be affected by different parameters since they will display much smaller separation in energy. Also the trap potential is generated artificially so will be subject to any instability in the trap parameters. First among these are the electric and magnetic fields applied to the trap. Obviously, unwanted shifts in the potential over time could cross-populate the normal modes, causing excitement of non-centre of mass modes. This is not only a redistribution of energy among the states of the trap, but also takes the system out of the computational basis states.

Since the trap states are close together, they may couple radiatively through the thermal electromagnetic field. Collisions with background gas in the vacuum system may also cause decoherence, either redistributing energy through the normal modes or transferring energy to or from the different modes.

3.4.3 Errors induced in evolution

These errors are caused by imperfections in the methods used to apply logic operations. One example of a possible cause would be incorrectly timed laser pulses used to transfer population between states. If the initial state were not prepared with enough purity then unwanted population may occur in states which are not part of the computational basis. This could destroy the fidelity of subsequent operations since the unwanted population could be transferred back into the computational basis states. Since the implementation of the logic operations involves Rabi oscillations it is necessary to know the Rabi frequency precisely. This depends on such parameters as the energy separation between the levels and the intensity of the lasers. If the intensity of the laser or the separation between the levels changes, then this will limit the fidelity of the operation.

Since superposition and entangled states are extremely fragile, care must be taken to stop spurious 'measurements' of the state of the system collapsing the desired wavefunctions.

3.4.4 Experimental consideration of heating and decoherence

Both the group at Innsbruck [81] and the group at NIST have studied decoherence in rf traps. The former measured coherence times by studying Rabi oscillations on a state initially cooled to the ground state of the trap. To achieve a picture of Rabi flopping, they would drive the system on the blue sideband. Each data point would consist of a large number of experiments with the system driven for a set time t. After driving for time t the state of the ion would be measured by looking for fluorescence on the $\mathrm{S}_{1/2}$-$\mathrm{P}_{1/2}$ transition. This forces the superposition state to collapse. Repeating this many times for the same value of t will yield a probability of the ion being in the $\mathrm{D}_{5/2}$ state. Repeating this for many values of t gives the Rabi oscillations of the ion. It was found that the fringe contrast was above 0.5 for about 20 periods. Thus decoherence was small over the period of a few oscillations (a reasonable estimate for the length of a gate operation) that quantum gate operations could be contemplated. This group also measured heating of about one phonon in 190ms for ions cooled to the ground state and left without laser interrogation.

A comprehensive study on heating rates in various traps has been done at NIST [82]. The results are inconclusive, but it appears that the main sources of heating may have been identified. Thermal (Johnson) noise from the resistive elements in the trap electronics is all but discounted. The two major factors identified are the trap size and fluctuating patch potentials. The lowest heating reported by this group is about 1 motional quantum in 150ms [83]. The heating scaled inversely with trap size, consistent with a power law of d^{-4}, so large traps may have significant advantages. Later work [76] has shown that shielding of trap electrodes from ion deposition and taking additional care over electrode surface imperfections may reduce heating.

3.4.5 Decoherence-free subspaces

By encoding the logical qubits in two ions, some of the worst aspects of decoherence can be minimised. Encoding a logical $|1\rangle$ as $|\uparrow\downarrow\rangle$ and $|0\rangle$ as $|\downarrow\uparrow\rangle$ is said to code the qubit in a decoherence-free subspace. The combined state of the two ions is then immune from certain types of decoherence (collective dephasing). This protects the information from being lost if ions encounter external magnetic fields and also removes the dependence on the phase of the ions. Use of such subspaces was demonstrated in [84].

3.5 Penning traps for quantum computation

In comparison to rf traps, Penning traps may seem an unusual choice for quantum information studies. Certainly, there has been much less interest in using these traps so far. However, there could be significant advantages to using Penning traps if some obstacles can be overcome. Significantly, Penning traps may suffer much less from decoherence than rf traps. Our Penning traps have a size on the order of 1cm, in comparison to rf traps on the order of 200 μm [82]. Since the heating rates have been shown to scale as d^{-4}, where d is the characteristic size of the trap, our trap may show greatly reduced heating. Another major source of heating identified in the above reference is that due to fluctuating patch potentials. Since the Penning trap does not use rf frequencies, the heating due to this may be lower also.

Unfortunately, Penning traps have several other difficulties to overcome. Foremost of these is probably that the ions are not well localised in the standard configuration. The ions rotate around the trap at the magnetron frequency. Disc-like crystals of cold ions may be formed. To image or address the ions, it may therefore be required to synchronise the driving lasers and detection system with the magnetron motion. This gating technique has been demonstrated at NIST by applying a rotating electric field to an ion crystal in a Penning trap [85]. The magnetron rotation is then phase-locked to the field and imaging of the crystal was demonstrated. Axialisation [90] may also overcome this problem. Here an rf electric field is used to drive an ion into the centre of the trap by coupling the magnetron and laser-cooled cyclotron motions. Since the ion is localised at the centre of the trap, the magnetron motion is suppressed. Laser cooling is also complicated in the Penning trap by the large magnetic field. This induces large Zeeman splittings between the fine structure levels and additional lasers are generally required to cool the ion efficiently and prevent optical pumping.

The long term goal of our experiments at Imperial College, is to study the decoherence of motional states in the Penning trap. This thesis details the first half of that work, which is an ongoing project with funding for a further three years. Since joining the group, I have commissioned laser systems to Doppler cool Ca^+ and trapped and laser cooled Ca^+ in our trap run in rf mode. This is easier than cooling in a Penning trap due to the requirements for fewer lasers and the availability of absolute wavelength tests for the lasers (an unusual type of hollow cathode lamp has been built for this purpose). The ions were then trapped in a combined Penning/rf trap and the magnetic field gradually increased. This provided a method of finding the required laser frequencies for the $\approx$1T magnetic field used for the Penning trap. A narrow linewidth ($\sim$kHz) Ti:Sapphire laser has been commissioned to perform sideband cooling. To complete the experiments, ions will be trapped using a superconducting magnet with a stable magnetic field, and sideband cooled to the ground state of the motion. Measurements of the coherence time will be measured using Rabi flopping. This thesis describes the work done for the early part of the project. This runs up to and includes the commissioning of the narrow linewidth Ti:Sapphire laser.

Chapter 4

A model of laser cooling using the rate equation approach

This chapter describes work done to simulate laser cooling on a computer, using Excel and Visual Basic. The rate equation approach is described and the equations derived for the laser cooling of a four level system. Also, the applicability of this approach is considered and the limitations of this model are compared with a real ion in a real Penning trap. Although this method was designed to work for a generic four level system, the model has been tied to the parameters of Ca^+ in a magnetic field of 1T. With realistic parameters thus included, the model elucidates the process of laser cooling in our trap. Further work shows how the model works for a two level system and for a method of controlling the equilibrium temperature of the ions.

The simulations were of interest, since Ca^+ has a different level structure to any species of ion previously laser cooled in a Penning trap. This level scheme requires the use of two equivalent cooling lasers to drive the $S_{1/2}$-$P_{1/2}$ transition. The simulations allowed us to investigate the role of optical pumping between the levels and how this affects the efficiency of cooling.

4.1 The model

4.1.1 The ion

Consider a system consisting of four atomic energy levels in two groups (Figure 4.1). This is taken to be the $S_{1/2}$ and $P_{1/2}$ levels which are Zeeman split by a magnetic field of 1T. For Ca^+, the splitting of the ground ($S_{1/2}$)

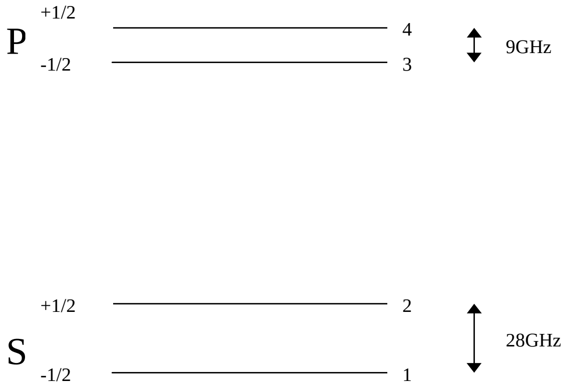

Figure 4.1: The four level system

state is 28GHz and of the excited ($P_{1/2}$) state is 9GHz [1]. The centre wavelength of the transition is 396.959nm. The possible transitions between all the levels are shown in Figure 4.2 relative to the zero field transition and are labelled A, B, C, D for convenience. Since each of the stable ground state levels may be reached by spontaneous decay from either of the $P_{1/2}$ levels, two lasers are required to form a closed loop cooling cycle. In these simulations, the frequency of the lasers can be set to any detuning away from the position of the zero field transition (also the Zeeman splitting can be chosen to be any value), but for the sake of modelling our experiment the detunings are set close to ±9GHz to drive transitions B and C strongly.

A_1, B_1, C_1, D_1 are effective strengths of the transitions A, B, C, D driven by laser 1. Similarly A_2, B_2, C_2, D_2 are the interactions between these transitions and laser 2. The lineshape function of each of these transitions is taken to be a Voigt profile, which is a convolution of a Gaussian and a Lorentzian lineshape. This is physically realistic since the real lineshape function will be a result of the Doppler broadened (Gaussian) width and the natural (Lorentzian) width. Since Excel will not compute Voigt profiles directly, it was necessary to write a macro in Visual Basic to calculate the Voigt function.

The ion cloud is taken to be at thermal equilibrium at all times. This is reasonable since the time for it to come into thermal equilibrium is much smaller than the characteristic time steps of the simulations. The ion cloud is assumed to have a definite temperature defined by a distribution of energies over the different ions. The simulations may also be taken to represent

---

[1] The metastable ^2D states (see Figure 3.9) are not used in this simulation, assuming that the repumping from these levels is complete

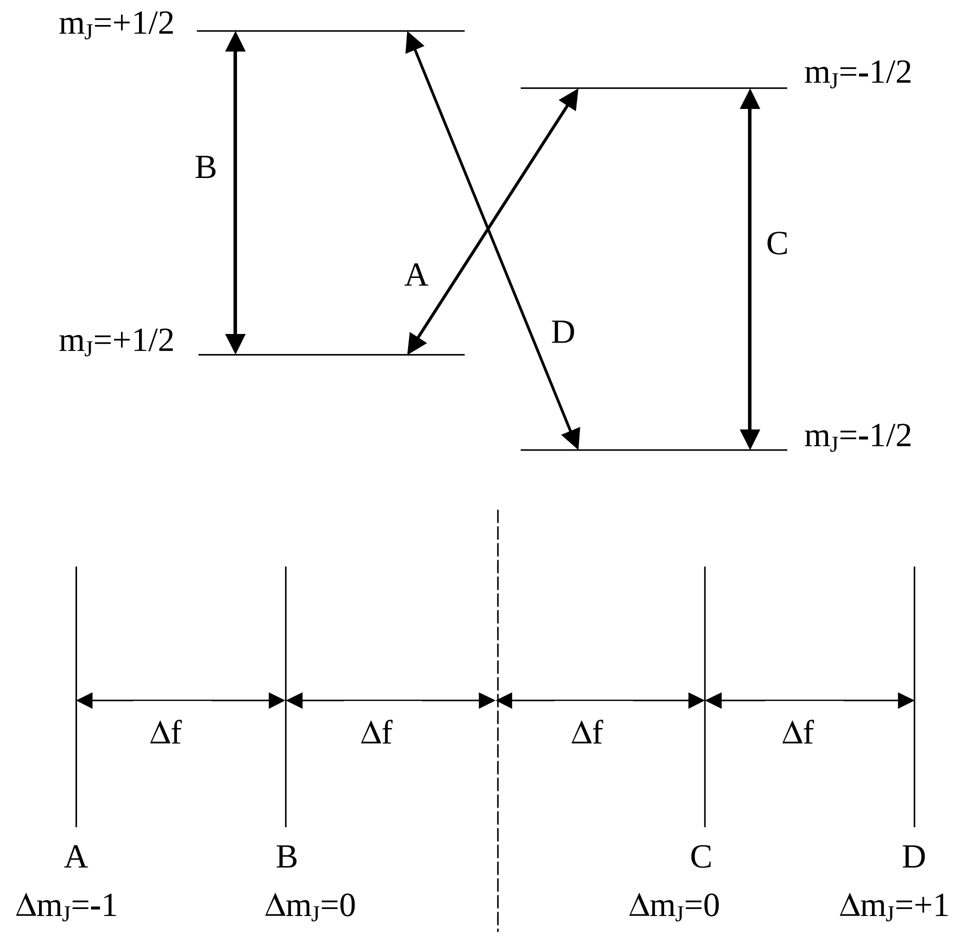

Figure 4.2: Positions of the four transitions relative to the zero field transition

the cooling of a single ion, which will also be assumed to have a definite temperature. This is assumed to be represented by a distribution of energy over time. The quantum effects associated with trapping a particle in a potential well are ignored. This is reasonable since a minimum Doppler width of 20MHz corresponding to a temperature of 50mK would imply a vibrational quantum number in excess of 3000 for a modified cyclotron motion of 350kHz. In our experiments, Doppler cooling will not result in the ion being in the quantum regime.

4.1.2 The Voigt function

The Voigt function is defined as the convolution of a Gaussian and a Lorentzian:

$$V(\alpha) = \int_{-\infty}^{\infty} G(\alpha - x)L(x)dx \tag{4.1}$$

where G and L are normalised Gaussian and Lorentzian profiles. In order to calculate the convolution integral, a macro was written within Excel using Visual Basic. It uses Simpson's rule to approximate the integral by dividing the function into n strips between the integration limits a and b and summing their contributions.

$$\int_a^b f(x)dx \approx \frac{h}{3}\Big\{f_0 + f_n + 4(f_1 + f_3 + \ldots + f_{n-1}) + 2(f_2 + f_4 + \ldots + f_{n-2})\Big\} \tag{4.2}$$

where $h = (b - a)/(n)$.

To obtain realistic values of $V(\alpha)$, the number of strips must be chosen to be large enough that the narrower of the Gaussian and Lorentzian is split into several strips. The integration limits must also be chosen to include most of the area of the overlap between the Lorentzian and Gaussian. An example of a Voigt profile derived from a Gaussian width 0.02GHz and a Lorentzian width 0.02GHz is plotted in Figure 4.4. The integration limits are ±0.4GHz with 200 strips.

4.1.3 Derivation of A_1, A_2, B_1, B_2, C_1, C_2, D_1, D_2

We would like to know the transition rate for each of the possible transitions for each laser. This will depend on the laser detuning, polarisation and

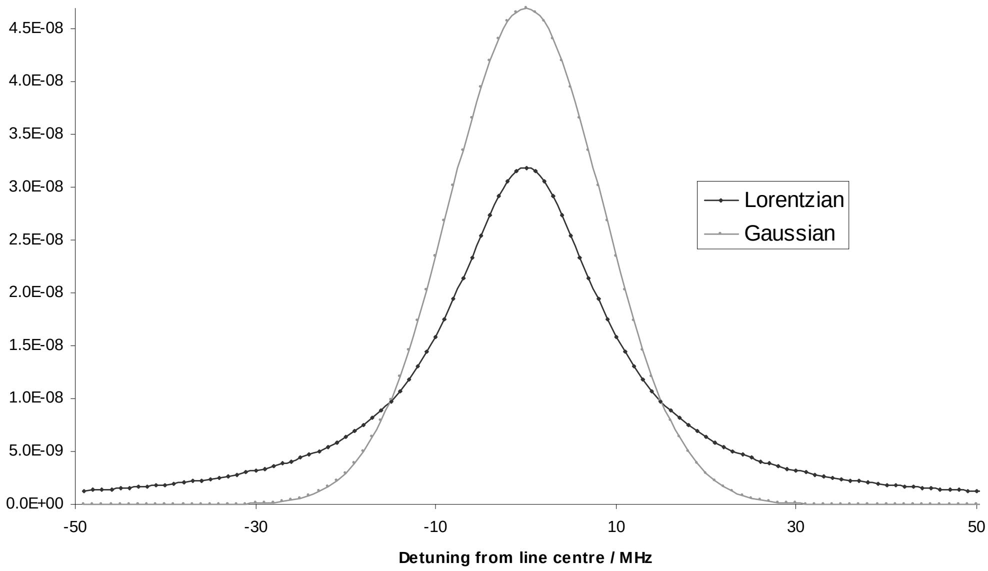

Figure 4.3: Lorentzian and Gaussian profiles

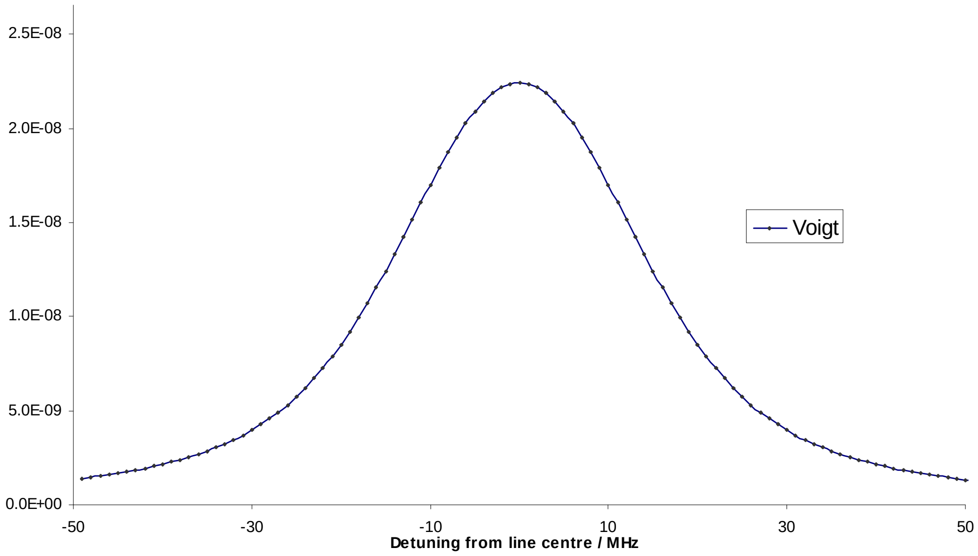

Figure 4.4: Voigt profile derived from the Lorentzian and Gaussian profiles

power as well as the width of the Voigt profile (which changes with temperature). It will also depend on the population in each of the ground state levels n_1 and n_2. We will separate out the population dependent terms by writing the number of transitions per time step δt on transition A due to laser 1 as

$$A_1 \times \frac{n_2}{N} \tag{4.3}$$

where n_2/N is the proportion of the population in level 2 at any given time.

To derive A_1, consider just two levels of a single ion which interact with a laser field $\rho(\nu)$, where ρ is the energy per unit volume per unit frequency interval (Figure 4.5). The centre frequency of the transition is ν_0.

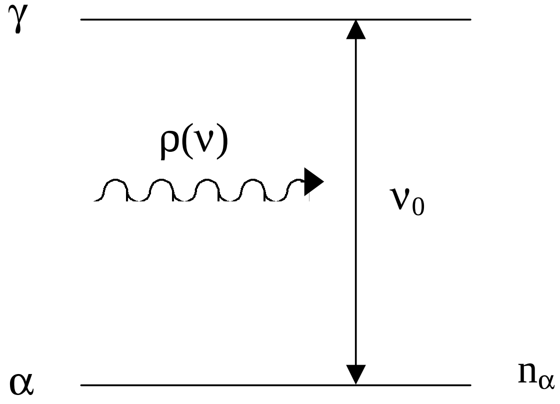

Figure 4.5: Two level system with incident light $\rho(\nu)$

Write the probability per unit frequency of a transition $\alpha \leftrightarrow \gamma$ as

$$\frac{n_\alpha}{N} B'_{\alpha\gamma}(\nu)\rho(\nu) \tag{4.4}$$

which follows from the rate equation approach and uses the Einstein B coefficient. But $B'_{\alpha\gamma}(\nu)$ follows the lineshape function, so integrating over all frequencies gives the transition rate per ion as

$$= \frac{n_\alpha}{N} B_{\alpha\gamma} \int_{-\infty}^{\infty} g(\nu_0, \nu)\rho(\nu) d\nu \tag{4.5}$$

where $g(\nu_0, \nu)$ is the lineshape function, so the number of interactions per ion in time δt is

$$\frac{-n_\alpha}{N} B_{\alpha\gamma} \int_{-\infty}^{\infty} g(\nu_0, \nu)\rho(\nu) d\nu \times \delta t \tag{4.6}$$

But in the rate equation method if we set all Einstein A factors to be equal for simplicity[2], then

$$B_{\alpha\gamma} = \frac{A_{\alpha\gamma} c^3}{8\pi h \nu_0^3} \tag{4.7}$$

where $A_{\alpha\gamma}$ is the Einstein A coefficient for the transition. Since, in practice, the linewidths of our cooling lasers are an order of magnitude lower than the natural linewidth of the Ca$^+$ $S_{1/2} - P_{1/2}$ transition, the laser intensity as a function of frequency will be taken to be a delta function.

$$\rho(\nu) = \rho_{\alpha\gamma} \delta(\nu - \nu_0) \tag{4.8}$$

Also the lineshape (as discussed earlier) is the Voigt function $V(\nu, \nu_0)$.

The number of transitions per ion in time δt can therefore be written

$$\frac{n_\alpha}{N} \delta t A_{\alpha\gamma} \frac{c^3}{8\pi h \nu_0^3} V(\alpha) \rho_{\alpha\gamma} \tag{4.9}$$

where $c\rho_{\alpha\gamma}$ is the intensity of the laser in Wm^{-2} and $V(\alpha)$ is the magnitude of the Voigt profile at laser detuning α.

There is one factor not yet included above. This is the polarisation of the laser. In our four level system, a laser with polarisation along the direction of the magnetic field, which causes the Zeeman splitting, will only excite transitions of $\Delta m_J = 0$. Similarly, polarisation perpendicular to the magnetic field will only excite transitions of $\Delta m_J = \pm 1$. Using θ as the angle between the polarisation and the magnetic field, this introduces a factor of $\sin^2\theta$ for $\Delta m_J = \pm 1$ transitions and $\cos^2\theta$ for $\Delta m_J = 0$ transitions. So comparing with equation 4.3 we may write

$$A_1 = A_A \frac{c^3}{8\pi h \nu_0^3} V(\nu, \nu_0) \rho_1 \delta t \sin^2\theta \tag{4.10}$$

and similarly for the other transitions B, C, D and laser 2.

---

[2] Ignoring the Clebsch-Gordon coefficients for the σ and π transitions. Since the lasers are set to interact strongly only with the π transitions, this alters the results very little.

4.1.4 Derivation of populations n_1/N and n_2/N

This section describes the method used to derive formulae for the proportion of the population in levels 1 and 2 (n_1/N and n_2/N). We will again consider the four level system. It is assumed throughout that the spontaneous decay out of levels 3 and 4 will be fast enough compared to the stimulated transition rate as to completely empty levels 3 and 4. The model will therefore only hold rigorously for the case where transitions are driven below saturation. The magnitude of the Voigt profile of transition A at a detuning corresponding to the frequency of laser 1 will be written V(laser 1, line A).

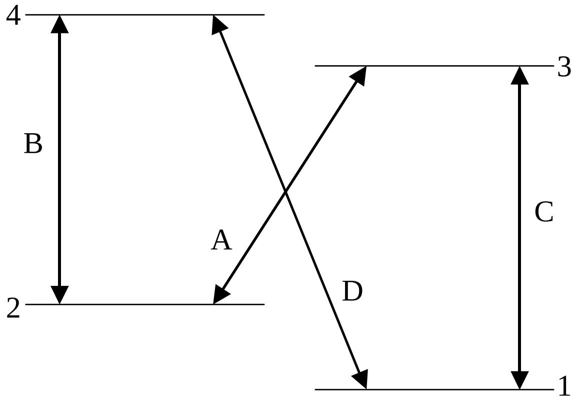

Figure 4.6: Transitions in and out of levels 1 and 2

The rate of population transfer out of level 2 is

$$\begin{aligned} X &= n_2 A \frac{c^3}{8\pi h\nu^3} V(laser1, lineA)\rho_1 \sin^2\theta \\ &\quad + n_2 A \frac{c^3}{8\pi h\nu^3} V(laser2, lineA)\rho_2 \sin^2\theta \\ &\quad + n_2 A \frac{c^3}{8\pi h\nu^3} V(laser1, lineB)\rho_1 \cos^2\theta \\ &\quad + n_2 A \frac{c^3}{8\pi h\nu^3} V(laser2, lineB)\rho_2 \cos^2\theta \\ &= (n_2A_1 + n_2A_2 + n_2B_1 + n_2B_2)/\delta t \qquad (4.11) \end{aligned}$$

and similarly for the population transfer out of level 1

$$Y = (n_1C_1 + n_1C_2 + n_1D_1 + n_1D_2)/\delta t \qquad (4.12)$$

Also, the rate of population transfer into level 2 is $\frac{1}{2}(X+Y)$ since there is no population held in levels 3 and 4 and the branching ratio back to levels 1 and 2 is 1/2. Similarly, the rate of population transfer into level 1 is $\frac{1}{2}(X+Y)$.

Now, considering the system to be in equilibrium, i.e. the rates of transfer in and out of level 2 are equal, gives

$$X = \frac{1}{2}X + \frac{1}{2}Y \tag{4.13}$$

i.e.

$$X = Y \tag{4.14}$$

Now if the total population is N, this implies that $n_1 + n_2 = N$. Therefore

$$\begin{aligned} n_2A_1 + n_2A_2 + n_2B_1 + n_2B_2 = \\ (N-n_2)C_1 + (N-n_2)C_2 + (N-n_2)D_1 + (N-n_2)D_2 \end{aligned} \tag{4.15}$$

i.e.

$$\frac{n_2}{N} = \frac{C_1 + C_2 + D_1 + D_2}{A_1 + A_2 + B_1 + B_2 + C_1 + C_2 + D_1 + D_2} \tag{4.16}$$

and

$$\frac{n_1}{N} = \frac{A_1 + A_2 + B_1 + B_2}{A_1 + A_2 + B_1 + B_2 + C_1 + C_2 + D_1 + D_2} \tag{4.17}$$

4.1.5 Cloud size and addressing the ions

So far, it has been assumed that all the trapped ions are addressed by the laser beam at once. This is not the case in general, especially when the ions are hot and thus the cloud size is large. The ion cloud will be considered to shrink as the temperature drops, but will not be allowed to shrink lower than the size of the laser beam. This simple model has roughly the same behaviour as the experimental reality, since the magnetron motion is cooled imperfectly, but ignores space charge effects.

First, consider the size of the cloud in one dimension. For simplicity's sake we will consider the dimension running through the endcaps of a Penning trap. The ions are trapped in a simple harmonic potential in this dimension (Figure 4.7), and so the potential energy can be written $V = \zeta x^2$ and the ion temperature will determine the potential V_1 (which is an approximate upper bound on the ions' energy). Writing $2x_1$ as the spatial extent of the cloud gives

$$V_1 = \zeta x_1^2 \tag{4.18}$$

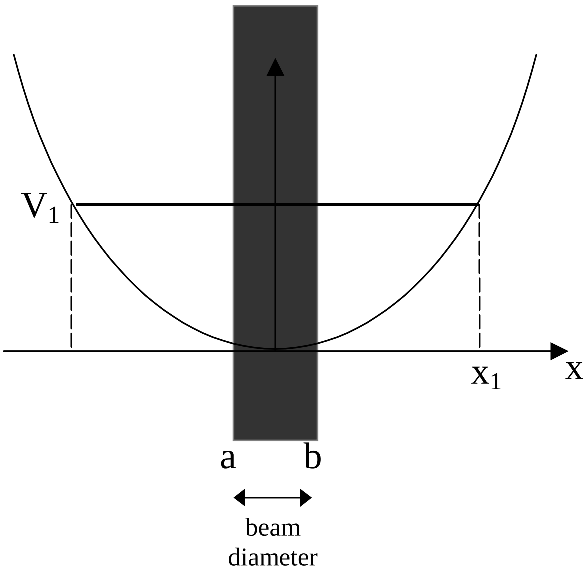

Figure 4.7: Ions in a simple harmonic potential addressed by a laser beam

Taking the edges of the laser beam to be at $x = a$ and $x = b$, then the shaded area of the graph (Figure 4.7) corresponds to the number of ions addressed.

$$\begin{aligned}\text{Shaded area} &= (b-a)V_1 - \int_a^b V dx \\ &= (b-a)\zeta x_1^2 - \frac{1}{3}\zeta(b^3 - a^3)\end{aligned} \tag{4.19}$$

The total area corresponds to the total number of trapped ions

$$\begin{aligned}\text{Total area} &= 2V_1 x_1 - \int_{-x_1}^{x_1} \zeta x^2 dx \\ &= \frac{4}{3}\zeta x_1^3\end{aligned} \tag{4.20}$$

So the fraction of ions addressed is

$$\frac{(b-a)x_1^2 - \frac{1}{3}(b^3 - a^3)}{\frac{4}{3}x_1^3} \tag{4.21}$$

The axial frequency of a Penning trap is

$$f = \sqrt{\frac{4eU}{m(2z_0^2 + r_0^2)}} \tag{4.22}$$

(see Section 3.1.1) which for our trap parameters gives $f = 175$kHz. Finding solutions for the simple harmonic equation gives

$$\zeta = \frac{(2\pi f)^2 m}{2} \tag{4.23}$$

where m is the mass of the Ca^+ ion, therefore

$$\zeta = 4.01 \times 10^{-14}\text{kgs}^{-2} \tag{4.24}$$

Now putting V_1, the energy of the ions, as equal to $k_B T$ gives

$$x_1 = \sqrt{\frac{k_B T}{\zeta}} \tag{4.25}$$

for any given temperature T. However it would be useful to write x_1 in terms of the Doppler width of the transitions. So using

$$w = 2\nu_0\sqrt{\frac{2k_BT\ln 2}{mc^2}} \tag{4.26}$$

where w is the Doppler width (in hertz), gives

$$x_1 = \frac{wc}{2\nu_0}\sqrt{\frac{m}{\zeta 2\ln 2}} \tag{4.27}$$

However, we do not want the cloud size to fall below the size of the laser beam. Putting $a = -b$, this can be roughly modelled by setting $x_2 = \sqrt{x_1^2 + a^2}$ where x_2 is the spatial extent of the cloud and replacing x_1 with x_2 in equation 4.21. So the fraction of time the ion spends in the beam in one dimension, Ξ, is

$$\Xi = \frac{-2ax_2^2 + \frac{1}{3} - 2a^3}{\frac{4}{3}x_2^3} \tag{4.28}$$

Finally, this factor must be squared since the beam spot is two dimensional (the third dimension, along the beam, produces a stripe of fluorescence so this analysis is not relevant). The cloud is considered to have roughly equal size in the two dimensions perpendicular to the laser beam.

4.1.6 The change in Doppler width R

Throughout the simulation, the temperature of the ions changes. This corresponds to a change in the Doppler width of each transition. The simulation is divided up into discrete time steps of length δt. At each time step new values for the Doppler width will be calculated, which will then change the Voigt profiles of the transitions. Hence the interaction strengths between the transitions and the lasers, and the populations in each level, will change for the next time step. It will be assumed that after each time step δt, the population is at equilibrium at a new temperature.

Consider the energy change involved in one interaction between laser 1 and transition C. L_1 is the detuning of laser 1 from the zero field transition and Δf is the shift of the transition due to the Zeeman effect. The energy imparted to the ion on absorbing and spontaneously emitting a laser photon once from laser 1 and line C is $h(L_1 - \Delta f)$. Also, the number of interactions per ion from laser 1 on line C in time δt is $n_1/N \times C_1 \times \Xi^2$. So the average energy transfer in time δt per ion from laser 1 on line C is

$$\frac{n_1}{N} C_1 \times (L_1 - \Delta f) h \times \Xi^2 \tag{4.29}$$

Now using the formula for the Doppler width w to find the change in width in time δt

$$w = 2\nu_0 \sqrt{\frac{2 \ln 2 E}{mc^2}} \tag{4.30}$$

So

$$w^2 = 4\nu_0^2 \frac{2 \ln 2 E}{mc^2} \tag{4.31}$$

and taking differentials

$$2w\delta w = \frac{8\nu_0^2 \ln 2}{mc^2} \delta E \tag{4.32}$$

Assuming the change in Doppler width is small compared to the total width for each time step gives

$$\delta w_{C_1} = \frac{4 \ln 2 \nu_0^2}{mc^2} \frac{1}{w} \frac{n_1}{N} C_1 \times (L_1 - \Delta f) h \times \Xi^2 \tag{4.33}$$

where δw_{C_1} is the change in width in Hz due to laser 1 and transition C.

Summing the contributions from all transitions and lasers gives the total change in width, due to laser cooling, δw to be

$$\begin{aligned} \delta w \;=\; & \frac{4 \ln 2 \nu_0^2}{mc^2} \frac{h}{w} \left[\frac{n_1}{N} C_1 \times (L_1 - \Delta f) + \frac{n_1}{N} C_2 \times (L_2 - \Delta f) \right. \\ & + \frac{n_1}{N} D_1 \times (L_1 - 2\Delta f) + \frac{n_1}{N} D_2 \times (L_2 - 2\Delta f) \\ & + \frac{n_2}{N} A_1 \times (L_1 + 2\Delta f) + \frac{n_2}{N} A_2 \times (L_2 + 2\Delta f) \\ & \left. + \frac{n_2}{N} B_1 \times (L_1 + \Delta f) + \frac{n_2}{N} B_2 \times (L_2 + \Delta f) \right] \times \Xi^2 \end{aligned} \tag{4.34}$$

The change in width used in the program is denoted by R and has two additional heating factors H_1 and H_2. H_1 is an arbitrary heating due to, say, background gas in the trap and is usually set to zero during simulations. H_2 is due to ‘random walk’ heating and will be further discussed below.

$$R = \delta w + H_1 + H_2 \tag{4.35}$$

The Doppler width is recalculated at each time step t in the simulation according to

$$w_t = \frac{w_{t-1} + R_t + w_{\min} + |w_{t-1} + R_t - w_{\min}|}{2} \tag{4.36}$$

and is therefore always above some minimum positive width $w_{\min}$. A minimum Doppler width is used since this approximates the situation of a real ion in a Penning trap. In a real trap, the magnetron motion is not cooled with the same efficiency as the modified cyclotron and axial frequencies. The magnetron motion tends to cool down until the ion cloud radius is of similar size to the cooling laser. This could lead to a residual temperature of the ions based on the magnetron motion. For a beam (and hence magnetron) radius of 25μm and a magnetron frequency of 40kHz, this leads to an ion speed of around 6.3ms^{-1}. Ions moving at this speed will suffer a Doppler shift of about 20MHz on the 397nm transition ($\Delta\nu = (2\sqrt{\ln 2})\nu_0 v/c$). It is necessary, in order to correctly calculate the Voigt profiles, that the strips used in the Simpson's rule approximation are small enough that several fall within $w_{\min}$.

Since it is the fluorescence level that is monitored in real ion trap experiments, it is desirable to include the fluorescence in this model. The fluorescence (F) is simply the number of photons scattered per second, i.e. the number of transitions per second.

$$F = \left[\frac{n_1}{N}(C_1 + C_2 + D_1 + D_2) + \frac{n_2}{N}(A_1 + A_2 + B_1 + B_2)\right] \times \Xi^2 \div \delta t \tag{4.37}$$

4.1.7 Random walk heating H_2

During laser cooling, photons are absorbed from a laser beam by an ion. Since the laser beam is red detuned, the photon does not have enough energy alone to promote an electron from the ground state to an excited state, so an amount of the ion's kinetic energy is converted to promote the electron. The ion is therefore cooled. Some time later, the excited ion will spontaneously emit a photon as the electron returns to the ground state. This photon will travel in a random direction and, since momentum is conserved, will give the ion a kick of magnitude $\hbar k$ in a random direction. Over N such random kicks, the ion will perform a random walk in momentum space. It is well established that the average distance R which the ion will be from its starting point after N steps of average length $\hbar k$ is

$$R = \hbar k\sqrt{N} \tag{4.38}$$

where $\hbar k/2m$ is the recoil energy.

Consider an ion in momentum space with initial momentum $m\mathbf{v_i}$. It undergoes a displacement ($\mathbf{R}$) of magnitude R in a random direction and so ends with final momentum $m\mathbf{v_f}$

$$m\mathbf{v}_f = m\mathbf{v_i} + \mathbf{R} \tag{4.39}$$

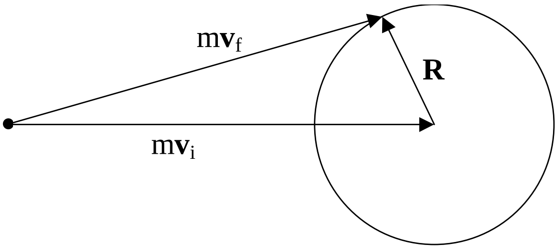

Figure 4.8: Random walk heating

Aligning the axis $\mathbf{i}$ along the initial momentum $m\mathbf{v_i}$ gives

$$\begin{aligned} m\mathbf{v_i} &= mv_i\mathbf{i} && (4.40)\\ \text{and}\qquad \mathbf{R} &= R\sin\theta\cos\phi\mathbf{i} + R\sin\theta\sin\phi\mathbf{j} + R\cos\theta\mathbf{k} && (4.41)\end{aligned}$$

where θ and ϕ are defined in the usual way for spherical polar coordinates. Then

$$m\mathbf{v}_f = (mv_i + R\sin\theta\cos\phi)\mathbf{i} + R\sin\theta\sin\phi\mathbf{j} + R\cos\theta\mathbf{k} \tag{4.42}$$

Writing the change in energy as ΔE

$$\begin{aligned} \Delta E &= E_f - E_i && (4.43)\\ &= 1/2m\mathbf{v}_f^2 - 1/2m\mathbf{v}_i^2 && (4.44)\\ &= \frac{1}{2m}\Big[(mv_i + R\sin\theta\cos\phi)^2 + (R\sin\theta\sin\phi)^2 + (R\cos\theta)^2\Big] \\ &\quad -1/2mv_i^2 && (4.45)\\ &= v_iR\sin\theta\cos\phi + \frac{R^2}{2m} && (4.46)\end{aligned}$$

The direction of $\mathbf{R}$ is random so the average value of ΔE must be found over the surface of a unit sphere

$$< \Delta E >= \frac{1}{4\pi} \iint \Delta E dA \tag{4.47}$$

where $dA = \sin\theta d\phi d\theta$ in spherical polars. Therefore

$$< \Delta E >= \frac{R^2}{2m} \tag{4.48}$$

Since N is simply the number of photons scattered in time δt then

$$N = F\delta t \tag{4.49}$$

Converting energy changes to Doppler width changes as in equation 4.32 and putting in the ^{40}Ca$^+$ mass and the wavelength of the scattered photons as 397nm gives

$$\delta w = 5.49 \times 10^9 \frac{\delta t}{w} F = H_2 \tag{4.50}$$

H_2 was negligible compared to R in all these simulations. The Doppler limited temperature for free ions was much less than the minimum allowed for the trapped ions due to the residual temperature of the ions caused by the magnetron motion.

4.2 Results

There are a number of user-definable parameters in the model. I will give the typical values used for the standard simulations described below. If the parameters differ from these values for a given simulation, then it is noted in that section.

The Zeeman splitting between transitions is taken to be 9GHz. This corresponds to a 1T magnetic field in the case of Ca$^+$. This is the maximum value which our magnet can deliver and is a reasonable field to use in a Penning trap with a conventional magnet.

The natural (Lorentzian) linewidth is set to 20MHz which is the case for the $S_{1/2} - P_{1/2}$ transition in Ca$^+$. The minimum Gaussian width is also set to 20MHz, which is consistent with the temperature deduced from the magnetron motion and the minimum cloud size. If this were set lower, then it would require the number of strips used in the Simpson's rule approximation to be correspondingly larger. This in turn places extra demands on the processor running the simulation without providing any new physical insights.

The laser intensity is set to 2500Wm^{-2}, which is comparable to the saturation power of 2750Wm^{-2}.[3] This roughly corresponds to a laser power of 25μW focussed to a spot of width 50μm. Again, these are reasonable values for our apparatus (to within an order of magnitude).

The laser spot size is taken to have a radius of 25μm for the purposes of calculating the cloud size. The axial frequency is taken as 175kHz, a typical value for our trap. For an initial Doppler (Gaussian) width of 5GHz, this gives an initial cloud size of about 1mm and a temperature of $\sim$ 3000K (0.26eV). These values are not unreasonable for trapped ions that have not been cooled. Complications of laser cooling in the Penning trap due to the ion dynamics are ignored and the laser beam is taken to pass through the centre of the trap.

The factors H_1, 'fluorescence factor' and 'cooling factor' are arbitrary. H_1 represents a heating factor in Hz due to non-laser factors and was set to zero. 'fluorescence factor' sets a scaling on the fluorescence level and should be set to one. This factor can be used to adjust for the solid angle and quantum efficiency on the photomultiplier tube if so desired. 'Cooling factor' alters the strength of the cooling and should be set to unity for realistic operation, but can be set higher in order to increase the speed of cooling.

The polarisation angle is fixed to 5°. This allows the lasers to predominantly drive transitions B and C ($\Delta m_J = 0$). The laser detuning is altered from simulation to simulation but a reasonable situation is to strongly drive transitions B (laser 1) and C (laser 2) by detuning to the red side of each transition by $\sim$ 0.05GHz. In the program, laser detunings are set from the position of the zero field transition.

The remaining parameters are a function of the model itself, rather than the experimental apparatus. The time step is set so that the simulation encompasses a time comparable to how long the ions take to cool. The number of steps was initially set to around 100 but was increased as the need arose. The number of strips was set such that at least five strips would fall within the narrowest of the lines (either the Gaussian of the Lorentzian). The integration limits were set so as to include all major contributions to the overlap integral used for the convolution.

If the limits of integration are set symmetrically about the Lorentzian portion of the integral, at say ±50×HWHM of the Lorentzian, and the cen-

---

[3] The saturation power is taken to be the power at which the probability of spontaneous and stimulated decay is equal. The formula used to calculate the saturation power S is $S = 4\pi^2\hbar c\Gamma/\lambda^3$ [97], where Γ is $22 \times 2\pi$MHz.

tre of the Gaussian (i.e. the laser detuning from the line centre) is within the limits of integration, then the convolution integral should give realistic values. If the computer speed were higher, then one could integrate over the Gaussian. Since the Gaussian may be much broader than the Lorentzian, this would require many more strips to be used in the calculation. However, since the Gaussian wings fall rapidly to zero above a few linewidths, this would ultimately resolve all problems in setting the integration limits.

4.2.1 Four-level cooling using two constant lasers

As has been described above, although this simulation is flexible and completely general, the parameters have been tied to our experiment. If both lasers are detuned by 0.05GHz from their respective transitions, then the ions do indeed cool. It is notable that, for these initially hot ions, the cooling rate is initially very slow. This is because the lasers are very close to resonance where the Gaussian is flat and low (since the Gaussian is normalised and broad). If the lasers were moved further from resonance, then the initial cooling rate would be higher. This is due to the greater energy difference between the transition centre and the laser. A single scattering event will therefore take more kinetic energy from the ion, but the number of events will remain similar due to the flatness of the distribution. As the ions cool, the Gaussian width decreases and so its magnitude increases. This increases the cooling rate. When the Doppler width reaches the minimum value, the cooling stops. If the ion initially cools, then for both lasers on resonance or red detuned, the ion will reach the minimum allowed temperature.

Figure 4.9 shows the evolution through time of the Gaussian width for several different detunings L1 of laser 1 from line B. Laser 2 is on resonance with line C. The closer that laser 1 is set to resonance, the longer it takes to reach the minimum temperature. Several such simulations were done for different detunings of laser 2 (L2=0, -0.05, -0.1 GHz) and in each case the time taken to cool to the minimum width was found to be roughly related to $1/(a \times (L1) + b)$. Fitting this rectangular hyperbola to the cooling times for different L1s gave a goodness of fit parameter $r > 0.999$ in all cases.

As the ions are cooled, the interaction with the lasers gets larger and so the fluorescence increases. An example of how the fluorescence changes over time is given in Figure 4.10. The fluorescence increases slowly at first. As the cooling rate accelerates and the Gaussian width falls to its minimum value, the fluorescence rapidly increases to a plateau. The final fluorescence level is plotted in Figure 4.11 for different laser 1 detunings L1. The maximum fluorescence increases rapidly as the detuning reaches zero. Temperature can be derived from the Doppler width and is plotted for L1=-0.1GHz, L2=0

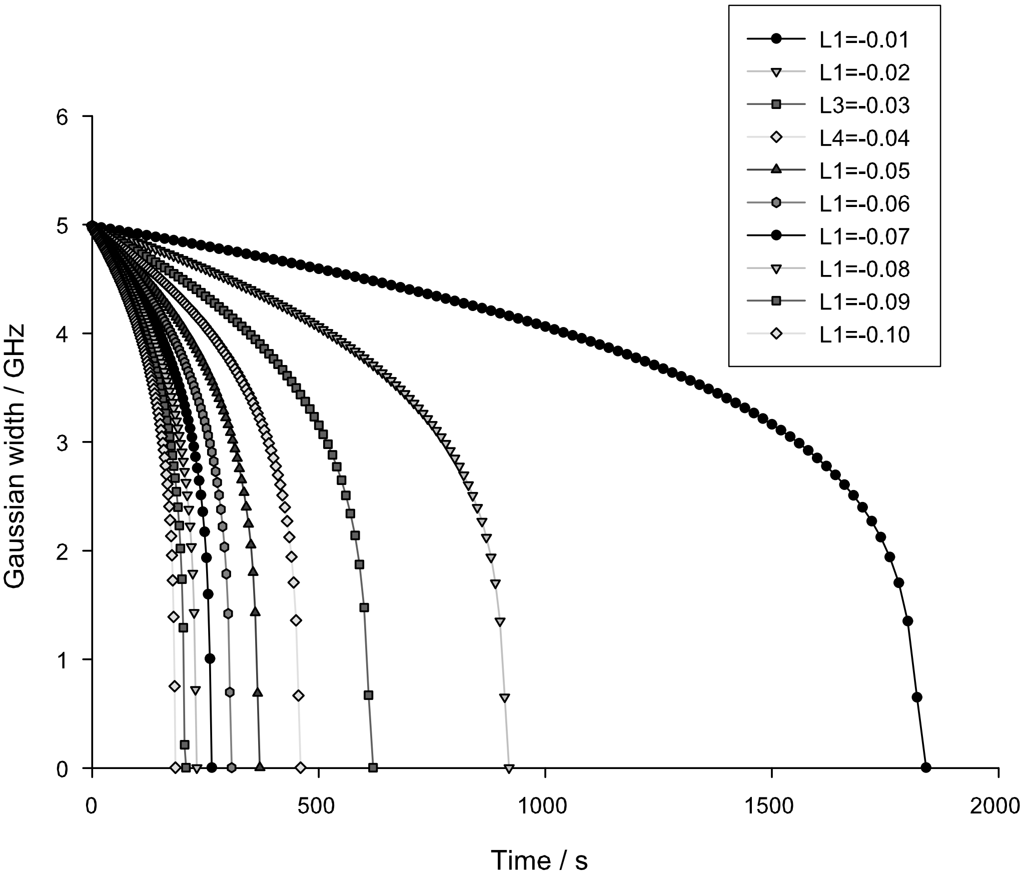

Figure 4.9: Gaussian width as a function of time for two constant lasers. L1 is the detuning of laser 1 from the transition.

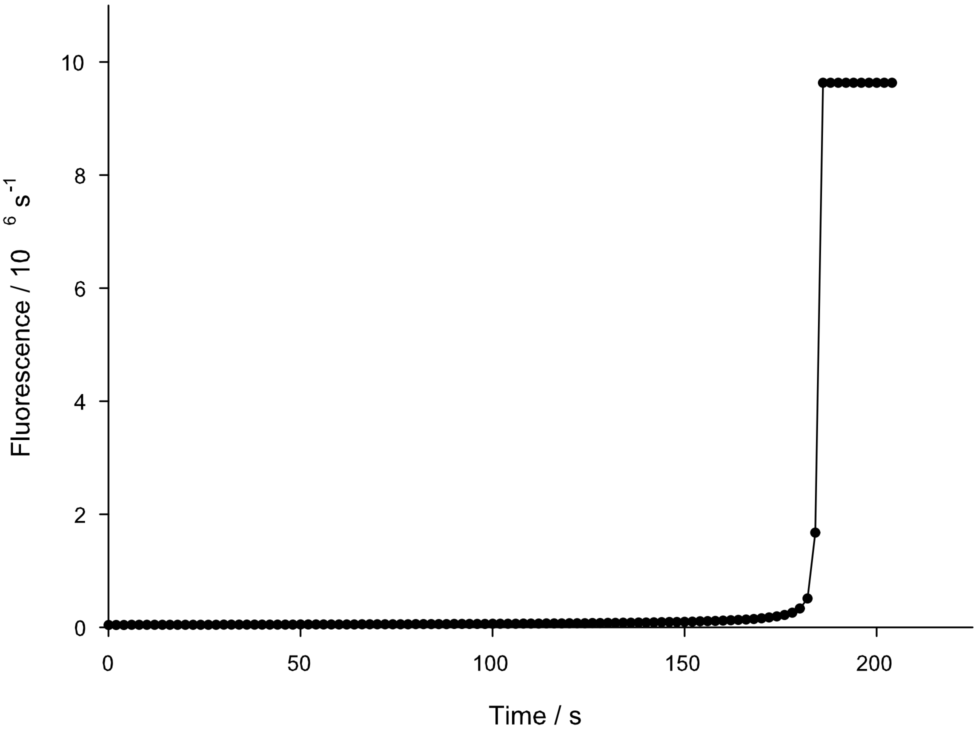

Figure 4.10: Fluorescence per ion as the ion cools

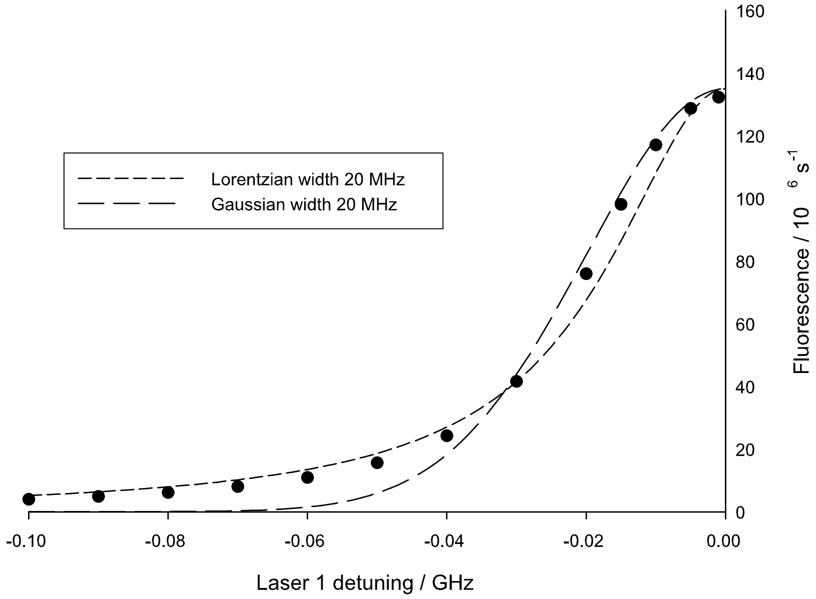

Figure 4.11: Maximum fluorescence per ion for different laser 1 detunings with L2 on resonance. Close to resonance, this closely matches a Gaussian of linewidth 20MHz, but further from resonance the profile drops off less rapidly due to optical pumping effects.

(Figure 4.12). In these situations, the proportions of the population in levels

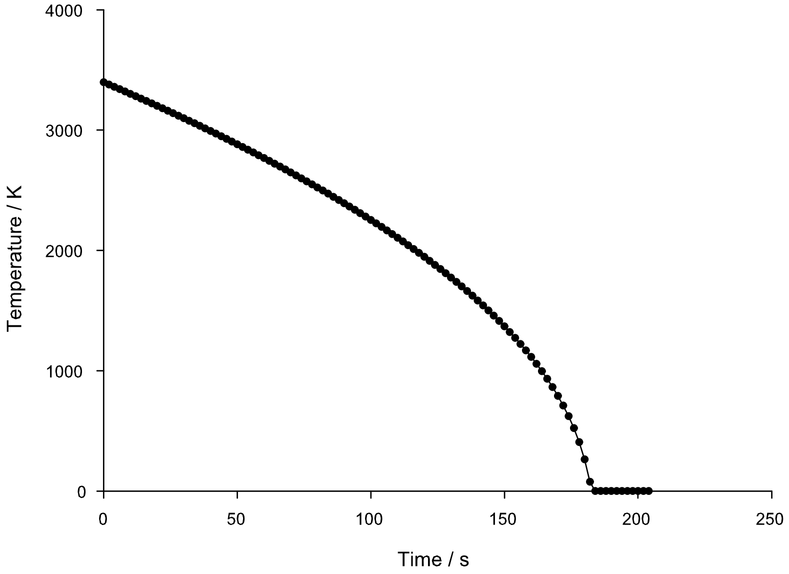

Figure 4.12: Temperature as a function of time

1 and 2 are close to 0.5 until the ions cool significantly. If the Gaussian is broad, then both lasers (being close to line centre) will have almost equal interactions. However as the ions are cooled and the Gaussian width becomes comparable to the detunings, then there is difference between the two lasers and so the population is optically pumped into the level being addressed the weakest (Figure 4.13).

4.2.2 Four-level cooling using one constant and one scanning laser

The program has been written so that laser 1 can be scanned in frequency throughout a simulation. The initial detuning is set at say -3GHz from line centre. The scan range can then be set to 3GHz for instance and the scan time set to 30s. To observe the whole scan, the time step will need to be set such that there are enough steps in the simulation to last 30s. In our experiments, it is common to keep one laser fixed in frequency whilst the other scans over about 3GHz in 1s. It is therefore useful to study these simulations. In this section, two parameters will be varied. These are the scan time and the detuning of the constant laser.

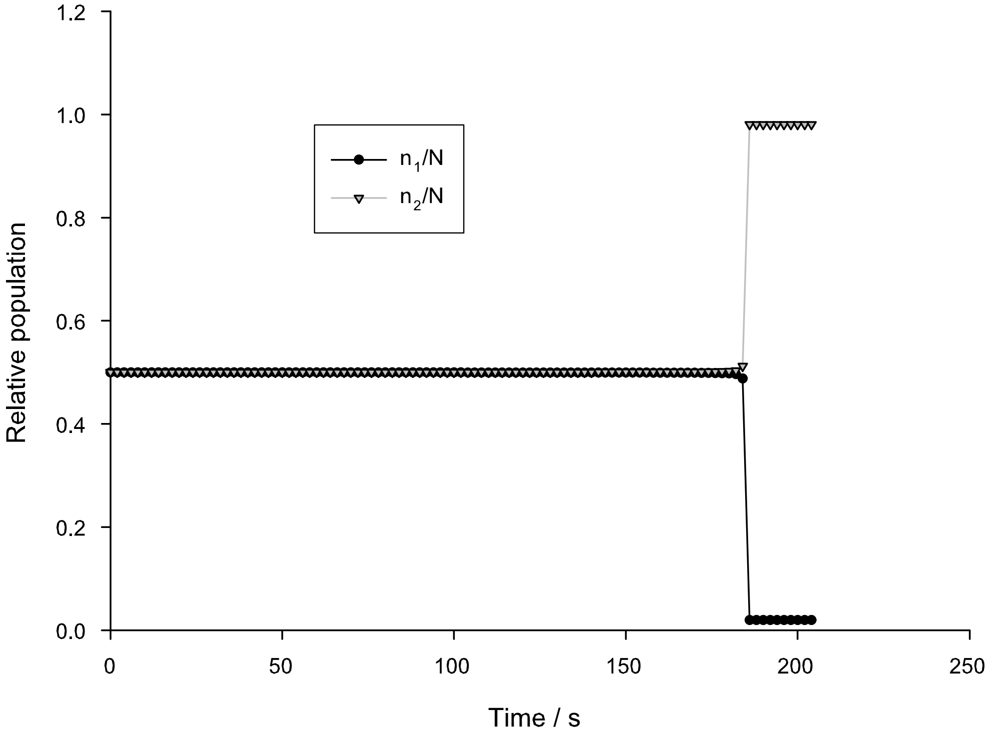

Figure 4.13: Proportion of population in levels 1 and 2

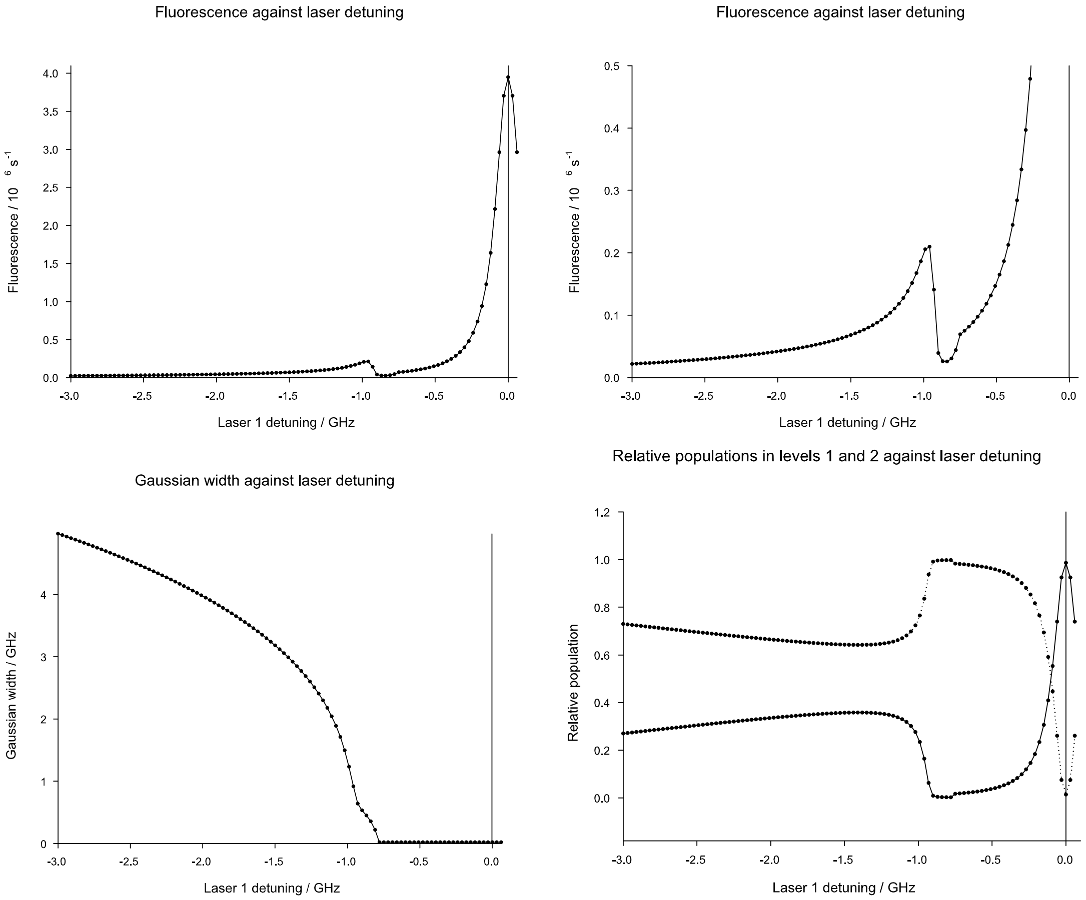

Figure 4.14: Results for L1 scanning over 3GHz in 20s with L2 fixed at a detuning of -0.1GHz. The top right frame is an expanded scale version of the top left frame.

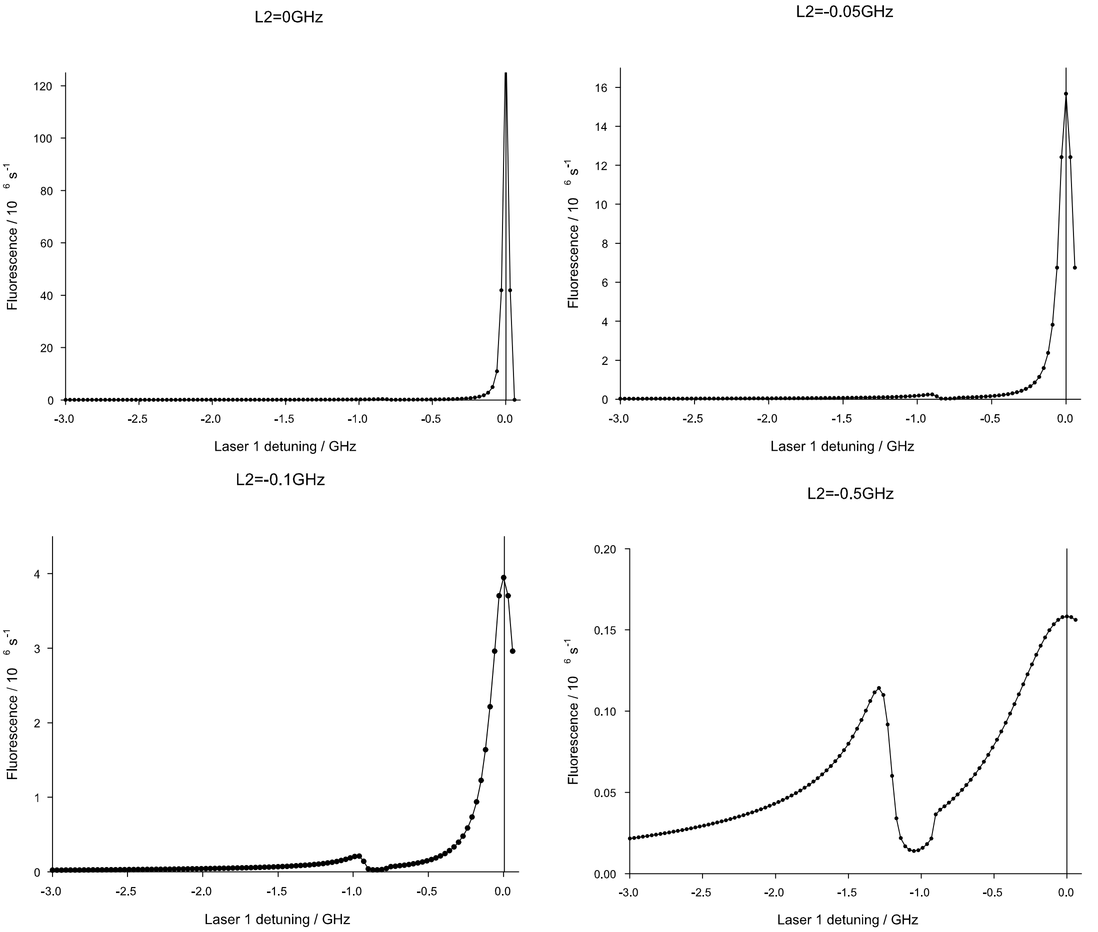

Figure 4.15: Ion fluorescence for various detunings of L2. L1 scanned over 3GHz in 20s. The bottom left frame has the same parameters as Figure 4.14.

First consider different detunings of laser 2, with a laser 1 scan of 3GHz over 20s. See Figure 4.14. This time is larger than in experiments but is used to show the behaviour of the system. Note that the cooling is an order of magnitude quicker than in the non-scanning case due to the large initial detuning. Initially, the Gaussian width is larger than the laser detuning. The ions cool slowly, but at a rate that reduces the Doppler width faster than the laser scans into resonance. The cooling rate will therefore increase initially. The populations in levels 1 and 2 will converge towards 0.5 as the detuning of laser 1 from line B converges on the detuning of laser 2 from line C. As the ions cool further, the Doppler width becomes comparable to the detuning of laser 1. The cooling rate then increases rapidly since the interaction with the lasers increases rapidly. This causes a sharp increase in the fluorescence (the 'cooling spike') and the Doppler width rapidly becomes smaller than the detuning of laser 1. The cooling rate therefore slows again and the fluorescence decreases. Since the Doppler width is now narrow, the non-scanning laser 2, which is closer to resonance, will interact much more strongly than laser 1. This drives the population almost exclusively into level 1 and so cooling is very slow again. The ions then continue to be cooled slowly, but gradually increase their cooling rate on a new cooling curve until reaching the minimum Gaussian width. When the ion reaches the minimum Gaussian width, this will coincide with a sharp discontinuity in the rate of change of fluorescence with laser detuning.

As the laser moves closer to resonance, it will reach a point where its detuning is equal to that of laser 2. Here the population will rapidly swap from primarily being in level 1 to being in level 2. In general, there will be a large increase in the fluorescence as laser 1 scans over the now narrow line profile. See Figure 4.14.

Performing scans with different (constant) detunings of laser 2 will alter the shape of the fluorescence curve. This is illustrated in Figure 4.15. For larger detunings, the cooling spike happens earlier in the scan since the initial cooling is more effective. The cooling spike also becomes broader for increased laser 2 detuning and is more pronounced compared to the maximum of fluorescence when laser 1 has scanned in to line centre. Although both the cooling spike and the fluorescence peak decrease in magnitude as laser 2's detuning is increased from 0 to -1GHz, the cooling spike only drops by a factor of four whilst the fluorescence peak drops by a factor of 3500. The fluorescence peak also gets considerably broader, with the HWHM being comparable to the detuning of laser 2.

Performing scans of differing speeds (same scan frequency width and laser 2 detuning) also alters the shape of the cooling curve. See Figure 4.16. Slower scans will tend to decrease the amplitude of the cooling spike and also to broaden it. Providing that the cooling spike occurs, it will happen at roughly constant times into the scan (about 13s in our case). The fluorescence peak will also be a constant height and width providing that the ion does reach its minimum temperature. If the scan is too quick, then the ion does not reach its minimum temperature, there is no cooling spike and the fluorescence curve is broad and low. In such a case, the scan is too quick for the Doppler linewidth to catch up with the laser detuning and produce the sudden cooling behaviour. In experiments, this situation would correspond to several scans of the laser with virtually no increase in fluorescence whilst the ion is cooled bit by bit. When the ions finally reach a cold enough temperature, the fluorescence will suddenly increase dramatically and it will seem as if the ions have suddenly appeared. This kind of behaviour is observed in our experiments.

4.2.3 Two-level cooling with one laser

The model of a four-level ion can be reduced to a two level system. Here only one laser is needed to complete a closed loop cooling cycle since the ion must always decay to the same ground state. This is similar to the level structure of Mg^+ and Be^+ which may be used with a single σ transition cooling laser, giving an effective two-level system. These are the only other ions previously used in laser cooling experiments in Penning traps. To reduce the simulation to two levels, the population of level 1 is set to zero ($n_1/N = 0$) and that of level 2 fixed at one ($n_2/N = 1$). The intensity of laser 2 is also set to zero. To increase the speed of the simulation, C_1, C_2, D_1, D_2 were also set to zero.

Scanning the laser produced similar results to the four-level case. However, the cooling spike is broader and much less pronounced than in the four-level case. This is due to the lack of optical pumping effects. Various scan speeds were tried and the results were in agreement with the four-level case, but with more efficient cooling (since emptying level 1 of population was not necessary). If the scan was too quick then cooling would not occur.

4.2.4 Two-level cooling with two lasers

A finite (and controllable) final ion temperature may be achieved by employing two lasers. One laser should be positioned to the blue side of a transition, the other to the red. We used the two-level system to perform these simulations. It is notable that the four-level system will not permit the use of similar techniques due to optical pumping.

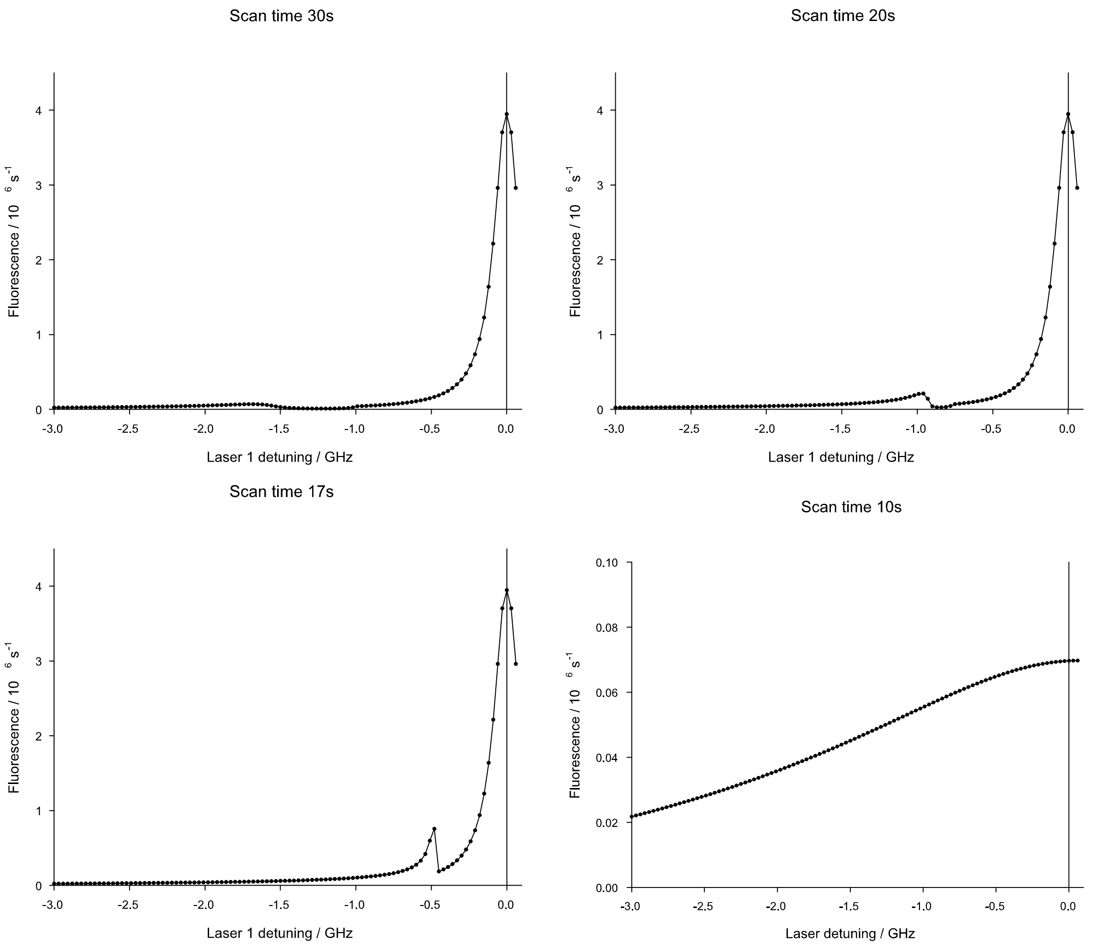

Figure 4.16: Ion fluorescence for various speeds of scan of L1 over 3GHz with L2 fixed at a detuning of -0.1GHz. Note the different vertical scale for the 10s scan. The top right frame is for the same parameters as Figure 4.14

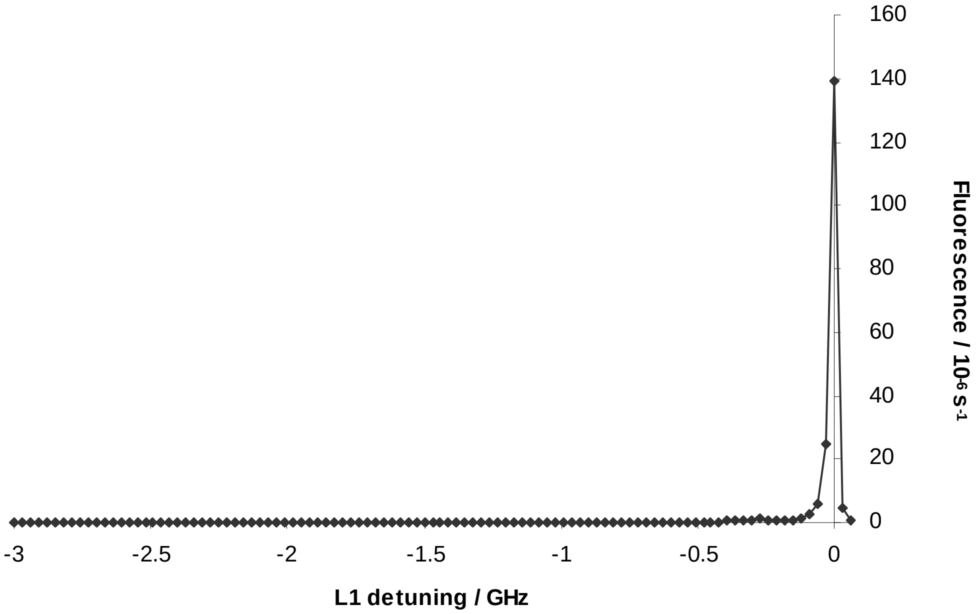

Figure 4.17: Ion fluorescence in the two level system for a laser scan of 3GHz in 11s. Scans of shorter duration would not display proper cooling. Note the relatively small size of the cooling spike in the absence of optical pumping.

The lasers must be positioned correctly to 'trap' the Doppler width at some finite level. To achieve this, the laser detuned to the red side of the transition should be further from resonance than the laser detuned to the blue. Consider a broad Doppler width. This will be roughly flat close to line centre and so the two lasers will interact equally with the ion. However, the red detuned laser will cause more kinetic energy to be lost per interaction than the blue detuned laser will add per interaction and so the ion will cool. When the Doppler width is narrow, the blue detuned laser (being closer to line centre) will have a stronger interaction with the ion and the ion temperature will therefore increase. Between these two extremes, the ion should reach an equilibrium where the heating is balanced by the cooling and the Doppler width is held in place.

Analytical approximation to finding the balance temperature

The Voigt profile does not lend itself to an analytical analysis of the above situation. However, if the transition is taken to have either a Gaussian or Lorentzian lineshape, then it is possible to obtain an analytical solution for the width of the transition at equilibrium.

Consider a Gaussian profile. At the equilibrium width, the cooling from laser 1 must balance the heating from laser 2. So

$$\begin{aligned} \rho_1 G(L_1) L_1 &= -\rho_2 G(L_2) L_2 \qquad (4.51) \\ -\frac{\rho_1 L_1}{\rho_2 L_2} &= \frac{G(L_2)}{G(L_1)} \qquad (4.52) \end{aligned}$$

Substituting for the Gaussian, $G(x) = \exp(-\ln 2 \times (2x/w)^2)$ gives the width, w

$$w = \sqrt{\frac{4 \ln 2 \times (L_1^2 - L_2^2)}{\ln(-\rho_1 L_1/\rho_2 L_2)}} \qquad (4.53)$$

To achieve a balanced temperature in this system, two conditions must be met by the lasers. The first ensures that there is cooling for a sufficiently large linewidth and the second ensures that there is heating for a sufficiently small linewidth. For a large linewidth, the lineshape appears flat at the frequencies of the two lasers. So if $|\rho_1 L_1| > |\rho_2 L_2|$, then the ions will cool for large enough widths. For a narrow linewidth, it is necessary that $|L_1| > |L_2|$. The intensities of the lasers can be ignored in this case since the exponential fall off of the Gaussian will always override any difference in intensities for widths that are narrow enough.

The equilibrium width (equation 4.53) is shown plotted against the detuning of laser 1 in Figure 4.18 for different intensity ratios, $I = \rho_1/\rho_2$. There are two separate regimes depending on whether I is greater than or less than unity. For $I > 1$, the value of L_1 is limited by the second condition (for heating). For values of $|L_1| < 0.1$GHz, there cannot be sufficient heating to balance the cooling effect of laser 1 and there is therefore no equilibrium temperature. As L_1 approaches 0.1GHz the width falls to zero. Note that this is independent of the relative powers of the lasers, providing $I > 1$.

The second regime is for $I < 1$. Here the value of L_1 is limited by the first condition and for $|L_1| < |L_2\rho_2/\rho_1|$ there is not sufficient cooling to stabilise the width at any value. As this condition on L_1 is approached, the width therefore tends towards infinity. The width also tends towards infinity for large detunings of laser 1 since the width would then have to be very wide to provide significant cooling to balance the heating. Given these two extremes there must be a minimum width that is achieved somewhere in between[4].

A similar approach can be used assuming that the lineshape is Lorentzian, $L(x) = 1/(1 + (2x/w)^2)$ (Figure 4.19). This yields

$$w = \sqrt{\frac{4\rho_2 L_1 L_2 (L_1 + \rho_1 L_2/\rho_2)}{\rho_1 L_1 + \rho_2 L_2}} \tag{4.54}$$

Note that for $I < 1$ the behaviour is very similar to the Gaussian case and the minimum value of L_1 is again limited by $|L_1| > \rho_2 L_2/\rho_1$.[5] Inspection of the formula for w will reveal that there is now a new condition for the case where $I > 1$. This condition is $|L_1| > L_2\rho_1/\rho_2$. Hence, the detuning where there is just sufficient heating to balance the cooling is dependent on the ratio of the laser powers. This difference between the Lorentzian and Gaussian cases is due to the exponential fall-off in the wings of the Gaussian.

Simulation approach to finding the balance temperature

This section describes the use of the computer simulation to study the actual behaviour when the Voigt line profile is assumed.

To obtain realistic results for the final temperature, the time step size δt must be set to a small enough value. Above this value, bifurcations and

---

[4] It is not possible to get a simple, analytical solution for the detuning of laser 1 at the minimum width.

[5] The detuning of laser 1 at the minimum width can be solved for the Lorentzian case. The minimum is at $L_1 = L_2(-1 \pm \sqrt{1 - I^2})/I^2$.

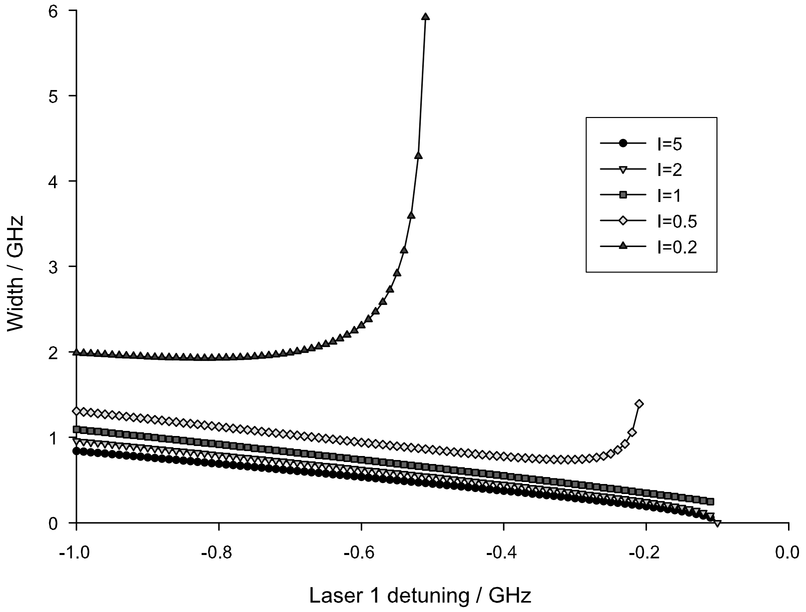

Figure 4.18: Analytical solutions for the balance temperature assuming a Gaussian lineshape. Laser 2 has fixed detuning of +0.1GHz in all plots.

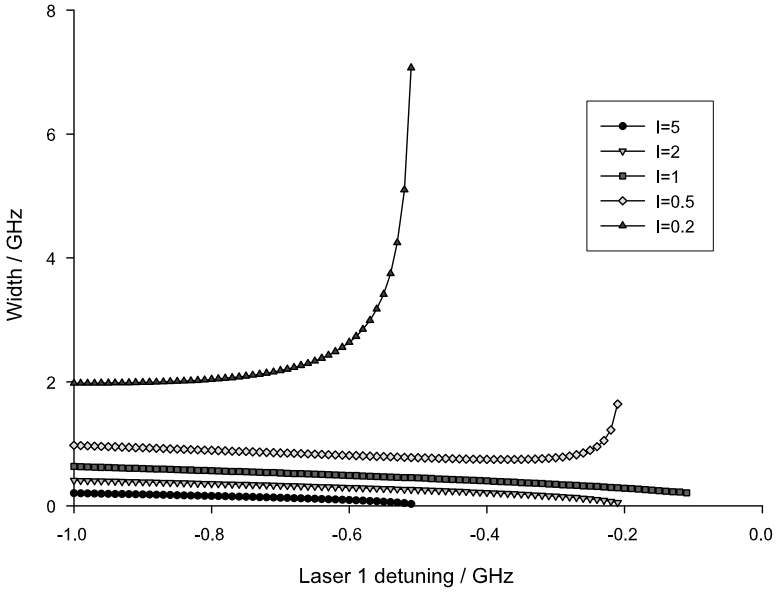

Figure 4.19: Analytical solutions for the balance temperature assuming a Lorentzian lineshape. Laser 2 has fixed detuning of +0.1GHz in all plots.

period doublings were found to occur. These are obviously not physical, but a manifestation of the discrete time intervals used in the model. To ensure realistic behaviour, these were investigated using a detuning of 0.3GHz to the red for laser 1 and 0.1GHz to the blue for laser 2. The laser intensities were set such that laser 1 was 2500Wm^{-2} and laser 2 was 5000Wm^{-2}. A time step of below 0.02s did indeed allow convergence to a single finite temperature of around 30K. Increasing the time step to 0.025s produced an oscillation between two temperature levels 20K apart. Further increases led to 4, 8, then 16 levels and eventually to a near homogeneous band at $\delta t = 0.032s$. At $\delta t = 0.0345s$ however, order returned with 3 stable levels which bifurcated into 6 as δt was further increased. Care was taken to ensure that the time step was low enough to ensure sensible behaviour in all that follows.

Care should also be taken with the laser intensities. If the cooling is too quick as the ion is cooled down, then the Doppler width may hit its minimum value and then bounce up to a hot temperature. The ion will then cool rapidly again, perpetuating the cycle. Care must be again be taken to ensure reasonable behaviour. Changing the laser detunings and powers alters the final temperature as expected.

By scanning the red detuned laser up to resonance, as one would in an experiment, the equilibrium temperature can be plotted for different detunings. Several such plots were made for different ratios of the laser intensities. Laser 2 was detuned to the blue by 0.1GHz in all the plots. Consider the plot in which both lasers had intensities of 2500Wm^{-2}. The time step was set to 0.001s and 1000 steps were used. An initial width of 1.1GHz was used (which was close to equilibrium at a laser 1 detuning of 1 GHz) and laser 1 was scanned over 1GHz in 1s (Figure 4.20). To show that the time step was not affecting the results, another scan was simulated using $\delta t = 0.0005$s and 2000 steps (total time 1s). Also a scan over 1GHz in 2s (4000 steps) was taken to show that the ions were in equilibrium. These gave identical results up to the point where the magnitudes of the detunings of the two lasers were equal. At a detuning of laser 1 by 0.1GHz, the ions are heated indefinitely and are no longer in equilibrium. The start of the scans show that the Doppler width comes into equilibrium from its initial value.

The plots show more similarity to the Gaussian than the Lorentzian case. Note that for $I > 1$, the minimum detuning of laser 1 which allows a balanced temperature is nearly independent of I. This should be expected since the width of the Gaussian may dominate the width of the Lorentzian. Even at the minimum Gaussian width, the two widths are equal.

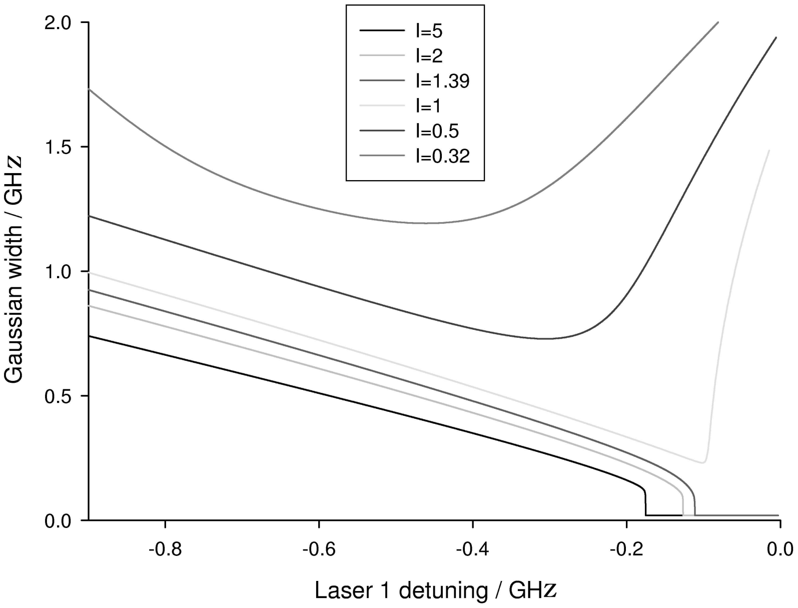

Figure 4.20: Gaussian width at balance for various values of the ratio of laser intensities I. L_2=0.1GHz in all cases. For $I < 1$, only values of $|L_1| > L_2 I$ have a finite equilibrium width. Points to the right hand side of the minimum may not be in equilibrium.

4.3 Summary

In summary, I have presented a rate equation model for simulating the laser cooling of a four-level ion using two lasers. This has incorporated the Voigt profiles of the ions as well as many parameters from our experiments. This has effectively produced a model of cooling Ca^+ in a Penning trap. Both the case of constant and scanning lasers has been considered. The system has also been used to simulate two level laser cooling using a single laser, which has been achieved experimentally by many groups in the past. Finally, a way of producing finite and controllable temperatures was described using a two-level system and two lasers.

Further work to improve the program may include saturation on the transitions for higher laser powers. It may also include inserting the $D_{3/2}$ and $D_{5/2}$ levels of Ca^+, although this will drastically increase the computer power required. The dynamics of the ions in a Penning trap may be modelled and the associated changes to laser cooling incorporated. The inclusion of space charge effects and patch potentials may also produce new insights.

Chapter 5

Apparatus

One of the major goals of this project was to trap and laser cool Ca^+ ions in a Penning trap. Only two species of ions (Mg^+ and Be^+) had previously been laser cooled in Penning traps. Calcium, however, has a different electronic level structure (see Figure 5.1) to both of these ions and so requires a more complicated suite of lasers to effectively laser cool it. Ca^+ has been laser cooled in an rf trap [91] [92].

The absence of a strong magnetic field in the rf trap means that there is no Zeeman splitting of the levels and so laser cooling is much simpler. Wavelength references are also much more readily achievable for transitions in Ca^+ without the magnetic field. Indeed, spectroscopy on the ion itself allowed the correct frequencies to be found. This is much more difficult if the spectroscopic source were to be kept in a magnetic field of 1T. For these reasons, we first trapped and cooled Ca^+ in a rf trap. This acted as a stepping stone to test parts of the laser system with the ions and to develop procedures to set the laser frequencies to the required values.

For laser cooling in a Penning trap, two lasers around 397nm must be used to stop the electron becoming shelved in one of the long-lived $S_{1/2}(m_J = \pm 1/2)$ states. Several repumping lasers at 866nm must also be used to empty the metastable $D_{3/2}$. In contrast, laser cooling in the rf trap only requires two lasers: one at 397nm to cool the ion and a repumper at 866nm.

To find the correct wavelengths to cool in a Paul trap, the blue (397nm) laser was initially set to within 2GHz of the Ca^+ $S_{1/2}$-$P_{1/2}$ transition using a wavemeter. It could then be set to within $\sim$ 100MHz using absorption spectroscopy in a hollow cathode lamp. After setting the laser using the wavemeter, the frequency of the laser was close enough to the desired value to see signal from the Doppler broadened transition in the hollow cathode lamp. The 397nm laser was then scanned over a 3.6GHz range from the red side of the transition into resonance using a piezoelectric transducer on the

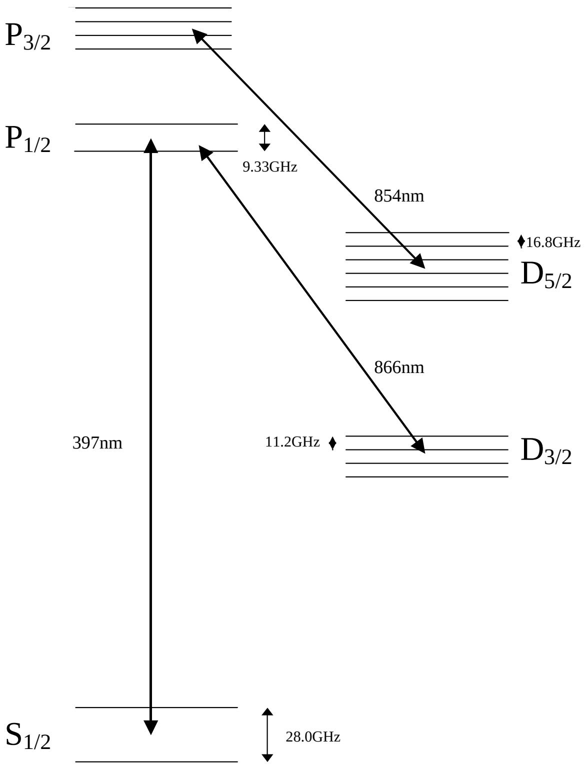

Figure 5.1: The level structure of Ca^+ in a magnetic field

extended cavity mirror. The 866nm laser was set to within 400MHz using the wavemeter.

5.1 The wavemeter

The wavemeter is a Burleigh model WA 20, which is rated to read wavelengths down to 400nm. It effectively works as a scanning Michelson interferometer with one moving mount carrying a corner cube reflector on each side. This causes the path lengths in each arm to vary in tandem (Figure 5.2). Changing the path lengths causes a series of fringes to be formed on the photodetector as the mount is moved back and forth. The electronics within the wavemeter then counts the number of fringes that pass over the photodetector as the arm lengths are changed. This is compared to the number of fringes which pass for an internal reference (HeNe) laser, which also follows a path round the Michelson. From these measurements the wavelength of the input light can be derived.

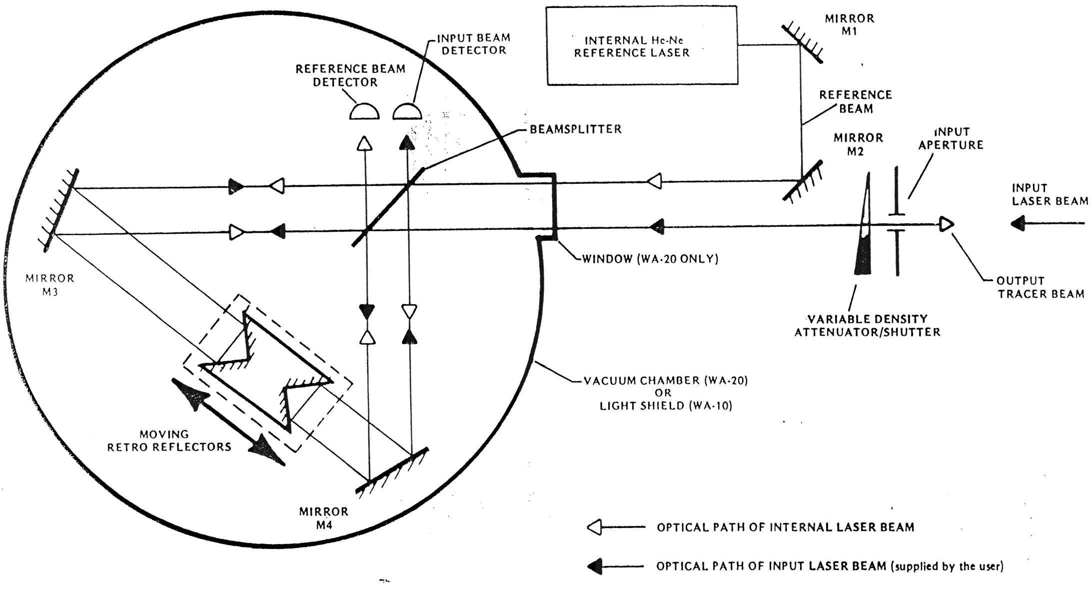

Figure 5.2: Wavemeter schematic, from the manual.

Unfortunately, the specification of the wavemeter down to 400nm was optimistic for light of around 3mW power. It is thought that this was partly due to the poor reflectivity of the mirrors at these low wavelengths. However, the fringe counting electronics did include a circuit to amplify the fringe signal. The input to the counting electronics (after amplification) can be viewed on an oscilloscope through a port on the rear of the wavemeter. If the wavemeter is to read properly, then this signal must be greater than 1V peak-to-peak. The amplification circuit is an op-amp in a negative feedback configuration (Figure 5.3), where

$$\left|\frac{V_0}{V_i}\right| = \frac{R_2}{R_1}\frac{1}{1+\omega^2(C_2^2R_2^2)} \tag{5.1}$$

R_2, R_1 are resistors
ω is the frequency of the fringes
C_2 is a capacitor
and the time constant is $\omega_0 = 1/C_2R_2$.

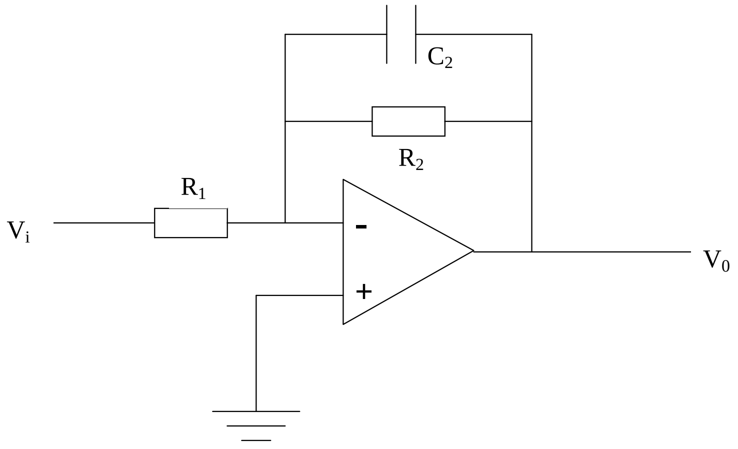

Figure 5.3: Amplification circuit to amplify the fringe signal.

The gain can therefore be increased by increasing R_2 and decreasing C_2. Initial values were R_2 = 75kΩ, C_2 = 5pF. A large gain could be achieved by using a large value for R_2 and zero for capacitance. This put the op-amp into a feedback loop due to its slow response time giving oscillations. The op-amp was therefore replaced by a faster model (LM 6364 instead of LM 318) and with R_2 = 680kΩ and C_2 = 0F. This increased the gain of the photodiode amplifier and allowed the wavelength of the 397nm laser light to be measured. The photodetector was also changed, but this did not lead to any significant improvements and so the original photodetector was replaced.

The wavemeter reads wavelength in nm to 3dp, but there is an offset to the true value which changes with wavelength. This was measured at several wavelengths using laser beams with known wavelengths (for instance, a

780nm diode locked to one of the rubidium lines using Doppler free saturation spectroscopy). It was found that the off-set could be as large as 0.006nm at long wavelengths. The reason for this offset is not known.

Monitoring the fringes output by the photodetector on an oscilloscope was found to yield useful information about the mode quality of the laser beam as well as how well the laser beam is aligned into the wavemeter. For better calibration of the wavemeter at precisely the frequencies we wished to use, a home-made hollow cathode lamp was used.

5.2 The hollow cathode lamp

Using a hollow cathode lamp to do spectroscopy on Ca^+ ions gives an absolute reference for the lasers with the exact same electronic transitions that are used in the rf trap. The hollow cathode lamp provides a plasma of Ca^+ ions in addition to Ca, Ca^{2+} etc. Absorption of the laser light will then show when the laser is on resonance with an electronic transition. The hollow cathode lamp itself is basically a vacuum tube evacuated to a pressure of 10^{-2}mbar of air and then filled with neon or argon gas to $\sim$ 1mbar. The exact operating pressure was too high to be read accurately on the Pirani gauge attached to the apparatus. A high voltage was applied to the gas leading to a discharge. The negative glow region of the discharge resides within the hollow cathode itself and, in the case of argon, glows blue (bright orange with neon). The purpose of the noble gas is two-fold: to sputter calcium from the walls of the hollow cathode; and to ionise the sputtered calcium. It is generally believed by spectroscopists [93] that argon may be better for sputtering and neon for ionising. It is also usual to use mixtures of these gases to achieve the optimal performance. If two gases are used concurrently, then the pressure of each gas may drastically affect the size of the signal and may need to be carefully controlled. However, for our uses it was found that the signal was quite insensitive to the pressure of the gas and that either of the gases alone would provide adequate signal.

The hollow cathode itself is a 30mm long nickel tube of internal diameter 9mm. It is held at a large negative potential with respect to the casing of the hollow cathode lamp, which is grounded. The tube is held onto the high voltage feed through pin by a collar of tantalum foil which is clamped into the bottom of the pin (Figure 5.4).

The calcium itself is cut into small pieces using a razor blade and a hammer. These are placed into the hollow cathode tube and the lamp is then fired for a couple of hours. The lamp runs with a voltage of 3.5kV and a current of between 85 and 100mA. This caused the calcium to be sputtered

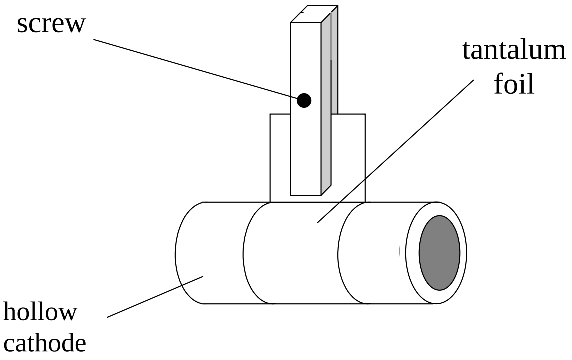

Figure 5.4: Hollow cathode and collar held onto the high voltage pin.

round the inside of the hollow cathode, where it forms a thin layer. Once the hollow cathode is coated, the lumps of calcium can then be removed. The hollow cathode lamp can then be run for a number of months before the calcium needs to be replenished.

The power supply used for driving the hollow cathode lamp was designed for use with an ion pump (VPS 60 Ion Pump Supply). The maximum current that can be drawn is 100mA. Since we were operating near this limit, using the supply internal resistance as ballast resistor, the current driver could not provide a constant current, but had a modulation at 100Hz. This was clearly visible on a photodiode output monitoring the intensity of light from the hollow cathode lamp with the oscilloscope set to trigger from the 50Hz mains line.

When a laser beam is sent through the hollow cathode and onto the photodiode, the laser light is much more intense than that from the hollow cathode lamp alone. By removing the DC offset part of the photodiode signal due to the laser, the characteristic 100Hz pattern of the hollow cathode can readily be seen (Figure 5.5). When the light intensity from the hollow cathode is largest, the hollow cathode is ‘firing’ and calcium ions are being produced. When light resonant with the $S_{1/2}$ - $P_{1/2}$ transition at 397nm is passed through the hollow cathode, some of it is absorbed by the Ca^+ ions. As the laser is brought into resonance, the peaks of the photodiode signal (where the lamp is producing Ca^+) become troughs. This is due to the more intense laser light dominating the signal. When the lamp is firing, some of the resonant laser light is absorbed by the Ca^+ ions, but when the lamp is in the off phase of its cycle, the laser light passes straight through the hollow cathode (Figure 5.6). Figure 5.5 and Figure 5.6 have very different vertical scales. The small structure in the troughs of Figure 5.6 corresponds

Figure 5.5: Light emitted from the hollow cathode lamp with no laser beam present. The frequency of the modulation is 100Hz and the peak-to-peak voltage is 50mV.

to the peaks in Figure 5.5. When compared to commercial hollow cathode lamps, this homemade lamp is found to give a much bigger signal. The advantage of building this lamp from sturdy metal vacuum components is that a large current can be used to form the discharge. Commercial lamps use about 1mA (100 times less current) and are hermetically sealed, so that the calcium source cannot be replenished at will. Building this spectroscopic source, was not only novel, but also represented a significant advance on commercially available equipment.

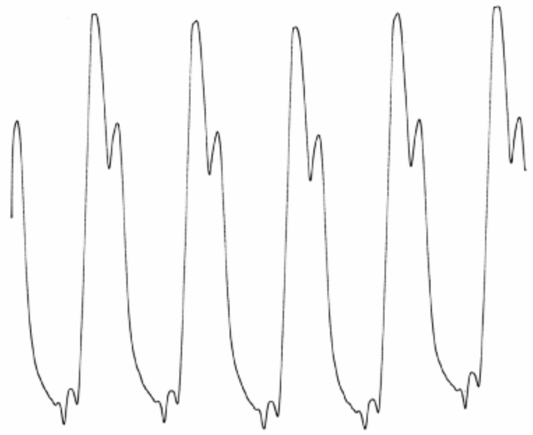

Figure 5.6: AC part of the light signal from the hollow cathode with the laser beam present. The troughs correspond to the hollow cathode lamp firing and hence producing Ca^+ ions which absorb some of the laser light. The peak-to-peak voltage is approximately 200mV.

By finding the maximum peak-to-peak signal, the blue laser can be set to within approximately 100MHz of the resonant frequency of the transition. A plot of the Doppler broadened line profile of the Ca^+ $S_{1/2}$ - $P_{1/2}$ transition was obtained by plotting the peak-to-peak voltage of the signal as the laser frequency was varied (Figure 5.7).

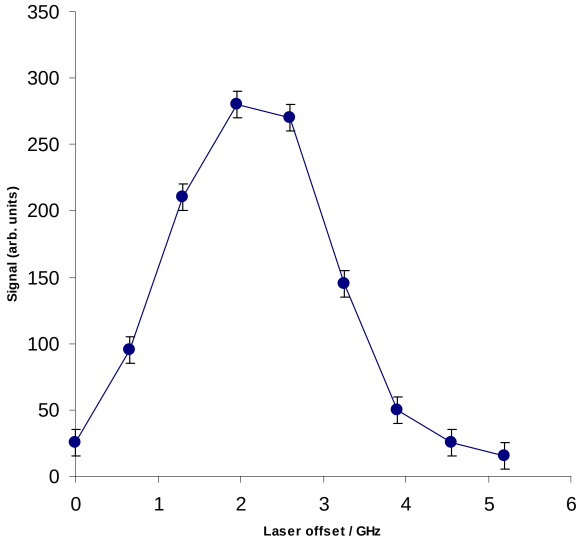

Figure 5.7: Doppler broadened $S_{1/2}$ - $P_{1/2}$ transition as measured using the hollow cathode lamp.

The hollow cathode lamp absorption could also be used for setting the infrared 866nm laser in a similar way. However, this repumper laser operates between two excited states (albeit that the lower one is metastable), so the corresponding absorption is much smaller and is therefore difficult to observe on a day-to-day basis. This signal was observed and used to calibrate the wavemeter at 866nm. The wavemeter could then be used to set this laser to within 400MHz of the required value. This wavelength is less critical than that of the blue laser and so this accuracy is good enough to further optimise the lasers using the fluorescence signal from a cloud of trapped ions. The frequencies and spatial positions of all the laser beams were optimised in this way by observing the florescence from the ions in the trap. This becomes more critical as the ions cool since there is less Doppler broadening on the cold ions and the cloud becomes physically small.

In using the hollow cathode lamp to find the 866nm wavelength, small signals from a photodetector were needed to be measured. Phase sensitive detection and differencing techniques were tried but neither gave significantly better results than the simple method above.

5.3 The blue cooling lasers

The blue laser is based on a Nichia laser diode. This has a centre wavelength of 397nm and a nominal output power of 5mW (1mW with feedback). The diode is housed in a commercial system in the Littrow configuration, with the Hänsch design [94]. Both the laser head and the control electronics were manufactured by TUI (now TOPTICA). A piezo electric transducer attached to the wavelength-selective grating allows the wavelength to be scanned.

The grating was aligned for feedback using a method similar to that used for the homemade infrared lasers (see below). The output was then put through a plane-plane Fabry-Perot cavity with a free spectral range of 6.3GHz. By scanning the laser over the fringes, it was possible to set the feed forward connecting the diode current and piezo voltage to give the minimum number of modehops over the tuning range. By central spot scanning in the far field, the amount the laser frequency changes as the piezo voltage is changed was measured at $0.60\mathrm{GHzV}^{-1}$.

A measurement was taken to give an estimate for the linewidth of the blue lasers. To achieve this, two blue laser systems were used. The laser light was mixed on a beam splitter and adjusted so that the two beams were colinear. A fast photodiode was used to measure the combined intensity of the coincident beams. When the frequencies of the two lasers were tuned close to each other (∼a few MHz) beats could be observed on a fast oscilloscope. Taking a Fourier transform of this beat signal gives the combined linewidth of the two lasers. The AC component of the photodiode signal is given in Figure 5.8 and the Fourier transform is given in Figure 5.9. The linewidth of the lasers is approximately 2MHz, which is a little greater than one might expect for an ir diode laser (∼ 200kHz). It is notable that there is considerable noise on the Fourier transform both at the peak and at the wings. It is believed that this is due to the beat signal being superimposed on a large background (a DC signal caused by the laser light). Although this DC level is subtracted from the signal, the large shot noise still remains. We were unable to remove this component from the measurement. Throughout these experiments, the lasers were not locked and had a drift of 200-300MHz per hour.

5.4 The infrared repumper lasers

This is a homemade system which includes an SDL 5411 G1 (or similar) diode with a centre wavelength at 852nm and a nominal power of 50mW. The rest of the system consists of a Littrow configuration, pseudo-external cavity and control electronics. The laser head was made in a manner similar

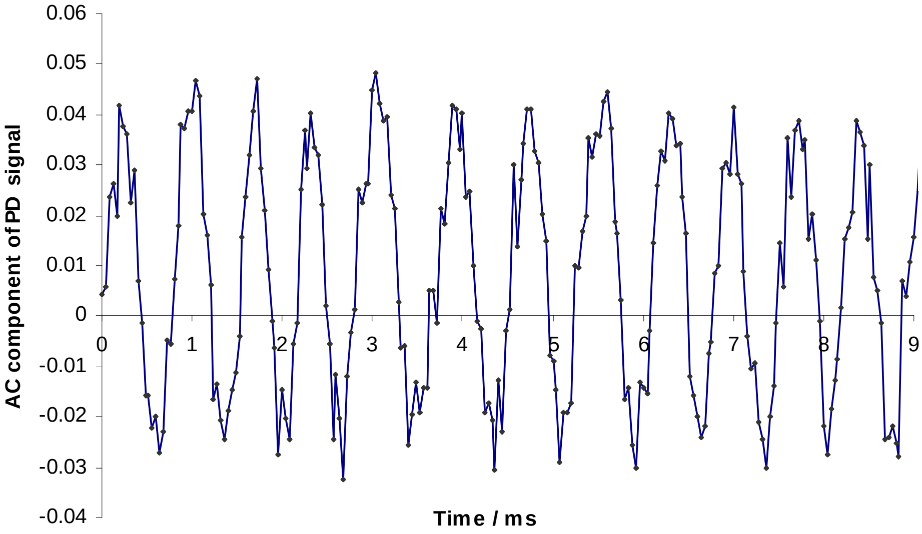

Figure 5.8: A portion of the beat signal of two blue laser diodes.

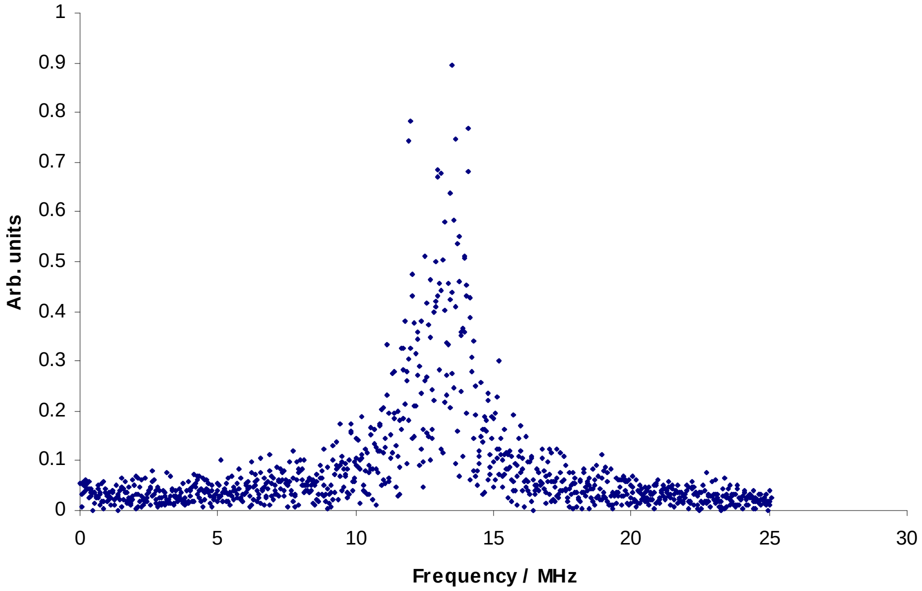

Figure 5.9: Fourier transform of the beat signal of the blue lasers.

to [95], see Figure 5.10. The back facet of the diode provides one end of the

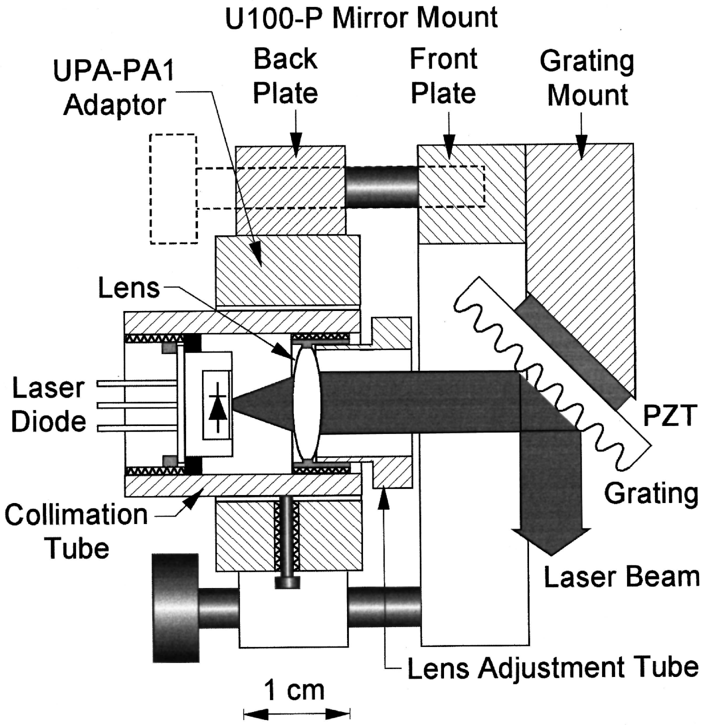

Figure 5.10: Schematic of the 866nm laser diode system. From [95]

laser cavity. The other is a gold coated diffraction grating. This is mounted at an angle of

$$\phi = \sin^{-1}\left(\frac{m\lambda}{2d}\right) \tag{5.2}$$

to provide feedback at a given wavelength λ from the m^{th} order of a grating with $1/d$ lines/m. This optical feedback of light in the laser cavity narrows the linewidth of the laser radiation and allows the wavelength to be tuned by altering ϕ and thus the feedback wavelength. The head is temperature stabilised using a Peltier thermo-electric heat pump. A piezo electric transducer is used to alter the grating position to fine tune the laser wavelength.

The current driver electronics and feedback circuit to stabilise the temperature are built around an ITC 100 board from Laser 2000. This board acts as a constant current source for the laser diode of about 90mA depending on precisely which model of laser diode is used. The current is stabilised to within 20μA on the board. The different models of laser diode require different temperature settings in conjunction with a certain driver current and diffraction grating angle. If the required temperature is close to room temperature, this can be achieved with the Peltier heat pump alone. However, for high temperatures ($\sim 40^\circ$C) a 24W heating resistor is attached to the laser head close to the mirror mount and can be used to help the Peltier stabilise the temperature at higher values.

Using a combination of heating, current tuning and grating tuning, the laser wavelength can be pulled from its centre at 852nm up to 866nm (or 854nm) which is needed to repump the $\mathrm{D}_{3/2}$ ($\mathrm{D}_{5/2}$) levels.

To set up the infrared lasers, a CCD camera or IR viewing card is needed to observe the light. With the laser running without feedback, two spots should be seen at the output of the laser. One is the true beam, the other is a beam reflected from the front facet of the diode after being reflected at the grating. Aligning these beams on top of one another should bring the laser close to the correct position for feedback. The current should now be reduced until the laser is just below threshold. Using the mirror mount to alter the vertical position of the reflected spot should cause the laser to flash on at some point. This is the correct placement for feedback. The horizontal displacement (ϕ) can then be scanned to pull the wavelength in the required direction.

The laser will flash on and off at frequency intervals commensurate with the free spectral range of the Fabry-Perot cavity formed by the front and back faces of the diode. This and temperature tuning allows gross tuning of the wavelength. Fine tuning is achieved by setting the current to its operating value and either tuning the current (fine tuning) or the voltage on the piezo electric transducer (very fine tuning). Using the wavemeter will allow the frequency to be set to within 400MHz, although the piezo can be scanned in much smaller increments.

Diffraction gratings with different blaze angles back-reflect different amounts of radiation for feedback. Testing blazes designed for different wavelengths (500, 750, 1000nm) led us to the conclusion that blazing for 750nm (closest to our desired wavelength of 866nm) worked best. This is due to the relatively large feedback needed to pull the wavelength so far from the free running wavelength of the diode (852nm).

5.5 The trap

The trap electrode structure is similar to that required to produce a perfect quadrupole potential (Figure 5.11). It was manufactured before I joined the group. Future work will be done in a superconducting magnet, which requires a slightly different design to fit into the centre of the magnet. In our trap, however, the electrodes have a spherical cross-section rather than the ideal hyperboloids of revolution. This was for ease of machining. The radius of curvature of the ring is 4mm and that of the endcap is 10mm. This was chosen to best approximate the quadrupole potential [96]. There are three holes in the ring electrode. Two are diametrically opposed and in the horizontal plane. These allow the laser beams to pass through the trap. It is important that these entrance and exit holes are big enough to allow lasers to pass through without scattering off the edges, but small enough that the electric fields still approximate to the quadrupole ideal. The third, conical, hole, is perpendicular to a line joining the other two and allows fluorescence from the ions to pass vertically upwards into the detection apparatus. There is a notch cut into the ring electrode diametrically opposite this hole, so that the detection apparatus looks into a void. The ring has a diameter of 10mm and the endcap separation is 7mm. The whole arrangement is mounted on the central pin of an ultra-high vacuum electrical feedthrough.

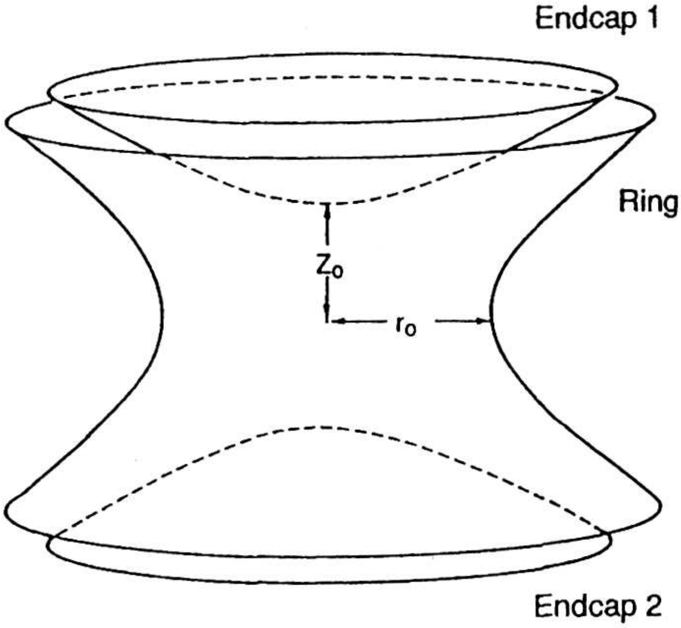

Figure 5.11: Schematic of trap electrodes. Note that in the actual experiments, the trap axis through the endcaps is horizontal.

Two ovens are held near the trap and point through the small gap between the ring and endcap electrodes. These serve to deliver a beam of calcium atoms into the trap. The ovens are constructed from tantalum tube 10mm long and 1mm in diameter. One end is clamped completely shut whilst the other is clamped shut apart from a pin hole to let a beam of atoms escape. The oven is spot welded onto a 0.25mm diameter tantalum wire. This serves as a support for the oven and also as a heating element when current is passed through it (Figure 5.12). Two filaments act as sources of electrons to ionise the calcium atoms. These are constructed from 0.25mm diameter tungsten wire and are placed behind the endcaps.

The whole trap is kept in ultra-high vacuum conditions after initial baking at 250°C and pumping on a turbo pump for five days. The vacuum is then maintained by an ion pump (Meca 2000) at 2×10^{-10}mbar. For more details see [96].

5.6 The imaging system

Two distinct methods of imaging were used. These were a photomultiplier tube and a CCD camera.

5.6.1 Photomultiplier tube

This imaging system is shown in Figure 5.13. A lens of focal length 38.1mm in the visible is mounted in the vacuum system above the trap. Originally this trap was constructed for UV wavelengths, where the focal length of the lens was 35mm. The lens is at a fixed position of 28.5mm above the centre of the trap, so that UV fluorescence would be nearly collimated. This value was chosen to minimise aberrations. Working at 397nm, the focal length of the lens is between the two values given above, but the collimation is still sufficient for good detection. Another lens is placed on an xyz-translation stage outside the ultra-high vacuum chamber. This lens has focal length 50.8mm (in the visible) and is used to focus the fluorescence onto a pin-hole below the photomultiplier tube.

An image of the ions at the trap centre is therefore formed on the pinhole. The pinhole has a diameter of approximately 1mm and is used to block as much background light as possible from hitting the photocathode of the photomultiplier tube, whilst still passing the fluorescence from the ions. This whole arrangement, from the top of the vacuum can to the photomultiplier tube is surrounded by a shield of black card and a dark cloth. This serves to provide further protection from stray light giving rise to background noise on the photomultiplier signal. The photomultiplier itself must be protected from magnetic fields. For this reason, the photomultiplier tube is elevated

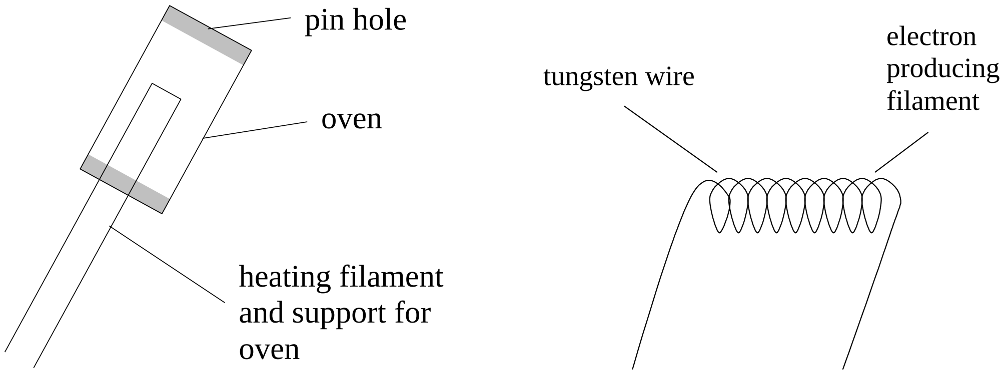

Figure 5.12: Diagram showing oven construction and filament to produce ionising electrons

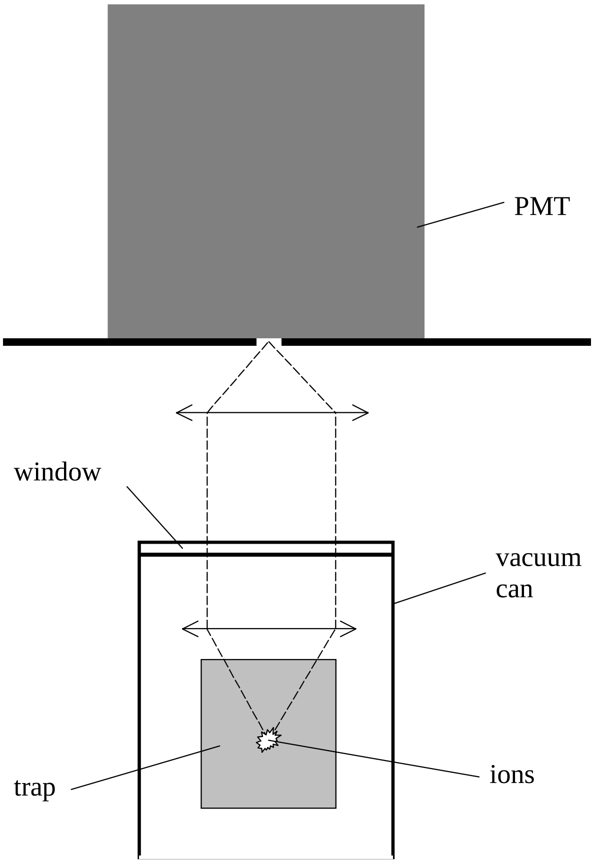

Figure 5.13: Imaging system for the photomultiplier tube

above the trap and is housed in a mu-metal shield.

Two optical filters are placed between the pin-hole and the photomultiplier tube. One is coloured glass (Comar 465GK25, BG3 glass) with good extinction over the whole visible spectrum down to 500nm and the other is an interference filter (Comar 400IL25) with a sharp cut off and a pass band of 10nm around a centre wavelength of 400nm. Together these filters cut out much of the scattered visible light ($\sim 100\%$) whilst passing a significant proportion of the fluorescence at 397nm (30%). The signal from the photomultiplier tube is passed to a multi-channel scalar (MCS) card in a computer. For display purposes, the level of fluorescence is displayed as counts per bin, where the length of each bin is chosen to be $\sim$2ms. Theoretically, the lens in the trap subtends a solid angle of 0.32steradians since the lens is 28mm from the trap centre and has a usable radius of 9mm ($\pi 9^2/28^2 = 0.32$steradians). Therefore the imaging system may collect a fraction $0.32/4\pi = 26 \times 10^{-3}$ of photons. At 397nm, the photomultiplier tube has a theoretical efficiency of 23% and so the overall efficiency (including the filters) of this apparatus should be $\sim 2 \times 10^{-3}$.

5.6.2 CCD camera

Whilst the photomultiplier tube is a very useful tool and is very sensitive to overall fluorescence, it gives no information on the size, shape and position of the cloud. This spatial information is completely lost. To gain spatial information, a CCD camera must be used. This camera will be used extensively for imaging ions in the next stage of the project. So far, it has only been used to take preliminary pictures of the trapped ions. It is an Andor ICCD-47-10 CCD camera, which has a CCD resolution of 1024×1024 pixels, with an image intensifier with a spatial resolution of 22μm. The image intensifier can act as a fast shutter to gate the camera.

The output of the CCD camera is displayed on a PC. The imaging system involves diverting the fluorescence away from the photomultiplier tube and into the CCD camera. This means that the two imaging systems cannot be used concurrently. The imaging schematic is shown in Figure 5.14.

Since the lens inside the vacuum chamber was designed initially to collect the greatest amount of fluorescence for the photomultiplier tube, without thought to resolution, this system is not optimal.

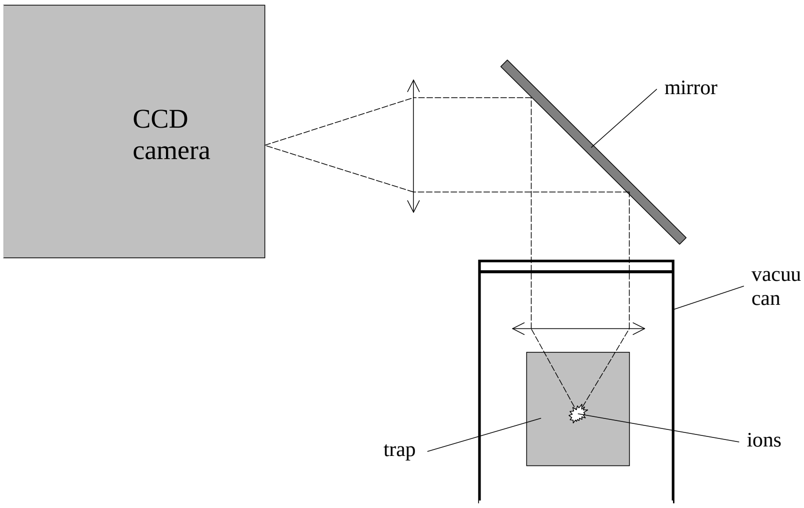

Figure 5.14: Imaging system for the CCD camera

Chapter 6

The Paul trap

This chapter encompasses the work done with the Paul trap. It describes the alignment of the lasers with the trap and the associated optics. It also describes the alignment of the detection system. The Paul trap was chosen as an initial stepping stone to trapping and laser cooling in a Penning trap. The absence of Zeeman splitting allows laser cooling to be achieved with only two lasers, which is much easier than the schemes needed to cool in a Penning trap. Ca^+ has been trapped and cooled in a Paul trap by other groups (Blatt in Innsbruck and Steane in Oxford), but until the beginning of this project the Imperial College group had only worked with Mg^+ and Be^+. Trapping of small clouds and single ions has been demonstrated and is presented at the end of the chapter.

6.1 Optical set up for the Paul trap

A schematic of the lasers and optics required to laser cool in a Paul trap is shown in Figure 6.1. Dielectrically coated mirrors (Comar MX189) are used to steer the blue (397nm) cooling laser round the optical table. The infrared (866nm and 854nm) beams are steered using standard gold-coated mirrors (Comar 25MX03). The two beams are mixed on a dichroic mirror (Comar 530BK25) which passes the infrared beams but reflects the blue.

The two beams are colinear as they pass through a lens of focal length 220mm, which focusses the beams into the trap. Whilst the blue light is focussed to a tight spot (50μm) at the trap centre, chromatic aberrations in the lens ensure that the infrared light bathes a larger area. Because of this, it is possible to move the 397nm beam position around the trap using the dichroic mirror without having to move the 866nm beam at the same time. Measurement of the spot size of the blue laser was carried out by K Koo

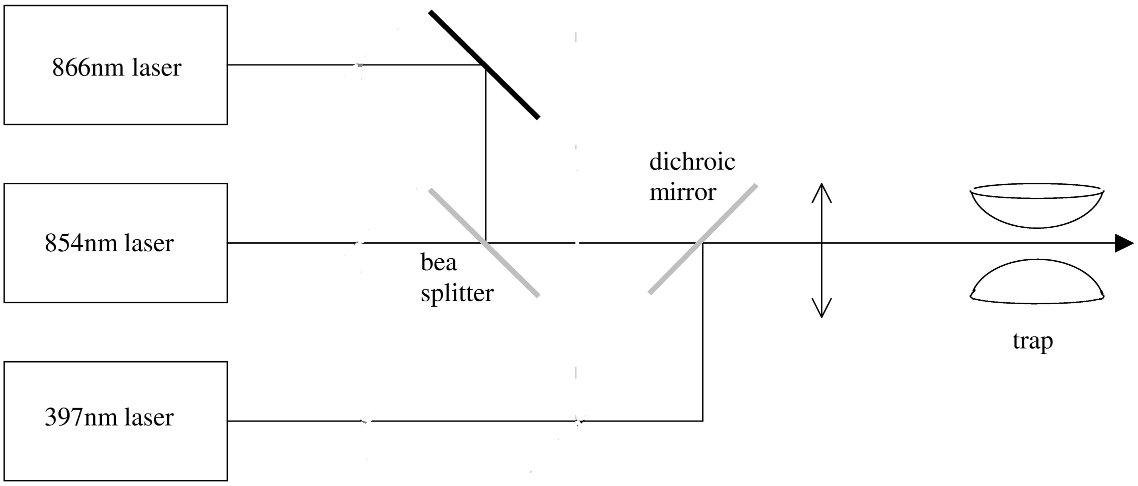

Figure 6.1: Schematic of the optical layout for the Paul trap

using a knife edge technique.

Flipper mirrors (New Focus 9891-M) are used to switch the blue beam from the trap to the diagnostic equipment (wavemeter, hollow cathode lamp as described earlier). This allows all the blue light to be used in the trap, but at the same time facilitates the use of the diagnostic equipment. The power in the infrared beams is plentiful, so a small amount of their power (5%) is picked off using mirrors coated for high reflectance in the UV (280nm) but transparent in the visible. The 866nm and 854nm lasers are mixed on another of these UV mirrors. This passes most of the 866nm light but reflects a small amount of the 854nm light into a colinear beam.

6.1.1 Procedure for aligning the lasers through the trap

As discussed in Section 5.5, the ring electrode of the trap contains two diametrically opposed holes for the lasers to enter and exit the trap. By looking through the trap it is possible to locate the position where the line through these holes intersects the front window of the vacuum chamber, the dichroic mirror and a screen placed behind the trap apparatus. It is then possible to position the blue beam (with the lens removed) such that some light passes through the trap. Since the eye is relatively insensitive at these short wavelengths, the screen is coated with a fluorescent ink which emits light at a more visible green wavelength when struck by the laser. Blocking the laser again and looking through the trap it is possible to locate the position which the beam should strike on the screen. This is most accurately accomplished by lowering a black card across the screen, noting when the view through the trap goes dark. This locates the height of the beam. A similar procedure will locate the horizontal position.

The beam would now be aligned reasonably through the centre of the trap. The addition of the lens, placed 22cm from the trap centre and coaxially with the beam, should focus the beam into the trap. It is important that the lens is in exactly the right position, so that the cooling laser is focussed at the trap centre. This also minimises the laser light scattered from the trap electrodes into the photomultiplier tube.

The lens should be finely adjusted to fulfill two criteria. One is that the beam cuts off sharply at the electrodes as it is scanned using the dichroic mirror. This implies that the light is tightly focussed at the trap. The second is that the scattered light should be at a minimum. This implies that the laser beam is passing cleanly through the trap. Once this is achieved, the infrared beam can be adjusted to be colinear with the blue beam (i.e. lie on top both before and after the trap). The beams should now overlap at the trap centre.

6.1.2 Aligning the imaging optics

The lens immediately above the trap (Figure 5.13) is not adjustable since it is fixed inside the vacuum chamber and kept under ultra high vacuum conditions. To align the second imaging lens it is first necessary to remove the photomultiplier and filters and fully open the iris serving as a pin hole. Shining an ordinary desk lamp through the laser input window (and removing other ambient light) will allow the user to see into the trap by looking through the iris. The conical hole in the ring electrode should be visible as a silver coloured ring. The lens should be positioned using an xyz translation stage so as to centre the image of the ring on the aperture. The image of the ring should be in the plane of the aperture, which can be achieved by looking for a vertical position of the lens at which there is no parallax between the image and the aperture.

This procedure is likely to leave the lens too close to the trap, since the image of the ring was formed using visible light, whereas the fluorescence of Ca^+ is at 397nm. Nevertheless, this procedure will bring the imaging system close enough to alignment to record some fluorescence from a cloud of trapped ions when the filters and photomultiplier tube are replaced. As a final adjustment, look for a point where the scattered background light is at a minimum using the photomultiplier and then maximise the signal from a cloud of trapped and laser cooled ions. If the image of the ions is well focussed at the aperture, then closing the iris and looking for a low background with large signal which cuts off sharply as the image is moved in the plane of the aperture will give the best alignment of the optics. In practice, several iterations of moving the imaging lens, the laser beam focussing lens and the dichroic mirror may be necessary to find the best possible positions.

6.2 Operating the Paul trap

To run the Paul trap, the endcap electrodes were grounded. The ring electrode was set at a DC offset potential of +6V and an rf drive voltage of 240V at a frequency of 1.83MHz was applied to it. This drive voltage was derived from a signal generator (HP 3325B) with an output of 29mV. This was fed to the input of an amplifier (ENI 325LA). At the output of this amplifier, the voltage was 14V. Finally, the output of this amplifier was fed to a homemade circuit which steps up the rf voltage to 240V using an air core transformer (which acts as a tuned circuit operated at resonance) and adds the DC offset voltage. The resonant frequency of the air core transformer was measured using a low capacitance, high voltage probe and found to be 1.83MHz. It was necessary to do this with the trap electrodes connected, since the capacitance of the trap affected the frequency of the resonance.

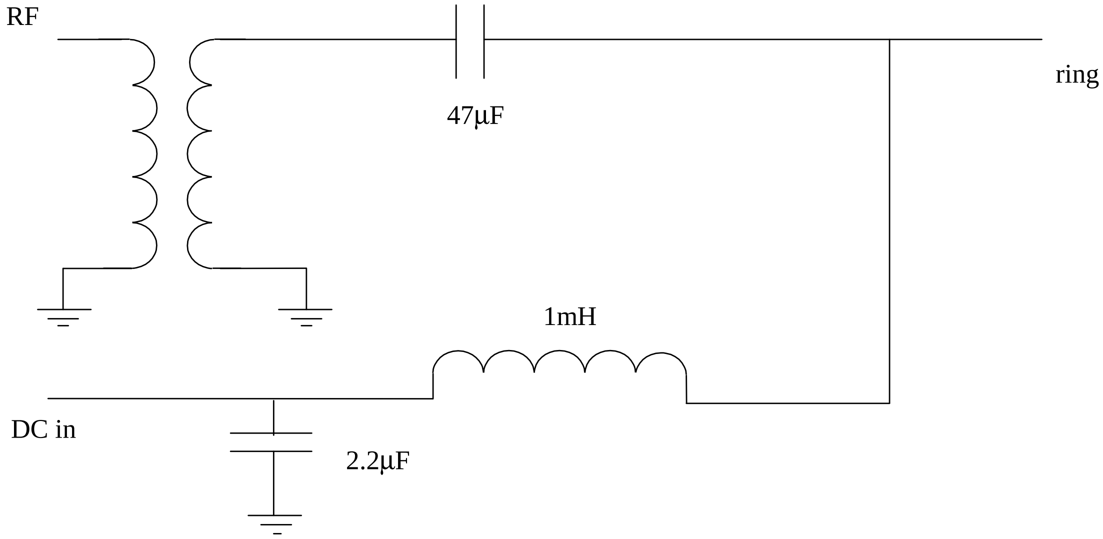

Figure 6.2: Step up transformer and circuit to apply high voltage rf to the trap. The inductor and capacitor are included to block the rf and dc signals respectively.

6.2.1 Electronic detection

It is possible to detect the presence of ions in a trap by purely electronic means. Electronic detection was initially used to check the efficacy of the Paul trap. Being the first time that Ca^+ had been trapped by the group, it was a necessary and useful test of our ability to trap Ca^+ in the Paul trap. The trap was loaded by passing a current of 2.00A through the wire connected to the oven. The oven would take 32s to heat to the required temperature to form an atomic beam through evaporation of calcium. The calcium beam passes through the trap. After the first 20s of heating of the oven, a current of 5A was passed through the filament situated behind one of the endcaps. The filament would take 10s to heat to the required temperature. At this temperature, the filament acts as an electron gun, emitting a stream of electrons. The electrons are guided along the magnetic field lines through the centre of the trap by applying a magnetic field of 0.1T through the endcaps of the trap. The filament was kept at a negative (bias) voltage of -12V relative to the centre of the trap, such that the electrons are accelerated away from the filament. In the trap, collisions between electrons and calcium atoms have sufficient energy to ionise the calcium atoms to Ca^+. By applying the appropriate electromagnetic fields, Ca^+ ions are confined to this region of space and are trapped.

These ions have characteristic motional frequencies associated with the trap parameters (Section 3.1.2). By driving the motions at these frequencies, it is possible to detect the ions by electronic means. An LCR circuit was constructed between the endcaps of the trap for this purpose.

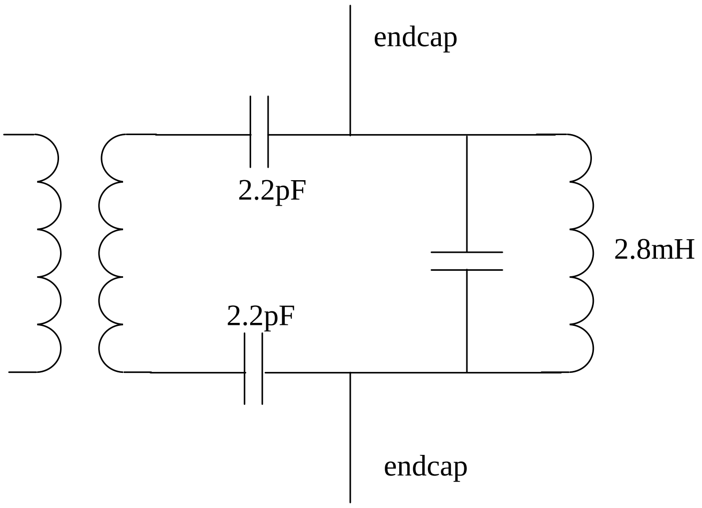

Figure 6.3: High Q LCR tuned circuit used in electronic detection.

When the resonant frequency of this tuned circuit matches the motional frequency of the ions in the trap (in this case the axial frequency, $\omega_z = 1/LC$), energy is coupled into the ions' motion. The loss of energy in the circuit can be detected as an reduction in voltage across the transformer in this circuit. Coupling energy into the ions' motion will usually result in the ions being heated out of the trap unless the applied driving voltage is small. For this reason, the oven and filament are fired continuously to constantly replace the ejected ions.

The DC voltage on the ring was scanned upwards whilst the driving frequency was kept constant. As the DC voltage brought the axial frequency into resonance with the drive frequency, there was a detectable drop in voltage across the resistor. Whilst this was small, it was readily observable and sufficient to convince us that Ca^+ was indeed trapped. If a better signal to noise ratio were required, then the use of a lock-in amplifier at the driving frequency will improve the signal. It may be noted that the parameters for resonance may be used to derive a value of the trapped ions' charge to mass ratio. Although this was unnecessary in our case since it is obvious we are trapping Ca^+, it was consistent with a mass of 40u.

6.2.2 Laser cooling in a Paul trap

The level structure of Ca^+ without any Zeeman splitting is shown in Figure 6.4. The strong dipole transition $S_{1/2}$ – $P_{1/2}$ is used to laser cool the ions as explained in Section 3.2. As the electron cycles through the $S_{1/2}$ and $P_{1/2}$ states during cooling, the atom may decay via an allowed transition to the $D_{3/2}$ level. The branching ratio for this decay as opposed to the decay to $S_{1/2}$ is approximately 1:16. Since this level is metastable (lifetime 1.2s), any ion falling into this state would ordinarily be lost from the laser cooling cycle. It is therefore necessary to apply a repumper laser beam at 866nm to empty the $D_{3/2}$ state. Since $P_{1/2}$ – $D_{5/2}$ is not an allowed transition, there is no appreciable decay from the $P_{1/2}$ state to the $D_{5/2}$ state (although there is an allowed decay to this state from the $P_{3/2}$ state).

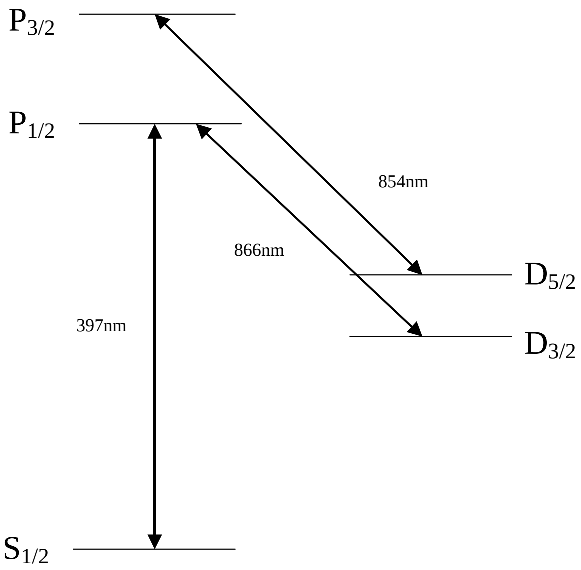

Figure 6.4: Level diagram for Ca^+

Initially, the trap was loaded as in Section 6.2.1. After the trap was loaded, the 397nm cooling laser and the 866nm repumping laser were applied to the ions. The cooling laser was set to the red side of the transition by reference to the hollow cathode lamp and was scanned using the piezo electric transducer in the Littrow cavity. The width of the scan is 3.6GHz in a time of about 1s. The scan is controlled using the 'scan controller' integrated into the TUI drive electronics.

A feed forward is activated between the piezo voltage and the drive current. This allows the laser to be scanned further using the piezo controls before it mode hops to a new wavelength. The level of feed forward is adjusted so as to maximise the piezo scan range between mode hops. This was measured using a plane-plane Fabry-Perot interferometer with invar spacers. As the laser frequency is scanned, the ring pattern formed at infinity by the Fabry-Perot will smoothly collapse towards the centre. If a mode hop occurs in the laser then there will be a small range of piezo voltages which will give many rings and then the ring pattern will reappear shifted to a different place in the frequency spectrum.

Under optimum conditions there were three such mode hops over the 40V range of the piezo (a scanning range of about 7.5GHz without a mode hop). By central spot scanning methods, the change in frequency for a given change in piezo voltage was measured at 0.60GHz/V.

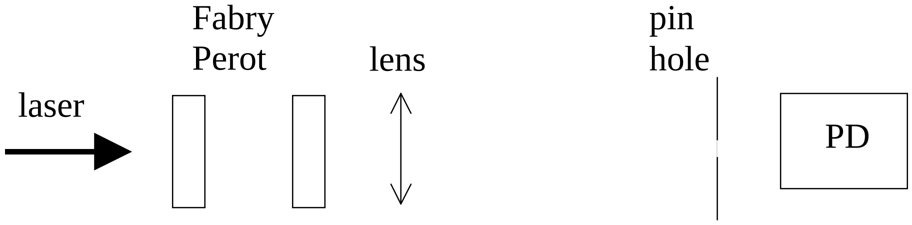

Figure 6.5: Schematic of the central spot scanning arrangement

The 866nm repumper was set to within 400MHz using the wavemeter. The fluorescence signal from the trapped ions is dependent on both the repumper and cooling laser frequencies. As these were brought closer to resonance with their respective transitions, the fluorescence increased. If the system is set up as described above, it is usual to see some signal from the ions immediately upon loading the trap. Changing the centre frequency of the scanning laser (manually adjusting the offset of the piezo voltage), will allow the laser to scan over different parts of the absorption line. The same is true for the non-scanning 866nm laser, which may be tuned in frequency with its piezo. Changing the angle of the dichroic mirror will move the blue beam around the trap. By iterating these three adjustments, it is possible to home in on a position whereby the blue laser scans from the red side of the $S_{1/2}$-$P_{1/2}$ transition up to resonance, the infrared laser sits on resonance with the $D_{3/2}$-$P_{1/2}$ transition and the beam passes close to the centre of the trap, providing maximum cooling of the trapped ion cloud.

It was found that, in practice, the two lasers described above were not sufficient to provide the maximum fluorescence signal or optimal Doppler cooling. The reason for this is that there is an amount of ASE (Amplified Spontaneous Emission) light emitted with the laser light at 397nm. This light has a broad band nature and is a shoulder to the main emission at 397nm. The ASE is emitted over several nanometres. Despite the ASE at 393nm being at a comparatively low power (compared to the laser emission), it is enough to excite the $S_{1/2}$ – $P_{3/2}$ transition weakly. Any population excited into the $P_{3/2}$ level may decay back to the $S_{1/2}$ level via an allowed transition. The ions would then continue their cooling cycle with little or no hiatus. However, if the ion decays to the $D_{5/2}$ level (again by an allowed transition), then there is no allowed decay back to the ground state. The $D_{5/2}$ level is metastable with a lifetime of $\tau = 1.2$s. Any ions caught in the $D_{5/2}$ state will remain there for an extended period of time and will not take part in the laser cooling (or fluoresce). These ions will still be heated via micromotion caused by the rf drive potential and so they will lead to an increase in temperature of the whole cloud and a corresponding drop in fluorescence. Since the excitation of the $S_{1/2}$ – $P_{3/2}$ transition is at a very low level, it is possible to see the effects of fluorescence and laser cooling with the apparatus described above (i.e. one 397nm and one 866nm laser).

Application of a third laser at 854nm ensured that the $D_{5/2}$ level was emptied. It is notable that much less laser power was required to empty this transition than even the 866nm transition. This is since the ion is seldom present in this state. However, both transitions are well over-saturated by our laser systems. Theoretical calculations imply that 0.27mW/mm^2 of radiation is needed to saturate[1] the 866nm transition. This is much less than our applied power (1mW in a 50μm diameter beam gives $\sim$ 500mW/mm^2). When the 854nm laser is applied to an otherwise optimised system (as described above), the signal increases by a factor of two. This implies that roughly half of the ions were in the $D_{5/2}$ state at any one time before the 854nm laser was introduced. Thus, since each ion spends roughly half its time in a state with a lifetime of 1.2s, it is also pumped into this state after an average of 1s in the cooling cycle.

6.2.3 Nulling the residual magnetic field

With good cooling, it was possible to stop the laser scanning and maintain a constant fluorescence signal. The laser can be tuned manually using the

---

[1] The saturation power is taken to be the power at which the probability of spontaneous and stimulated decay is equal. The formula used to calculate the saturation power S is $S = 4\pi^2\hbar c\Gamma/\lambda^3$ [97], where Γ is $22 \times 2\pi$MHz.

piezo and set to the position of maximum fluorescence. This is the line centre. The fluorescence will be constant in time (albeit with intensity noise from the laser imposed on top). One may then apply very small magnetic fields to the trap. Since the trap is designed for use as a Penning trap, it is permanently located between the poles of a large, conventional, electromagnet. Even when there is no current flowing in the magnet coils (i.e. the magnet is off) there is still a small residual field generated by the pole pieces. This is of the order of 1mT. This field Zeeman splits the levels by a small amount and so the lasers will not address the states with maximum efficiency. This is particularly true for the 397nm laser. By applying a small current (~10mA) through the coils in the reverse direction, it was possible to tune the resultant magnetic field over a range of values. This range includes the point where the permanent and induced fields cancel and the field is nulled.

6.3 Temperature measurements

An upper bound on the temperature of a cloud of Doppler cooled ions in the trap can be derived from fluorescence measurements. The amount of fluorescence depends on the strength of the interaction between the laser light and the ion. The lineshape of the cooling transition can therefore be mapped out by taking the fluorescence level for different laser detunings from line centre. Scanning the laser over the line will therefore give its width. Assuming that the natural (Lorentzian) linewidth is much smaller than the Doppler broadened (Gaussian) linewidth, then these peaks can be fitted with Gaussian profiles. The temperature of the ions can be derived from the FWHM of these profiles using

$$T = \frac{\Delta\nu_D^2 mc^2}{4\nu_0^2 2k_B \ln 2} \tag{6.1}$$

where m is the mass of the ion, $\Delta\nu_D$ is the FWHM in Hz and ν_0 is the frequency of the transition in Hz.

This method of measuring temperature will only give a guide to the temperature of the ions. It is therefore reasonable to fit the curves with a Gaussian function rather than the more technically accurate pseudo-Voigt[2].

---

[2] The formula for the pseudo-Voigt is a weighted sum of the Lorentzian and Gaussian components

$$V_{pseudo} = (1-\eta)G(\Gamma_G) + \eta L(\Gamma_L) \tag{6.2}$$

where Γ is the linewidth and η is a mixing parameter constrained by $\eta = 1.33603(\Gamma_L/\Gamma) -$

As stated above, this method will only ever produce a rough upper bound on the ions' temperature. The fact that the natural linewidth of 20MHz and the laser linewidth of 2MHz are convolved with the Doppler linewidth to give the total linewidth produces only small errors. The largest source of error comes from the fact that the laser cooling itself is a dynamic process which depends critically on the detuning of the laser. Thus, when the laser is detuned far from resonance, the cooling is weak and the ions are comparatively hot. The Gaussian line profile is broad. As the laser is brought closer to resonance, the cooling increases and so the line is sharper and narrower. When this profile is plotted, the width will be broader than it would be if the ions were at their coldest throughout the entire scan. It should be noted that the laser is scanned repeatedly and continuously, so the heating described above is due to $\sim$ 2s of interaction with the environment. Only the red side of the transition is measured in this way. If the laser were scanned over the line centre then the ions would be actively heated by the laser.

The lowest temperature measured for our Paul trap is 5K. In general, colder temperatures are observed for smaller clouds of ions since the micromotion is also smaller and so there is less rf heating. Over-saturating the 397nm transition tended to broaden the fluorescence peak, but this could be overcome by filtering the laser which produced lower temperatures. A sample fluorescence trace for a laser scan over 3.6GHz is shown in Figure 6.6.

It is believed that this temperature is limited by micromotion. Micromotion is caused by the large rf fields ($\sim$ 250V) present in the Paul trap. These electric fields cause the charged ions to vibrate and hence to be heated. For a perfect Paul trap, the micromotion is zero at the trap centre. However, in a real trap, patch potentials on the trap electrodes will cause the ions to sit away from the trap centre. This can be corrected by extra compensation electrodes, but these are not available for our trap. Since our goal is to work in the Penning trap, lower temperatures were not pursued further in the Paul trap.

6.4 Small clouds and a single ion

If the oven producing calcium atoms is heated less, then fewer atoms are produced. This can be achieved by passing less current through the heater wire attached to the oven and results in smaller clouds of ions being trapped. By carefully reducing the current further and further, it is possible to load a single ion into the trap. The method of quantum jumps can be used to determine the number of trapped ions if there are one or two ions trapped.

$0.47719(\Gamma_L/\Gamma)^2 + 0.11116(\Gamma_L/\Gamma)^3$.

Small clouds of ions show markedly less heating than large clouds of ions. The FWHM of the transition is much smaller for small clouds and the peaks are therefore much sharper. Examples of the fluorescence are given in Figure 6.6 as the cooling laser is scanned over the line for a large and small cloud respectively.

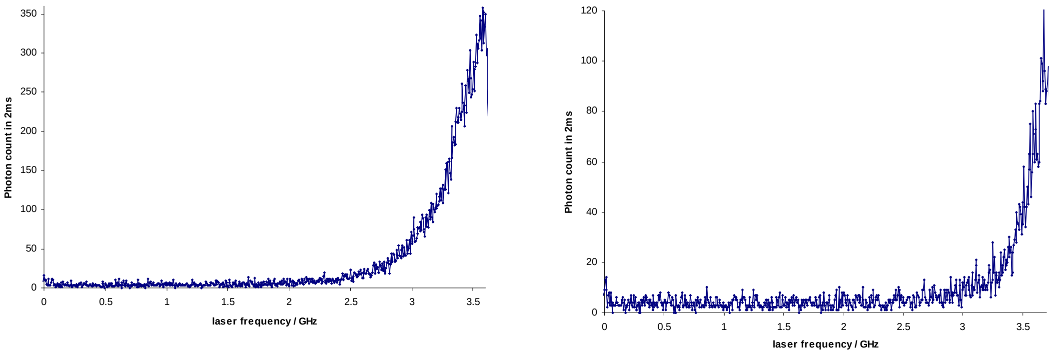

Figure 6.6: Fluorescence traces showing large and small clouds of ions respectively. Temperatures are 34K and 5K respectively. The position of the centre of the peak is not known exactly, so the start of the scan is arbitrarily labelled as zero frequency.

For the case of a single trapped ion laser cooled on the $S_{1/2}$-$P_{1/2}$ transition with one repumper at 866nm (and a laser detuned from the 854nm transition), there is a constant level of fluorescence. However, if the ion is excited by ASE to the $P_{3/2}$ level, then it may decay to the metastable $D_{5/2}$ level. The fluorescence will then cease until the ion has decayed back to the ground state. This pattern of fluorescence is observed as shown in Figure 6.7. The theoretical maximum signal is 5000 counts per second[3]. This compares with our observed signal of 1500 counts per second for a single ion. Two ions will produce a similar pattern but with two steps since either two, one or no ions may be fluorescing (see Figure 6.8). Any cloud much larger than this is seen to wash out the steps. The signal to noise ratio of the data could be improved by adding compensation electrodes to the trap. By application of extra electric fields, the ion could be moved to the position where the micromotion is minimised. This would allow the ion to cool to a lower temperature and the signal would improve.

---

[3] The population is divided equally between 8 levels (two from $S_{1/2}$, two from $P_{1/2}$ and four from $D_{3/2}$) of which two emit fluorescence at 397nm during decay. The linewidth is 22MHz and the theoretical maximal detection efficiency is 2×10^{-3} for our apparatus. For optimal cooling the laser is positioned half way down the peak. The theoretical maximum signal we would see is therefore $22 \times 10^6 \times 2 \times 10^{-3} \times 2/(8 \times 2) = 5000$.

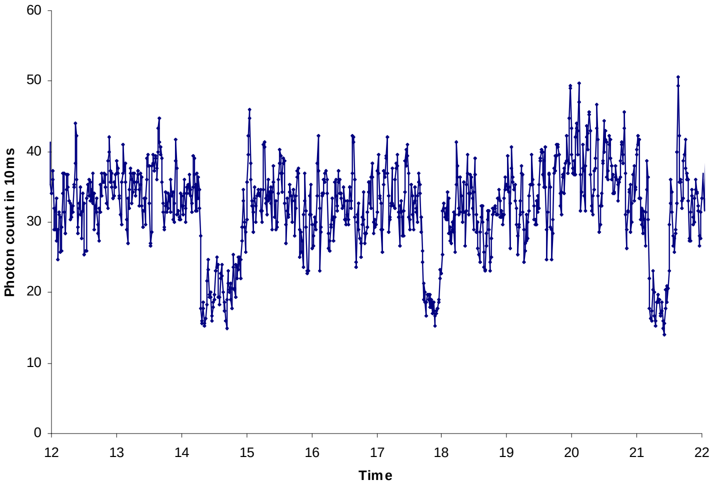

Figure 6.7: Example of quantum jumps in a single Ca^+ ion in a Paul trap. The lower level is the background level due only to scattered laser light.

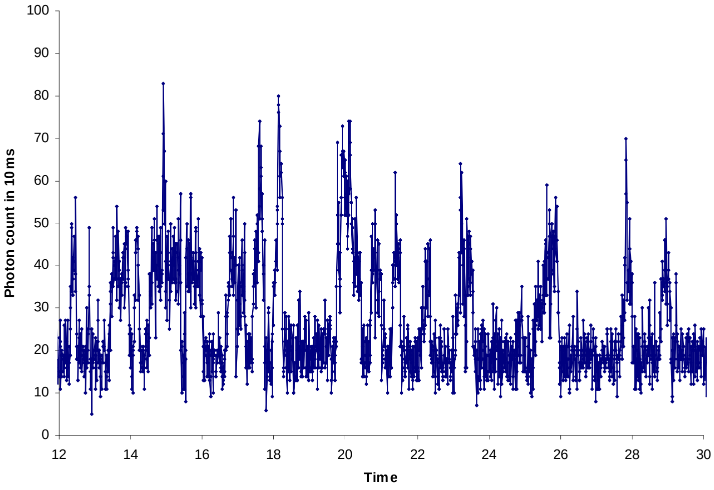

Figure 6.8: Example of quantum jumps for two trapped Ca^+ ions in a Paul trap.

Chapter 7

The combined and Penning traps

Only two species of ion had been laser cooled in a Penning trap before this work. Both of these had similar features of their energy level scheme that allowed cooling with the application of only one laser. In this chapter, work done in the combined and Penning traps on Ca^+ is discussed. Apart from demonstrating laser cooling of a third species of ion in a Penning trap, we also demonstrate a novel scheme where two equivalent cooling lasers are used.

This chapter also clarifies the difference between laser cooling in a Penning trap and in a Paul trap. The level structure of Ca^+ is different in a magnetic field due to the large Zeeman splittings between the levels. The calibration of the magnetic field applied to the trap is discussed and results presented. The optical setup and the additional lasers needed to laser cool Ca^+ in the presence of a magnetic field are also described.

7.1 The combined trap

By applying an axial magnetic field through the endcaps of the Paul trap, it is converted to a combined Paul/Penning trap. The combined trap is actually more stable than either the Paul or Penning trap over a wider range of masses [98]. However, the application of a magnetic field splits the atomic energy levels into $2J+1$ components. Because of this Zeeman splitting, the combined trap necessitates the use of more lasers to perform Doppler cooling than in the Paul trap. Application solely of the lasers used to cool in the Paul trap results in optical pumping to the unaddressed Zeeman sub-levels and laser cooling will cease. The level scheme of Ca^+ in a magnetic field is as in Figure 7.1. Even for moderate fields of 0.1T, it is necessary to use two

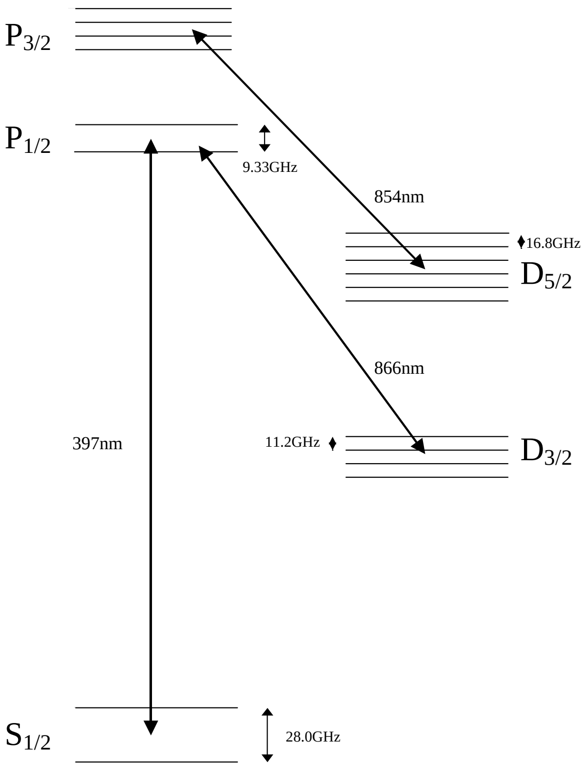

Figure 7.1: The level scheme of Ca^+ in a 1T magnetic field.

cooling lasers at 397nm. It is believed this is the first time that two equivalent cooling lasers have been used to laser cool an ion. Extra lasers may also be required to empty the $D_{3/2}$ levels. The optical schematic is shown in Figure 7.2.

Initially, the magnetic field was increased from zero field in steps of 0.1T. After each increase in magnetic field, the fluorescence dropped and the laser frequencies needed to be readjusted. However, there was still enough of the fluorescence signal detected to re-optimise the frequencies of the two blue lasers. In this situation, the frequency of both of these lasers is critical. Since each acts strongly on the transition and has a nominally equal role in cooling, it is found that the cooling (and hence the fluorescence signal) is limited by the least optimised laser (see Section 4.2.2 for more discussion). The general method employed was to optimise one laser manually by bringing it into resonance with its line (with no automated scan) whilst the other laser continually and automatically scanned in frequency as described for the Paul trap. The centre frequency of this scan was then positioned so as to provide optimal fluorescence. Both the π and the σ transitions have been driven

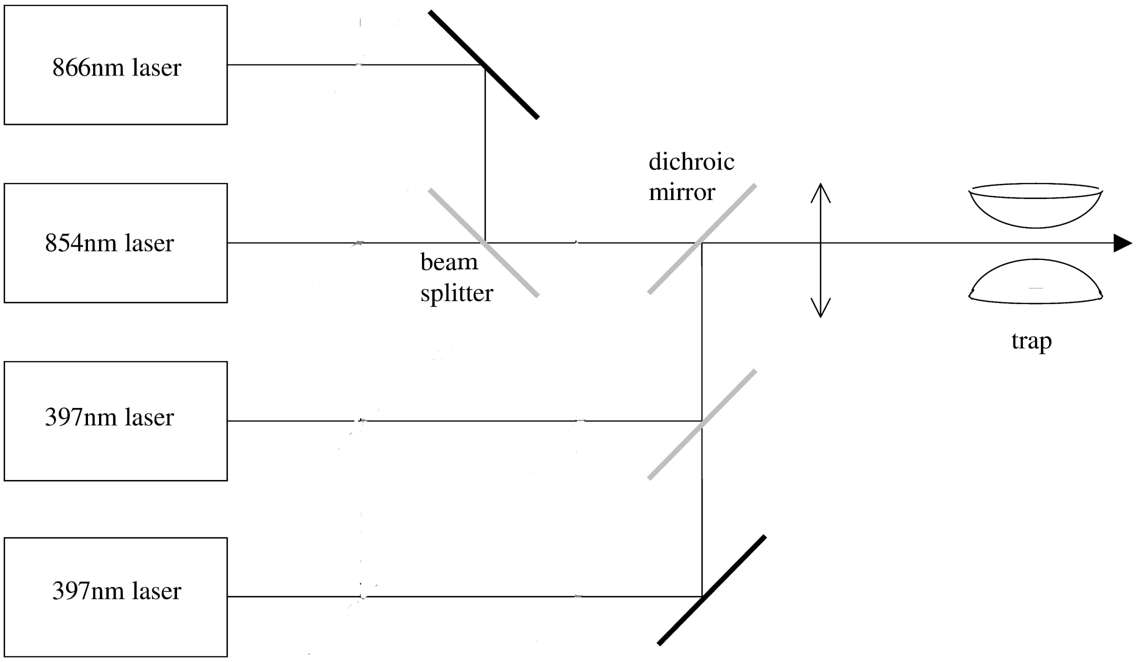

Figure 7.2: Optical layout for laser cooling in the combined and Penning traps.

in this manner at separate times[1]. The maximum magnetic field which the magnet could produce was about 1T. By stepping the magnetic field in this fashion it was possible to reach high enough fields to operate a pure Penning trap (albeit with the changes to the laser systems described below). With experience, jumps in field of up to 0.3T could be used. This process of bridging the gap between the zero magnetic field Paul trap and the 1T field Penning trap allowed the lasers to be set at the correct wavelength for the Penning trap transitions without additional spectroscopy. This was not only important for accomplishing the goal of laser cooling Ca^+ in a Penning trap, but also of interest in its own right. This is the first time that Ca^+ has been trapped and laser cooled in a combined trap. The peaks become noticeably less broad and the signal greater as the lasers are optimised.

As the magnetic field is increased, the $D_{3/2}$ level splits into four sublevels. In theory these four levels could be emptied by using four separate lasers. However, it is notable that these levels require much less energy to saturate than our laser produces. These levels could therefore be emptied to a reasonable extent by an unusual method of running the 866nm laser. If the frequency of this laser was tuned using the piezo until it was on the boundary of a mode hop, then it would run in a semi-broadband manner. If a 7.5GHz spectrum analyser is used to study this light, then it is characterised by a broad, irregular background punctuated by broad peaks. Some values of driver current allowed this behaviour to occur more readily. In this mode, the laser produced enough light over a broad spectrum to provide some repumping on all four of the $D_{3/2}$ levels. Thus despite the splitting of the $D_{3/2}$-$P_{1/2}$ transition into six components, it was possible to see significant fluorescence at all values of magnetic field up to 1T (the maximum our magnet can deliver).

7.1.1 Cooling in a combined trap

As the magnetic field was increased, reoptimisation of the lasers at each field value failed to recover the full fluorescence signal. The peaks also become progressively broader, indicating that the ions are not as cool at higher magnetic fields. This is attributed to two factors. Firstly, the cooling is not as efficient at large fields. Zeeman splitting of the $D_{3/2}$ level is such that one infra-red laser at 866nm is not sufficient to saturate the $D_{3/2} - P_{1/2}$ transition. This leads to a partial shelving of the population in the $D_{3/2}$ level, which can be solved by applying more lasers close to 866nm. The second

---

[1] The π transitions were chosen for the subsequent work since their smaller Zeeman splitting required the frequency of the lasers to be moved less in going from the Paul to the Penning trap. The required laser polarisation was chosen using an oblique periscope.

factor is due to the drift of the ions round the trap centre induced by the magnetic field. Application of a magnetic field to a Paul trap produces the combined trap and synthesises the micromotion characteristic of the Paul trap with the magnetron drift of the Penning trap. Effectively, this forces the ions to drift around the trap centre and hence they are radically affected by micromotion. As described earlier, the action of the micromotion serves to heat the ions. Sample traces at various magnetic fields are shown in Figure 7.3.

7.2 The Penning trap

The Penning trap is described in detail in Section 3.1.1. The trap electrodes themselves are the same as for the Paul and combined traps. In this case, the ring is held at a DC potential of -6V and a magnetic field of 0.75 to 1T is applied axially through the endcaps. It is possible to operate the Penning trap with the optical setup described for the combined trap, however to optimise cooling a better optical setup was chosen involving several lasers close to 866nm (Figure 7.4).

7.2.1 Motional frequencies

In any trap, the ions move with well defined frequencies. These frequencies depend on the trap parameters (DC voltage, magnetic field, electrode dimensions) as well as the charge and mass of the ions. In the Penning trap, the three frequencies are given by the following formulae:

$$\text{Axial} \qquad f_z = \frac{1}{2\pi}\sqrt{\frac{4eU}{mR^2}} \tag{7.1}$$

$$\text{Modified cyclotron} \qquad f_+ = 1/2(f_c + \sqrt{f_c^2 - 2f_z^2}) \tag{7.2}$$

$$\text{Magnetron} \qquad f_- = 1/2(f_c - \sqrt{f_c^2 - 2f_z^2}) \tag{7.3}$$

where f_c is the cyclotron frequency, $f_c = eB/2\pi m$. All the above are in hertz.

If a small amplitude ($\sim$ 10mV) radio frequency signal is applied to one endcap (with the other grounded as usual), then the ions can still be trapped. If the frequency of this rf field is scanned over the region of one of the motional frequencies, then energy will be coupled into the ions from the field as the frequencies become equal. Since the rf drive that excites the ions is small, it is known as the 'tickle voltage'. When energy is coupled into the ions'

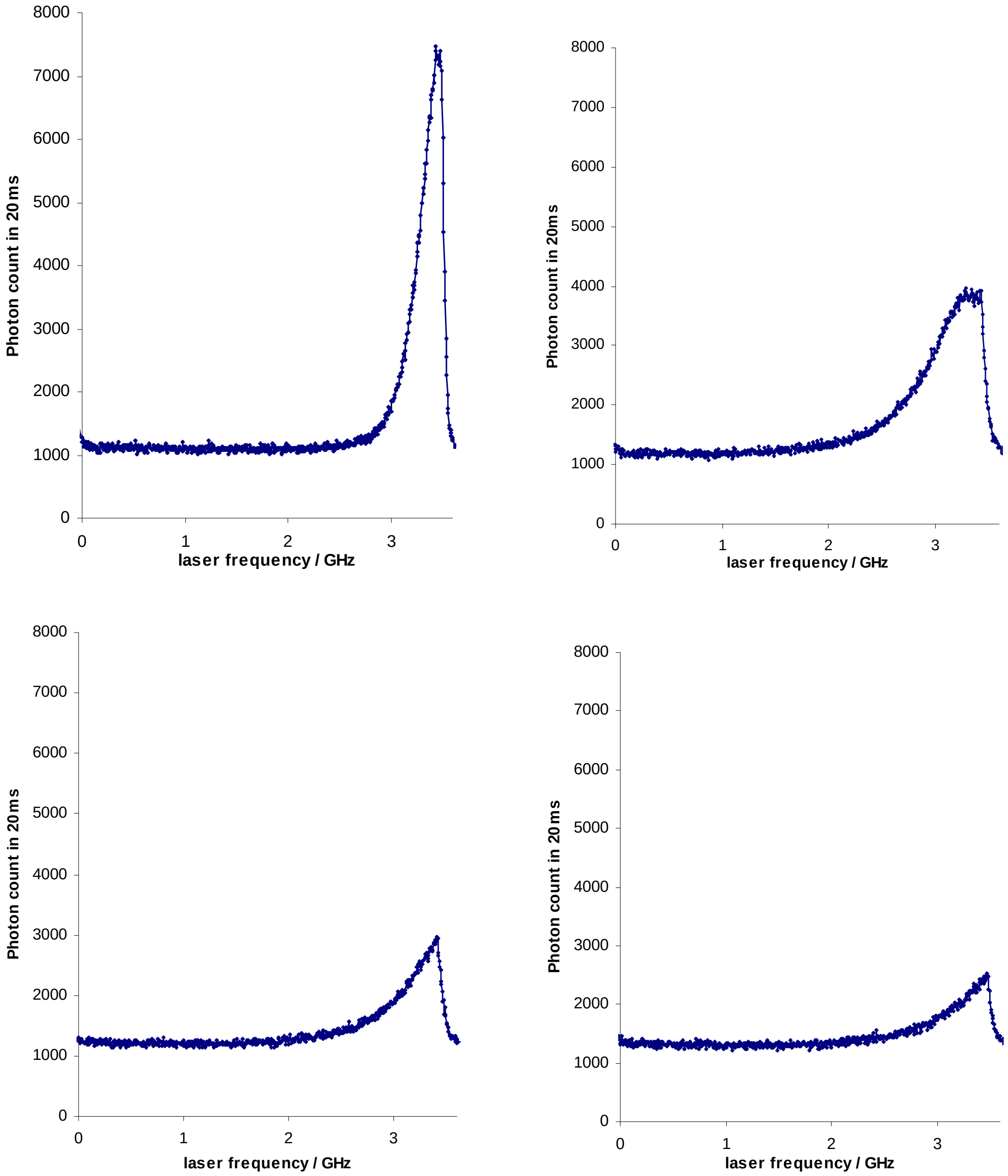

Figure 7.3: Graphs showing the fluorescence from ions trapped in a combined trap as one blue laser is scanned up to resonance with the $S_{1/2}$-$P_{1/2}$ transition. The four graphs are for magnetic fields of approximately 0, 0.1, 0.4 and 0.6 T respectively. The start frequency of the scan is zero and is reset for each graph.

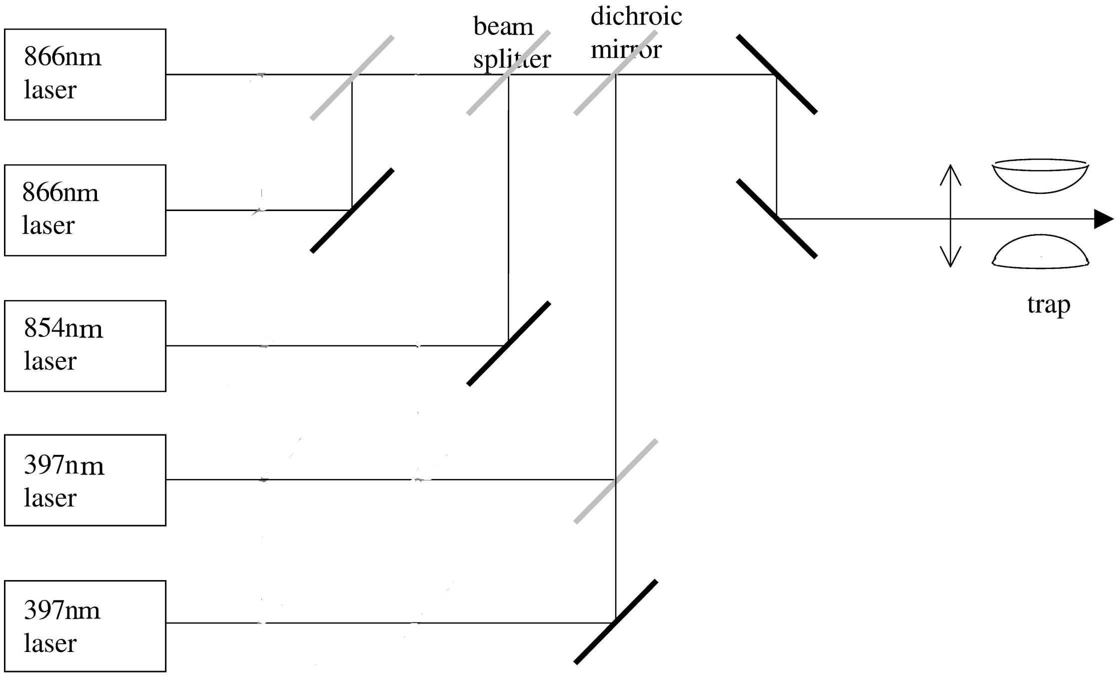

Figure 7.4: Optical layout for laser cooling in the Penning trap.

motion, the ions are heated. As the ions are heated, the cloud grows rapidly to a size bigger than the laser beam. The laser cooling is not as effective and the fluorescence signal decreases. The ions will then return to the beam after the tickle voltage frequency has moved on. A sample trace is given below in Figures 7.5 and 7.6 for the magnetron motion.

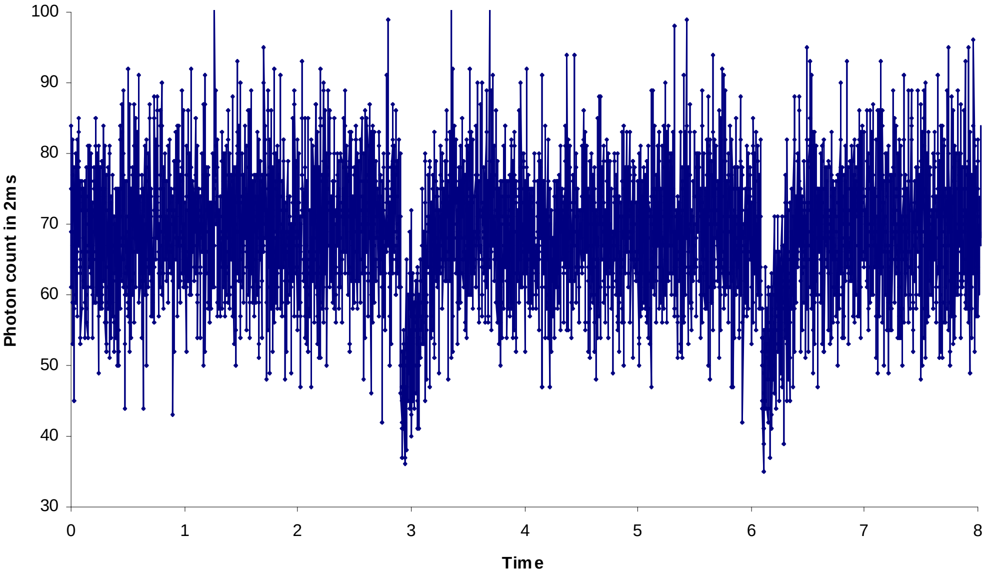

Figure 7.5: Example trace showing the fluorescence dip associated with applying the rf tickle voltage for one scan. The frequency is scanned linearly upwards for the first 4.5s and then decreases linearly for the next 4.5s. There is therefore a point of reflection at 4.5s. See description in text.

Here, both cooling lasers are set at a constant frequency close to resonance. The MCS is triggered at the start of the tickle voltage scan. The tickle voltage scans up from 20kHz to 70kHz and back down. The scan up and down takes 9s, of which the trace shows the first 8s. It is therefore possible to calculate the frequency of the tickle voltage which causes the dips from the bin numbers on the MCS. In this case, this gives the magnetron frequency for a current of 9.0A flowing through the magnet coils. The tickle voltage amplitude was 7.5mV for this scan and the measured frequency 52.4kHz and 52.3kHz for the up and down scans respectively. Note that the leading edge of the dip is always the sharpest. This is because the ions take time to cool back into the beam once they are heated. Most consistent results are therefore obtained by taking the leading edge of the dip as the motional frequency.

Both magnetron and modified cyclotron resonances were measured at a number of different magnet currents. Since the cyclotron frequency f_c is the

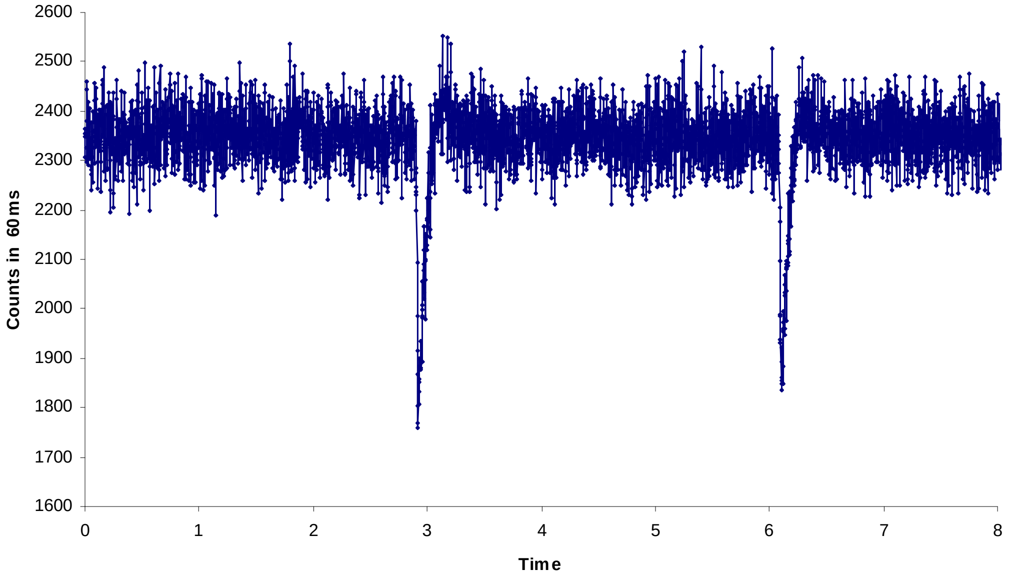

Figure 7.6: Example trace showing the fluorescence dip summed over many scans. The leading edge of the dip is less sharp than for one scan since the magnetic field drifts during the measurement.

sum of these two frequencies, then an accurate calibration of the magnetic field can be obtained (since $f_c = eB/2\pi m$). The cyclotron frequency itself could also be excited, although the conditions under which this occurred were not controllable. This gave broad dips which were difficult to measure accurately, so direct excitation of the cyclotron motion was not used as a general method.

To provide assurance that the dips we believed to be the magnetron and modified cyclotron were indeed those resonances, some values for the axial frequency were taken. These were difficult to measure since energy supplied to the endcap is well coupled into the axial motion and so the ions tend to be driven out of the trap completely. A potential divider was constructed to reduce the tickle voltage to below 1mV. Several axial frequencies were measured for different DC voltages applied to the trap. This gives an independent measure of R, the trap parameter. R is expected to differ significantly from the theoretical value ($R^2 = 2z_0^2 + r_0^2$) due to imperfections of the trap electrodes and patch potentials.

A trace summed over 30 scans is provided for the magnetron frequency at 9.0A magnet current (Figure 7.6). The dip is broader for 30 scans since the magnetic field drifts slightly over time. This is shown in case the reader has any doubt over the dip shown in the original data, which is only marginally larger than the noise. The ions were deliberately driven at this weak level to minimise the heating and hence the width of the dip. In practice the dips at this level were readily distinguishable from the noise due to their repeatability.

The calibration of the magnetic field by this method is shown in Figure 7.7. This method affords a way to measure the magnetic field accurately at the position of the ions, which will be useful for future studies.

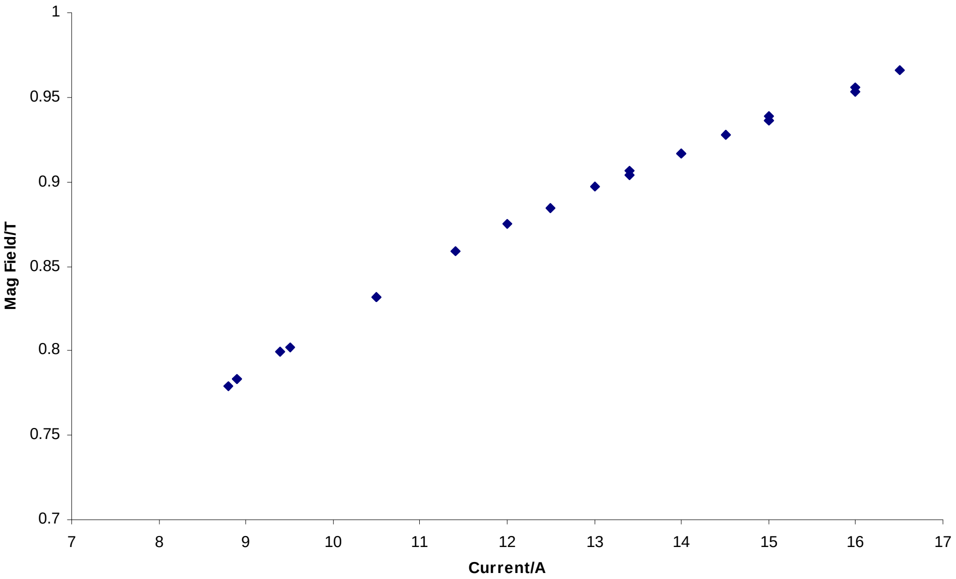

Figure 7.7: Calibration of the magnetic field using the motional frequency method for ions in the Penning trap. The abscissa is the current in the coils of the electromagnet.

7.2.2 Driving the $D_{3/2}$ state

As discussed earlier, the $D_{3/2}$ sub-levels must be emptied for efficient laser cooling to take place. To see some fluorescence signal it is possible to repump using the poorly understood behaviour of one laser close to a mode hop. However, to get good cooling it is desirable to empty the levels completely. Three methods for achieving this have been investigated.

Microwave method

The first method is to repump strongly on one sublevel with the 866nm laser and to mix the other $D_{3/2}$ states into this one by direct microwave excitation. This involves applying microwave radiation at a frequency commensurate with the separation of the Zeeman split sublevels. In order to try this approach, a signal generator (Agilent 83650L) was used to supply the microwave radiation.

Three different approaches to delivering the microwaves into the trap were tried: 'horn', 'oven' and 'endcap'. The 'horn' method used a microwave horn to shine a beam of microwaves through the exit window of the trap. The horn was well matched to the 50Ω impedance of the signal generator. However, since the horn must necessarily be outside the vacuum can, it was impossible to get the source closer than 0.55m to the trap. Assuming a ray picture, and following the contours of the horn, implies that the microwaves will spread out over an area of 0.052m^2 by the time they have travelled 0.55m. Access to the trap is via a small hole of diameter 3mm (laser exit hole), but microwaves of frequency 11GHz have wavelength 27mm. This approach was unsuccessful, probably due to the very limited power coupled into the trap and I believe there is little hope in pursuing it further.

The 'oven' method uses one of the ovens in the trap as an antenna for the microwaves. The microwave generator was connected directly to the electrical feed through which connected to the oven. As above, this method did not yield success. Since the oven is much closer to the trap electrodes ($\sim$ 5mm), this improves upon the situation above. However, the oven was not impedance matched to the signal generator so reflections could be significant. It was hoped that the proximity of the oven to the gap between ring and endcap electrodes would allow the microwaves to penetrate the trap and drive the transition. It is now believed that this is not the case and that the electrode structure acts as quite an effective Faraday cage.

In the 'endcap' method, the microwave generator was again directly connected to the electrical feedthrough, this time to the endcap electrode. It was hoped that this would supply microwaves directly into the trap despite the long wavelength. In order to trap ions effectively, the endcaps must be anchored to a fixed voltage. It was therefore necessary to construct a choke circuit to allow simultaneous DC grounding of the endcap whilst the microwaves were applied. This prevented the microwaves flowing to earth, but allowed the endcap to be at DC ground. This setup did allow ions to be trapped, but did not allow the $\text{D}_{3/2}$ state to be driven successfully with the microwaves. It is suggested that this was either due to impedance mismatch or that the magnetic field drifts too rapidly and the transition is too narrow to effectively drive the transition. Future work could improve upon this if so desired.

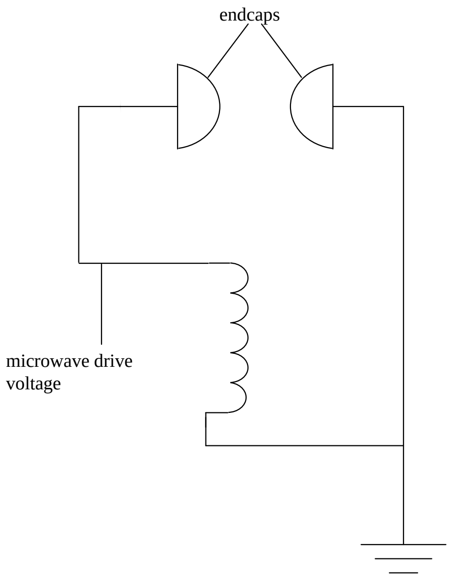

Figure 7.8: Schematic of set-up used to apply microwaves directly to the endcap.

Four laser method

The $D_{3/2}$-$P_{1/2}$ transition is Zeeman split into six components (two π and four σ components). To completely empty the $D_{3/2}$ state it is sufficient to drive the four σ transitions (see Figure 7.10). The obvious way to achieve this is using four separate lasers close to 866nm. This was tried and does work well. Each transition is significantly over saturated by its laser. The drawback of this method is that four separate lasers must be maintained and set to the correct wavelength. They must then all be reoptimised every few minutes to keep them at the correct frequency and counter their drift.

Two laser method

Using only two repumper lasers would considerably reduce the work required to maintain the repumping lasers at the correct frequency. Consider a Penning trap with a 0.8T magnetic field; the splitting of the closest pairs of σ transitions would be 1.5GHz. If a single laser could be placed between these two transitions and driven to produce sidebands at 750MHz from the centre wavelength, then this would drive the transitions directly.

Modulation of the drive current was used to add sidebands to two 866nm lasers. The radio frequency signal generator (Agilent 83650L) was used to provide this modulation. Modulation of the diode current provides phase modulation of the laser light emitted by the diode. The details of why this

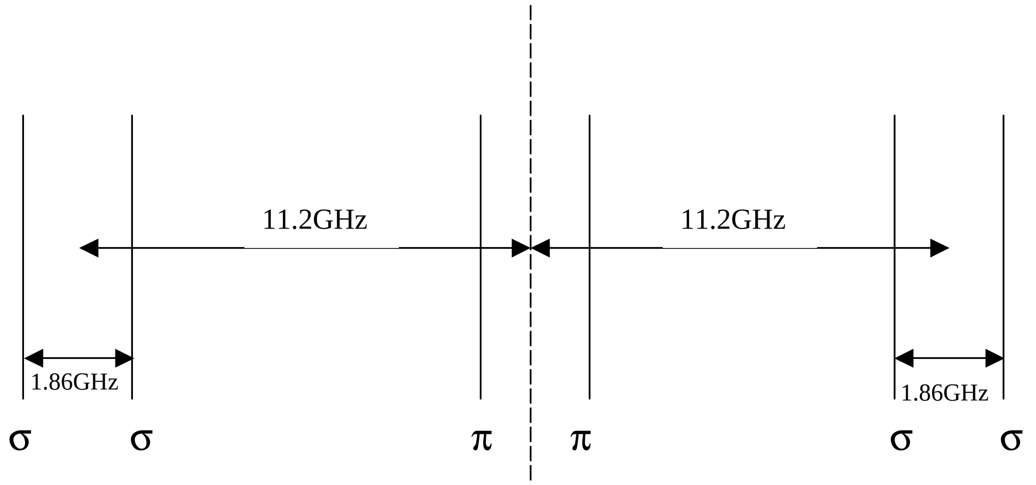

Figure 7.9: Splitting of the $D_{3/2}$-$P_{1/2}$ transition in a 1T magnetic field.

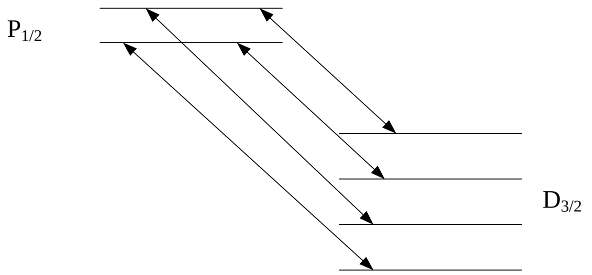

Figure 7.10: Directly driving the four σ transitions will empty the $D_{3/2}$ level effectively.

phase modulation produces sidebands are essentially identical to those explained in Section 8.2.1. The schematic is as shown in Figure 7.11. One of the legs of the laser diode was soldered directly onto a length of rigid cable ($\sim$ 10cm). This cable was clamped in place to avoid any unnecessary strain being placed on the laser diode pins. The DC drive current for the laser diode was provided through a bias T (Minicircuits ZFBT-6G-FT). This effectively acted as a choke, mixing the rf and DC currents together before the laser diode without letting the rf pass into the laser current driver. The stub tuner (Microlab S3-02N) was used to impedance match the 750MHz radio frequency drive into the laser diode.

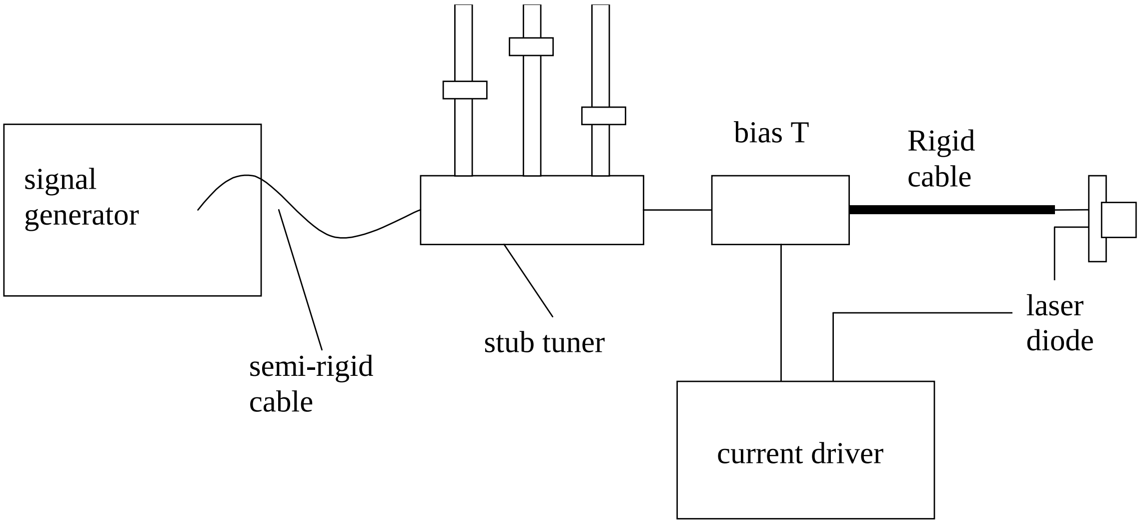

Figure 7.11: Schematic of equipment used to put sidebands onto a diode laser.

The resulting laser light with sidebands was monitored on a spectrum analyser (Tec-Optics SA-2). It was possible to watch the sideband production as the radio frequency power was altered. The amount of light in the sidebands could be optimised using the stub tuner. A modulation power of 5dBm was sufficient to produce significant sidebands.

Our final method to laser cool in a Penning trap was to use two lasers with sidebands. This meant that the centre frequency of two lasers had to be set correctly. The sidebands were set using the dial-up frequency from the signal generator. This was known to be the correct value since the magnetic field had been calibrated using motional frequencies of the ions in the trap. By filtering each laser in turn with a neutral density filter, it has been determined that each of the four σ transitions are saturated in this configuration.

The $D_{5/2}$ state requires little repumping power, since the ions rarely fall into this state. It has been determined that all six levels are effectively emptied by one laser placed between the six 854nm $D_{5/2}$-$P_{3/2}$ transitions.

7.2.3 Laser cooling in the Penning trap

Using two cooling lasers at 397nm, two 866nm lasers with sidebands to repump from the $D_{3/2}$ levels and one laser to repump from the $D_{5/2}$ levels cooling traces of the ion trapped in a Penning trap were recorded. Different laser powers were tried for the lasers. It was found that extra laser power in the 866nm lasers will not degrade the cooling, but that little is gained from running these lasers very much higher than the saturation power. Higher powers in the 397nm lasers caused the fluorescence signal to rise, however it was also found that the cooling effect was weaker for powers higher than some threshold. This has been attributed to two effects: power broadening on the $S_{1/2}$-$P_{1/2}$ transition and increased pumping to the $D_{5/2}$ level (via $P_{3/2}$) by ASE. It was also found that lower powers were needed for smaller clouds.

Figure 7.12 shows a fluorescence scan for a small cloud of ions in a Penning trap which are cooled with the optimum laser powers for low temperatures. The temperature inferred from this trace is 0.5K.

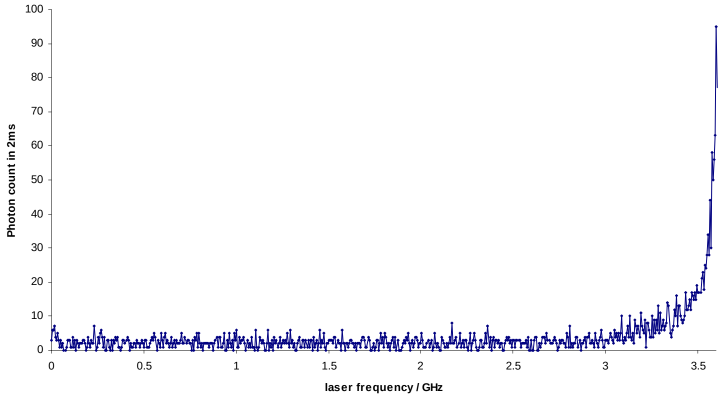

Figure 7.12: Cooling trace for a small cloud of ions in a Penning trap with a measured temperature of 0.5K.

7.2.4 Future work in the Penning trap

Whilst the long term scope of the project is spelt out in Section 3.5, I will now discuss some of the more immediate challenges. The first is to trap a single Ca^+ ion in a Penning trap. A preliminary attempt to follow similar methods used to trap single ions in a Paul trap (see Section 6.4) has so far failed to load single ions. It is believed that this is due to the lasers drifting away from their prescribed transitions. As the lasers drift, the cooling efficiency is reduced and the fluorescence signal is also degraded. Since a single ion will only produce a small signal (with a correspondingly poor signal to noise ratio), any further reduction may make the quantum jumps impossible to observe. To combat this, extensive efforts have already been made to reduce the background signal level by adding extra light baffles round the trap and detection equipment and more careful alignment of the optics.

To facilitate setting the laser frequencies, a new wavemeter will be constructed. This will be based on similar principles to the present one, but will have better resolution by an order of magnitude. This will allow ions to be trapped in a Penning trap without first using the Paul and combined traps. The laser drift will be reduced by locking the lasers to Fabry-Perot cavities. A side of fringe lock will be employed in a manner similar to that described in Section 8.1. This work is being undertaken by K Koo and should reduce the drift by an order of magnitude. The cavities will be temperature controlled but not evacuated. They will be of relatively low finesse (in comparison to the ultra high finesse cavity described in the next chapter) and made from a zerodur spacer. It is hoped that these improvements will allow single Ca^+ ions to be trapped in our Penning trap.

Further work will also include axialisation of a Ca^+ ion in our Penning trap. This will be an extension of work completed recently by our group on Mg^+ in a Penning trap. This requires a different trap geometry to the trap described in this thesis. The trap used in this experiment will be modified to include Ca^+ ovens. This trap will need to have a segmented ring electrode to drive the ions with an additional rf electric field. Under the right conditions this can lead to increased localisation of the ions at the centre of the trap by reducing the magnetron motion.

Chapter 8

Laser stabilisation using the Pound Drever Hall method

This chapter describes the work which I have done in order to lock a Ti:Sapphire laser to a high finesse Fabry Perot cavity. The first part details the theory behind the Pound Drever Hall method of locking a laser and also presents a brief overview of other methods of locking a laser. The Pound Drever Hall method has two distinct advantages over the simple side of fringe lock. The first is a large capture range, which helps ensure that the laser remains locked to the correct frequency. The second is the speed of the lock, which can be used to narrow the linewidth of the laser. The second part of the chapter presents the practical details and results. Work done with Stephen Webster at NPL to build a second Pound Drever Hall lock for their system at 934nm is described. Subsequent work to lock a Ti:Sapphire laser at 729nm to a high finesse cavity at Imperial is also described. These two projects have many similarities in the implementation of the lock (and deliberately so; the joint work at NPL was used to gain experience with this locking method).

The 729nm laser light will eventually be used to address the $S_{1/2}$-$D_{5/2}$ transition in Ca^+. This will serve two functions: to implement sideband cooling and to drive Rabi oscillations on this transition. Since the transition has a narrow linewidth and the vibrational levels of the trap are relatively close together, it is necessary to use a very stable laser with a low linewidth.

8.1 Laser stabilisation

Laser stabilisation has two main goals: to stop the laser drifting in frequency over long timescales and to narrow the linewidth of the laser. Consider the case that the laser has deviated from its required frequency. There should then be some way to diagnose this and pull the laser back to the correct frequency. This requires that there is some device, either as part of the laser cavity or external to it, which can alter the frequency of the laser. A piezo electric transducer attached to one of the laser cavity mirrors or an external AOM to shift the frequency after the light has left the laser are two such devices.

However, the device for shifting the frequency must know which way to change the frequency and by how much. This requires a function which has odd symmetry about the required frequency (at least for small frequency deviations). This function is the error signal, and one should note that it has one sign for frequencies above the required frequency and the other for frequencies below. This simple requirement of a signal whose sign depends on the frequency relative to the lock point can be achieved with a device with a frequency-dependent response, such as a Fabry-Perot cavity and a way to produce an offset.

Perhaps the simplest method to (actively) stabilise a laser would be to lock it to some point on the side of one of the Airy function transmission peaks of a Fabry-Perot cavity (Figure 8.1). This converts frequency fluctuations into amplitude fluctuations, which can be measured on a photodiode.

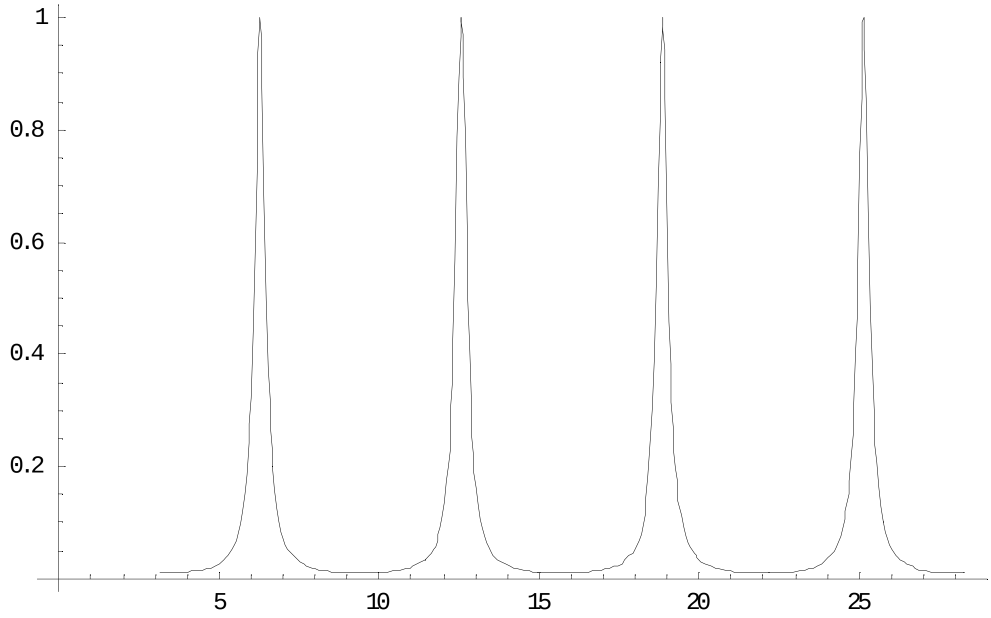

Figure 8.1: The Airy function, with a finesse of 13

Unfortunately this method suffers drastically if there are intensity fluctuations on the laser light since these cannot be distinguished from frequency fluctuations. Intensity fluctuations can be overcome by splitting the light into two, and using one beam as a reference for the intensity whilst the other passes through the Fabry-Perot. The two light levels can then be subtracted, cancelling out any intensity fluctuations (Figure 8.2). Unfortunately this requires that the photo-diodes are matched for frequency response and drifts over time. Also note that if the frequency of the laser jumps too far, then it may fall on the wrong side of the Airy peak and so the laser will rapidly lock to the wrong point (i.e. a different fringe). The frequency range over which the laser is correctly locked is the capture range.

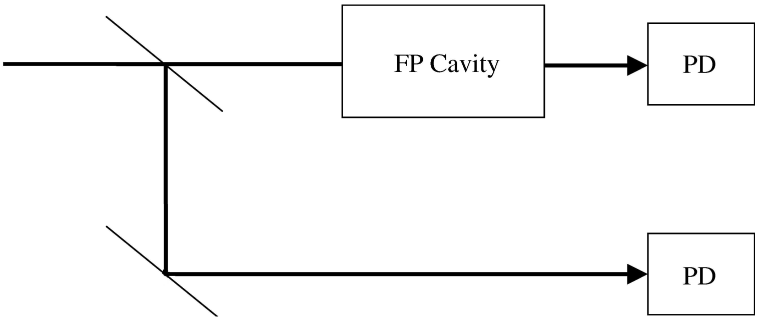

Figure 8.2: Balanced photodiode approach to a side of fringe lock

Hänsch and Couillaud [99] first proposed a technique using polarization at Brewster angled surfaces within the cavity to increase the capture range and thus help to alleviate the mode-hopping problem. This scheme produces a dispersion shaped curve and so the laser can be locked to a point of 0V. However Drever and Hall [100] proposed and implemented a new system based on a microwave stabilisation technique proposed by Pound [101] which only uses one photodiode, has a large capture range and also locks to a point of 0V.

8.2 The Pound Drever Hall method

This is a method of locking a laser to a Fabry-Perot cavity, which uses only one photodiode and has a large capture range. It also has the significant advantage of providing a very fast lock, since it is based on the prompt reflection from the front face of the Fabry-Perot cavity. This is important for reducing the linewidth of the laser light since it increases the bandwidth of the lock. The basic schematic for producing the error signal and applying it to the laser is as in Figure 8.3.

Some of the laser light is picked off from the main beam. It is sent through an EOM, which imposes a phase modulation on the light. The frequency

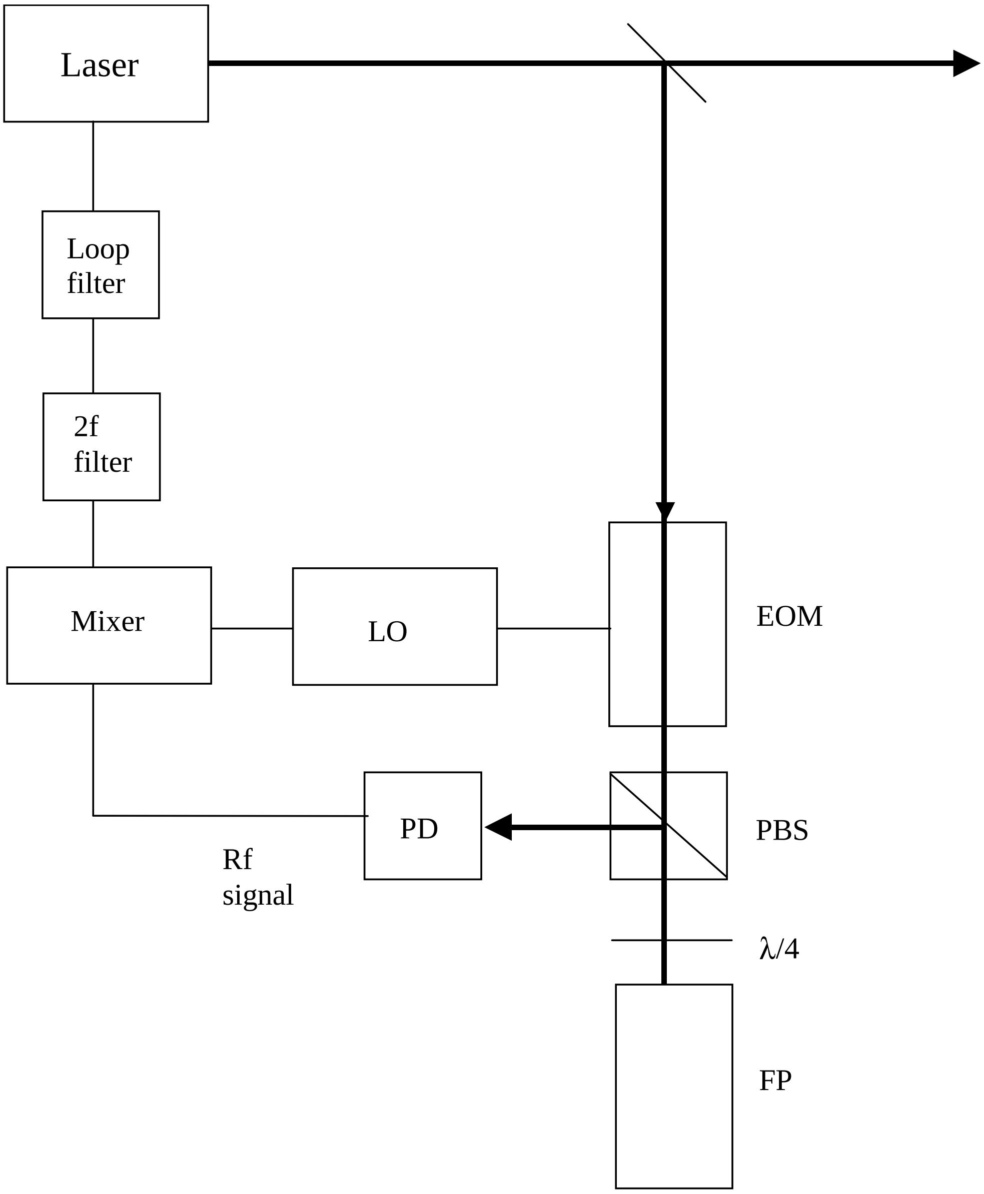

Figure 8.3: Schematic for Pound Drever Hall lock. Feedback is shown to the laser, but feedback may also be sent to an AOM in front of the laser.

of this modulation is set by the local oscillator (LO) which determines the frequency separation of the sidebands imposed on the light by the EOM. The light then passes through the polarising beam splitter and the $\lambda/4$ plate. The light reflected from the Fabry-Perot cavity passes through the $\lambda/4$ plate again and is reflected from the polarising beam splitter onto the fast photodiode. The photodiode (rf) signal and the local oscillator signal are then passed through the electronics to produce the Pound Drever Hall error signal which is fed back to some frequency control element at the laser.

8.2.1 Theory of the Pound Drever Hall Method

The light (angular frequency ω) from the laser is subjected to a sinusoidal phase modulation of depth m and modulation frequency Ω

$$E_t = E_l e^{i(\omega t + m\sin\Omega t)} \tag{8.1}$$

But

$$e^{i(m\sin\Omega t)} =$$

$$J_0(m) + 2\sum_{k=1}^{\infty} J_{2k}(m)\cos(2k\Omega t) + 2i\sum_{k=0}^{\infty} J_{2k+1}(m)\sin((2k+1)\Omega t)$$

so

$$E_t \approx E_l e^{i\omega t}(J_0(m) + 2iJ_1(m)\sin(\Omega t)) \tag{8.2}$$

taking only terms up to J_1 (assuming the modulation m is small). i.e.

$$E_t \approx E_l(J_0(m)e^{i\omega t} + J_1(m)e^{i(\omega+\Omega)t} - J_1(m)e^{i(\omega-\Omega)t}) \tag{8.3}$$

Note that this phase modulation has put sidebands onto the light which have a separation from the carrier of the modulation frequency and opposite phases (see Figure 8.4).

The beam is then incident on the Fabry-Perot cavity. Consider the part reflected by the cavity, this is

$$E_r = FE_t \tag{8.4}$$

where

$$F(\omega) = \frac{-r_1 + r_2(r_1^2 + t_1^2)e^{i\omega/\Delta\nu_{FSR}}}{1 - r_1 r_2 e^{i\omega/\Delta\nu_{FSR}}} \tag{8.5}$$

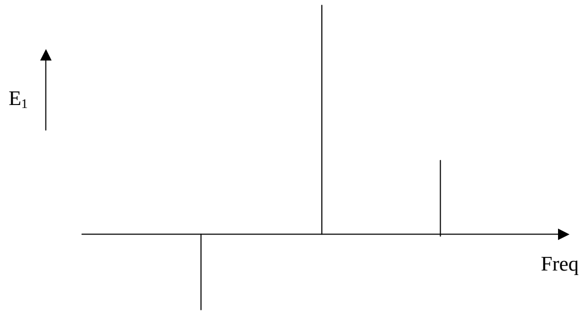

Figure 8.4: Carrier frequency with sidebands. The lower sideband is drawn below the line to emphasise the difference in phase between the two sidebands.

which can be found in optics text books.

Note that F is complex to accommodate any phase changes on reflection. For a symmetrical cavity, the reflection coefficients of the mirrors are equal $r = r_1 = r_2$ and assuming, also, that there is no absorption $(r_1^2 + t_1^2 = 1)$, this implies that

$$F(\omega) = \frac{r(e^{i\omega/\Delta\nu_{FSR}} - 1)}{1 - r^2 e^{i\omega/\Delta\nu_{FSR}}} \tag{8.6}$$

Each one of the three frequencies of light present must be multiplied by $F(\omega)$ and the results then added together, since the different light frequencies add linearly.

$$\begin{aligned} E_r = [F(\omega)J_0(m)e^{i\omega t} + F(\omega+\Omega)J_1(m)e^{i(\omega+\Omega)t} \\ -F(\omega-\Omega)J_1(m)e^{i(\omega-\Omega)t}]E_l \end{aligned} \tag{8.7}$$

However, the photodiode measures the power incident upon it. So we measure

$$P_r = E_r E_r^* \tag{8.8}$$

and also write

$$\begin{aligned} E_l E_l^* &= P_l & (8.9) \\ P_0 &= J_0^2(m) P_l & (8.10) \\ P_1 &= J_1^2(m) P_l & (8.11) \\ P_t &= E_t E_t^* & (8.12) \\ P_l &= P_0 + 2P_1 & (8.13) \end{aligned}$$

Therefore

$$\begin{align}
P_r &= E_r E_r^* \tag{8.14}\\
& \tag{8.15}\\
&= [E_l(F(\omega)J_0(m)e^{i\omega t} + F(\omega+\Omega)J_1(m)e^{i(\omega+\Omega)t} \nonumber\\
&\qquad\qquad\qquad + F(\omega-\Omega)J_1(m)e^{i(\omega-\Omega)t})] \nonumber\\
&\quad \times[E_l(F(\omega)^* J_0(m)e^{-i\omega t} + F^*(\omega+\Omega)J_1(m)e^{-i(\omega+\Omega)t} \nonumber\\
&\qquad\qquad\qquad - F^*(\omega-\Omega)J_1(m)e^{-i(\omega-\Omega)t})] \tag{8.16}\\
& \tag{8.17}\\
&= P_0|F(\omega)|^2 + P_1|F(\omega+\Omega)|^2 + P_1|F(\omega-\Omega)|^2 \nonumber\\
&\qquad + \sqrt{P_0P_1}\Big([F^*(\omega)F(\omega+\Omega) - F(\omega)F^*(\omega-\Omega)]e^{i\Omega t} \nonumber\\
&\qquad\qquad + [-F^*(\omega)F(\omega-\Omega) + F(\omega)F^*(\omega+\Omega)]e^{-i\Omega t}\Big) \nonumber\\
&\qquad - P_1[F(\omega+\Omega)F^*(\omega-\Omega) + F^*(\omega+\Omega)F(\omega-\Omega)e^{2i\Omega t}] \tag{8.18}
\end{align}$$

and neglecting 2Ω terms

$$\begin{align}
P_r &= P_0|F(\omega)|^2 + P_1\Big(|F(\omega+\Omega)|^2 + |F(\omega-\Omega)|^2\Big) \nonumber\\
&\quad + 2\sqrt{P_0P_1}\Big(\mathrm{Re}\Big[F(\omega)F^*(\omega+\Omega) - F^*(\omega)F(\omega-\Omega)\Big]\cos(\Omega t) \nonumber\\
&\qquad + \mathrm{Im}\Big[F(\omega)F^*(\omega+\Omega) - F^*(\omega)F(\omega-\Omega)\Big]\sin(\Omega t)\Big) \tag{8.19}
\end{align}$$

Multiplying this by a function proportional to the phase modulation signal and using $\cos\Omega t\sin\Omega t = 1/2\sin 2\Omega t$ and $\sin^2\Omega t = 1 - \cos^2\Omega t$, gives

$$\begin{align}
\epsilon' &= P_r\sin\Omega t \nonumber\\
&= P_0|F(\omega)|^2\sin\Omega t + P_1\Big(|F(\omega+\Omega)|^2 + |F(\omega-\Omega|^2\Big)\sin\Omega t \nonumber\\
&\quad + \sqrt{P_0P_1}\mathrm{Re}\Big[F(\omega)F^*(\omega+\Omega) - F^*(\omega)F(\omega-\Omega)\Big]\sin 2\Omega t \nonumber\\
&\quad + 2\sqrt{P_0P_1}\mathrm{Im}\Big[F(\omega)F^*(\omega+\Omega) - F^*(\omega)F(\omega-\Omega)\Big]\cos^2\Omega t \nonumber\\
&\quad - 2\sqrt{P_0P_1}\mathrm{Im}\Big[F(\omega)F^*(\omega+\Omega) - F^*(\omega)F(\omega-\Omega)\Big] \tag{8.20}
\end{align}$$

and putting this through a low pass filter to remove terms with frequency Ω and higher, gives an error signal of

$$\epsilon = -2\sqrt{P_0P_1}\mathrm{Im}\Big[F(\omega)F^*(\omega+\Omega) - F^*(\omega)F(\omega-\Omega)\Big] \tag{8.21}$$

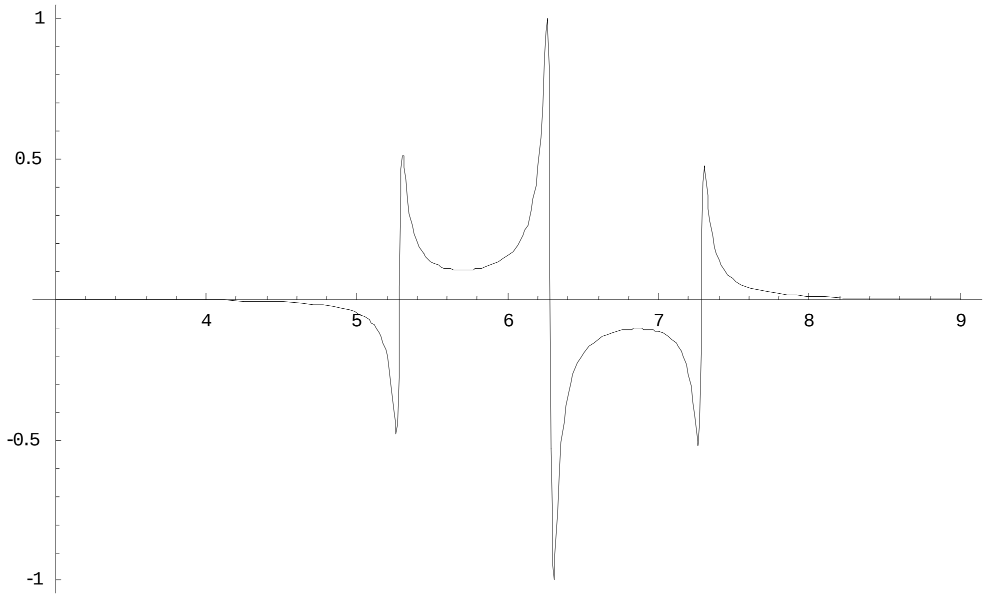

Figure 8.5: Error signal in the Pound Drever Hall method

ϵ is plotted for $[r = 0.99,\ \Omega = 1,\ \omega = 3\text{to}9]$ in Figure 8.5 as a function of ω.

Note that the error signal crosses zero when the carrier is resonant with the cavity. This is the lock point. Also note that the capture range is controlled by the modulation frequency since the error signal keeps the same sign until the frequency deviation reaches the modulation frequency.

In practice it is important to note that equation 8.21 may be multiplied by a phase shifted version of the phase modulation signal. A delay line may therefore be needed to be added to shift the phase back to that of the phase modulation signal. In the case that the phase is not properly matched between the two signals to be matched, the error signal will not have the desired shape.

Consider multiplying equation 8.21 by $\sin(\Omega t + \phi)$ and using

$$\cos \Omega t \sin(\Omega t + \phi) = 1/2 \sin 2\Omega t \cos \phi - \sin \phi \sin^2 \Omega t + \sin \phi \tag{8.22}$$

and

$$\sin \Omega t \sin(\Omega t + \phi) = \cos \Omega t \sin \Omega t \sin \phi - \sin \phi \cos^2 \Omega t + \cos \phi \tag{8.23}$$

Filtering out all terms with frequency Ωt or greater will give an error signal

$$\begin{aligned} \epsilon = {} & \sqrt{P_0 P_1}\,\mathrm{Im}\Big[F(\omega)F^*(\omega+\Omega) - F^*(\omega)F(\omega-\Omega)\Big]\sin\phi + \\ & \sqrt{P_0 P_1}\,\mathrm{Re}\Big[F(\omega)F^*(\omega+\Omega) - F^*(\omega)F(\omega-\Omega)\Big]\cos\phi \end{aligned} \tag{8.24}$$

This is plotted in Figures 8.6 and 8.7 for $\phi = 60^o$ and $\phi = 90^o$ respectively.

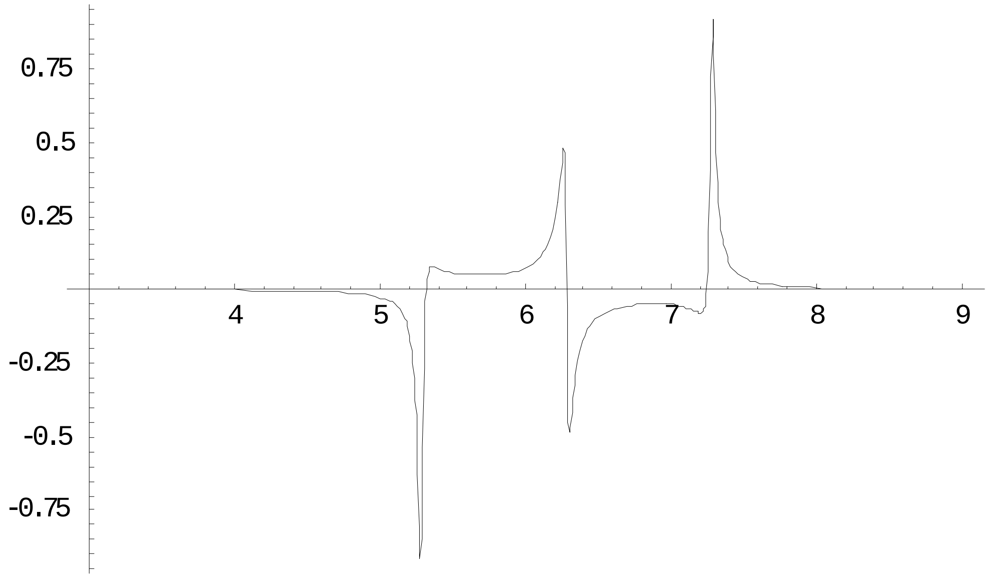

Figure 8.6: Error signal for phase mismatch of 60^o. Other parameters are the same as for Figure 8.5.

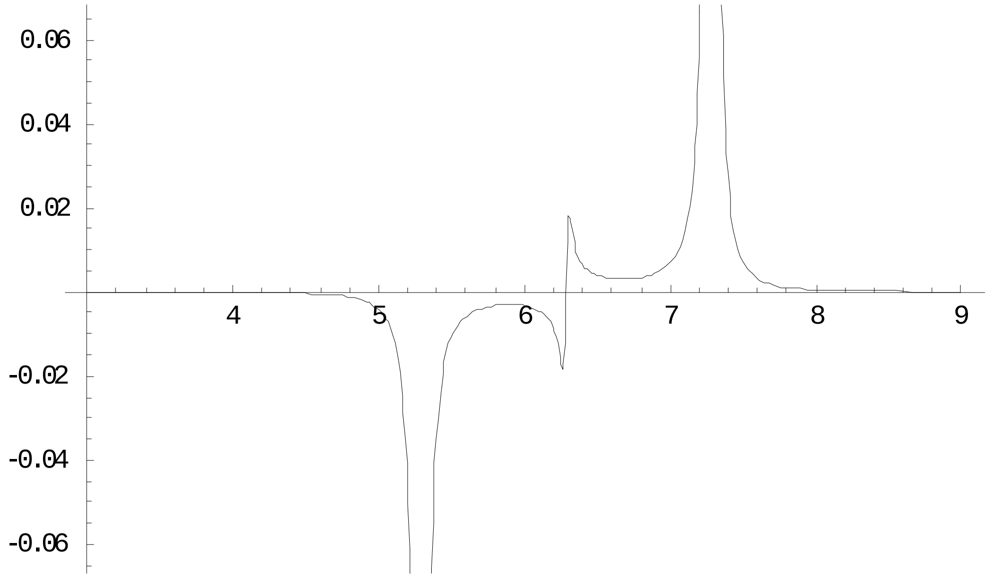

Figure 8.7: Error signal for complete phase mismatch of 90^o. Other parameters are the same as for Figure 8.5.

8.2.2 Phase in the Pound Drever Hall scheme

So far, the form of the error signal in the Pound Drever Hall scheme has been derived. I have, however, ignored a very useful feature of the scheme, which allows the linewidth to be narrowed considerably. The lock is very fast since it depends primarily on the light reflected from the front face of the cavity, known as the promptly reflected beam. Light incident on a Fabry-Perot cavity will be held inside it for a characteristic time. This decay time for the cavity is determined by the finesse (i.e. the reflectivity of the mirrors), and for a high finesse cavity the time is significant. For example, a finesse of ~ 300000 is obtained using mirrors of 99.999% reflectivity so for a 10cm cavity, the time to decay to $1/e$ is $\sim 30\mu s$ i.e. the cavity would not respond to frequency jitter above 30kHz.

The reflected beam consists of the sidebands, the promptly reflected beam and a beam of light leaked back out of the cavity. The sidebands are a long way from the resonance of the cavity so are almost completely reflected. On resonance, the reflected carrier and leakage beam are π radians out of phase and so interfere destructively. There would then only be a beat at 2Ω between the two sidebands and this is removed by the $2f$ filter. The phase of the reflected beam depends critically on which side of resonance the frequency is. Plotting the imaginary part of F gives the phase of the reflected beam. One can think of the laser beam (with its associated fast jitter of phase) being continually compared to the average phase of the stored light in the cavity via the leakage beam. The phase would then be a different sign depending on whether the frequency were above or below resonance.

8.2.3 Noise and stabilisation

Noise can in general be regarded as derived from one of two sources. The first is fundamental noise, which is linked to the laser mechanism and the nature of light. It is this noise which will ultimately limit the stability of any laser system, no matter how good the externally applied stabilisation is. Fundamental noise includes the shot noise and the noise due to spontaneous emission in the laser medium. The second source is technical noise, which is externally imposed on the system. This includes sources of frequency deviation such as vibrations in the lasing cavity. It is this noise which is corrected for by the stabilisation technique.

8.3 Experimental set-up of the Pound-Drever-Hall method

Work done with Stephen Webster during a three month stay at NPL is described in this section. During my time at NPL I built a second Pound-Drever-Hall lock for a Ti:Sapphire laser. The locking apparatus for the extant lock to a high finesse (~ 250000) cavity was realigned by me. I also built a second separate locking system with a cavity of finesse of 800 which could be used concurrently with the extant lock. The new locking system was to reduce the linewidth of the laser before the lock to the high finesse cavity. It was hoped that this would reduce the final linewidth of the laser.

An outline of the experimental setup for one lock is given below. The output of the laser was taken through a Faraday rotator to isolate the laser from back reflections from any of the locking apparatus. The light was then focussed down onto an AOM used in a double pass configuration. In this configuration the AOM had 50% efficiency for light in the $+1^{\text{st}}$ order after double pass. This AOM provided the frequency correction to the light. Some of this light was then picked off and focussed onto an EOM. The light was phase modulated at 10MHz to give sidebands on the light separated from the carrier by 10MHz. Two lenses were used to mode match into the Fabry-Perot cavity and the light reflected from the cavity was used to derive an error signal (Figure 8.8). The two mode matching lenses allowed the beam characteristics (i.e. waist size and position) to be controlled so as to only excite the TEM_{00} mode of the cavity.

8.3.1 The cavity

The cavity itself consisted of two mirrors, each with radius of curvature 0.35m and reflectance 99.6% giving a finesse of 800 ($F = \frac{\pi\sqrt{R}}{1-R}$). The spacer separating the two mirrors is a tube of Ultra Low Expansivity glass (ULE) 0.1m long and 0.035m in diameter. At one end, the mirror was glued on, at the other, the mirror was attached to piezo-electric transducers in a re-entrant design. Thus three piezos attach to the mirror and endplate and three attach to the endplate and spacer. This design allows much of the length change due to thermal expansion of the piezo stack to be cancelled out automatically. The cavity length (and hence resonant frequency) is tunable via the piezo-electric transducers.

The cavity rests on four viton pads, which in turn sit on a V-groove holder. The viton pads primarily insulate against thermal transfer. The whole cavity-holder system sits in a vacuum chamber. This is a home-made system made

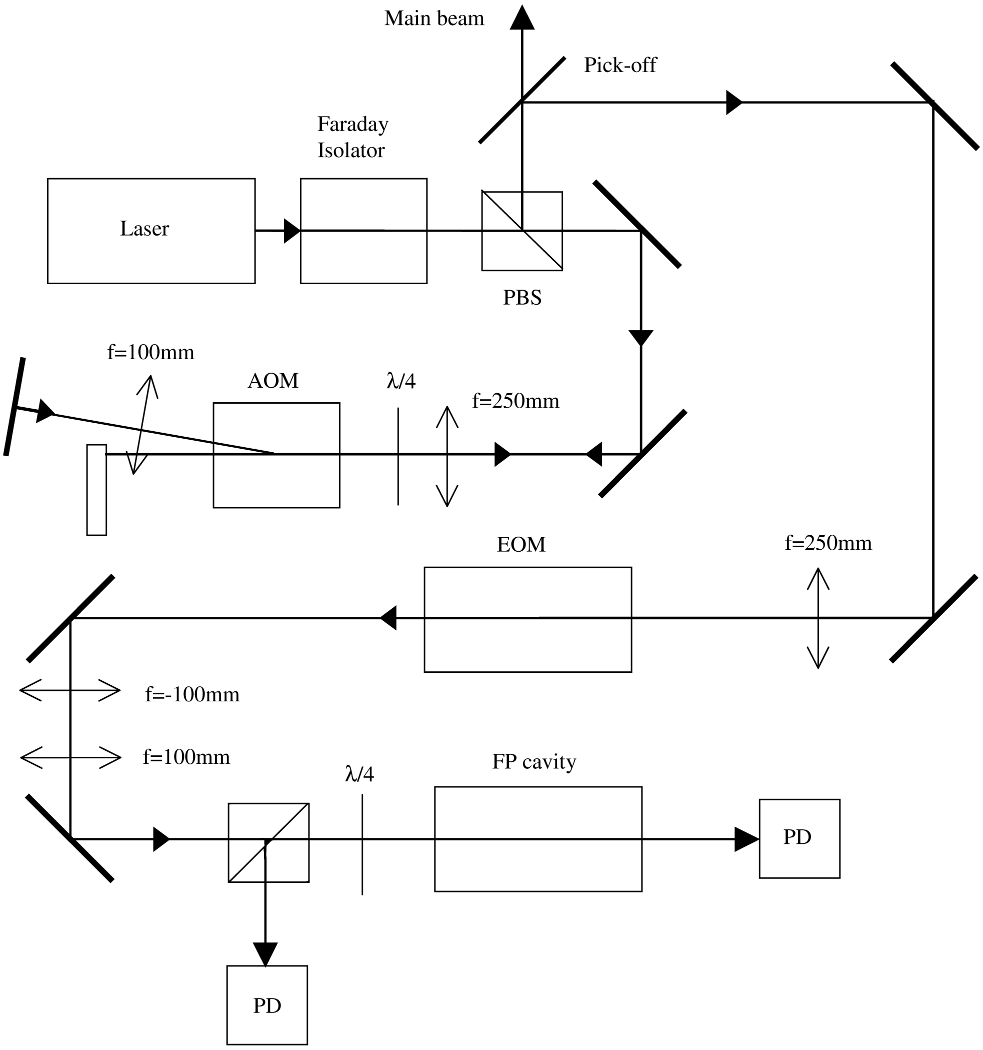

Figure 8.8: Schematic of the optical set-up used

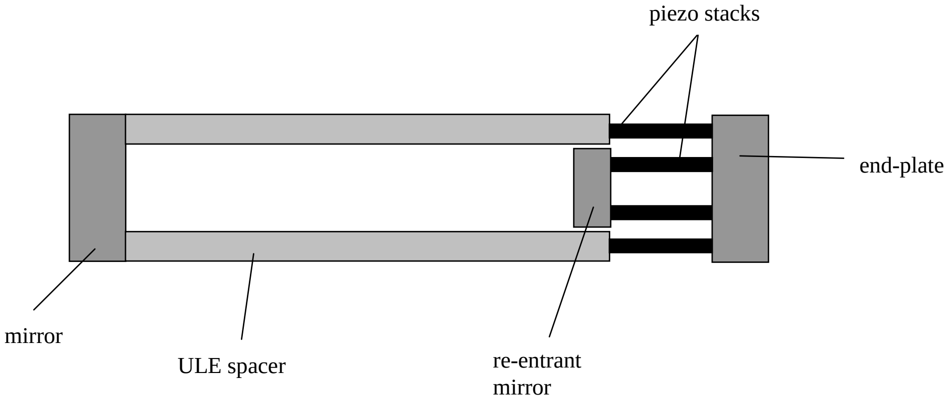

Figure 8.9: Design of the Fabry Perot cavity (only four out of six piezo-electric transducers shown for clarity

of Dural. The body of the vacuum chamber is a pipe of length 0.17m and outer diameter 0.15m, the wall thickness being 0.021m. The endplates are attached by M6 screws and the vacuum seal is made from indium wire. The cavity is maintained at a pressure below 10^{-5}mbar (3×10^{-6}mbar) by a miniature ion pump (Varian 2l/s).

The cavity and vacuum chamber are covered in a layer of thermal insulation and are actively temperature stabilised. The temperature control circuitry is home made and the circuits are shown in Figures 8.10 and 8.11.

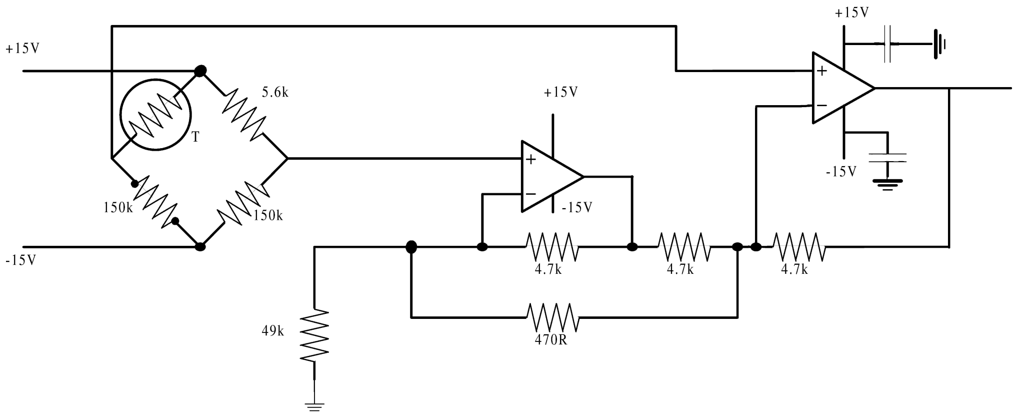

Figure 8.10: Circuit for the temperature sensor

The sensor circuit uses a thermistor (T) in a Wheatstone bridge circuit to produce a voltage which varies with temperature. This is amplified by the op-amps and is fed to the servo circuit. The servo circuit then compares this

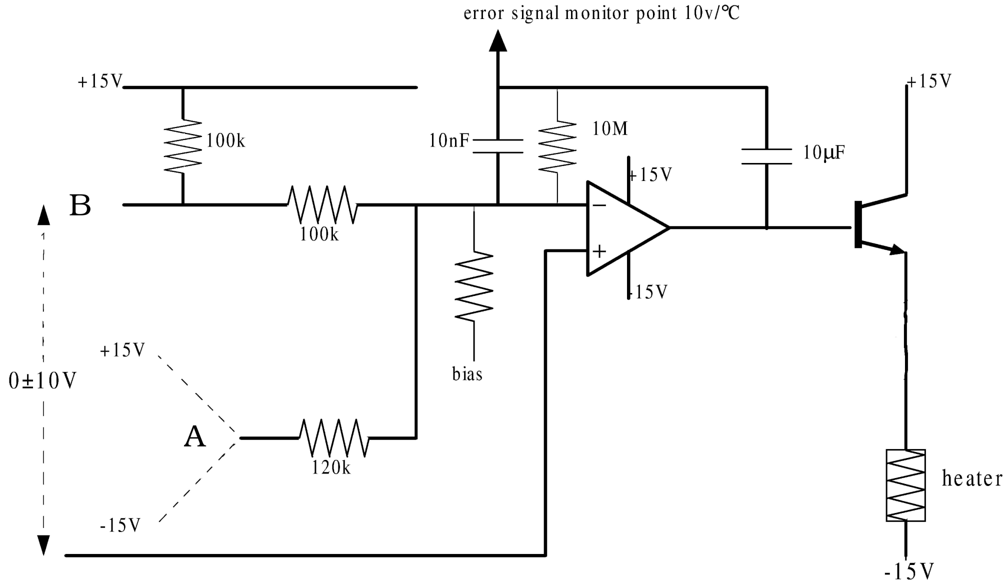

Figure 8.11: Servo circuit to control the temperature of the Fabry-Perot cavity. The set temperature is controlled by inputting a fixed voltage between +15V and -15V at A. The input from the sensor circuit is at B.

voltage to a reference voltage (adjustable to give a variable set temperature) and if the temperature of the thermistor is below the set temperature then current is forced through heater wire wrapped around the vacuum can to compensate.

8.3.2 The Acousto-Optic Modulator

The acousto-optic modulator (AOM) uses the Pound-Drever-Hall error signal and corrects for the frequency fluctuations present in the laser light. The AOM is made by Brimrose (model TEF-80-20). It shifts the frequency of the light by 80MHz with a potential bandwidth of 20 MHz (in practice the bandwidth is determined by the drive electronics and the delay in affecting the frequency due to the finite speed of sound in the medium). The AOM consists of a piezo-electric transducer connected to a crystal. The piezo vibrates at 80 MHz, setting up an acoustic wave in the crystal (i.e. a periodic pattern of compressed and rarefied material). Since the refractive index of the crystal depends on density, Bragg diffraction can occur from the wavefronts. Since the wavefronts are moving, the reflected light is Doppler shifted, hence the change in frequency. By controlling the frequency of the piezo, the energy transferred can be changed so as to tune the frequency of the light.

The AOM is used in a double pass configuration. This serves to reduce the change in beam direction as the light is frequency shifted. In single pass, the light in the first order is deflected by an amount which is dependent on the shift. If the light exiting the AOM is reflected back along its path into the AOM then the frequency is shifted again in the same direction, but the direction of propagation is deflected so as to counterpropagate with the incident beam. Since the double passed beam is always colinear to the incident beam, the direction of the shifted beam is independent of the frequency shift. To maximise the efficiency of the AOM, the incident beam is focussed into the AOM.

8.3.3 Servo-electronics

The layout for the servo (locking) electronics for extracting and applying the error signal is shown in Figure 8.12. The local oscillator (LO) was a

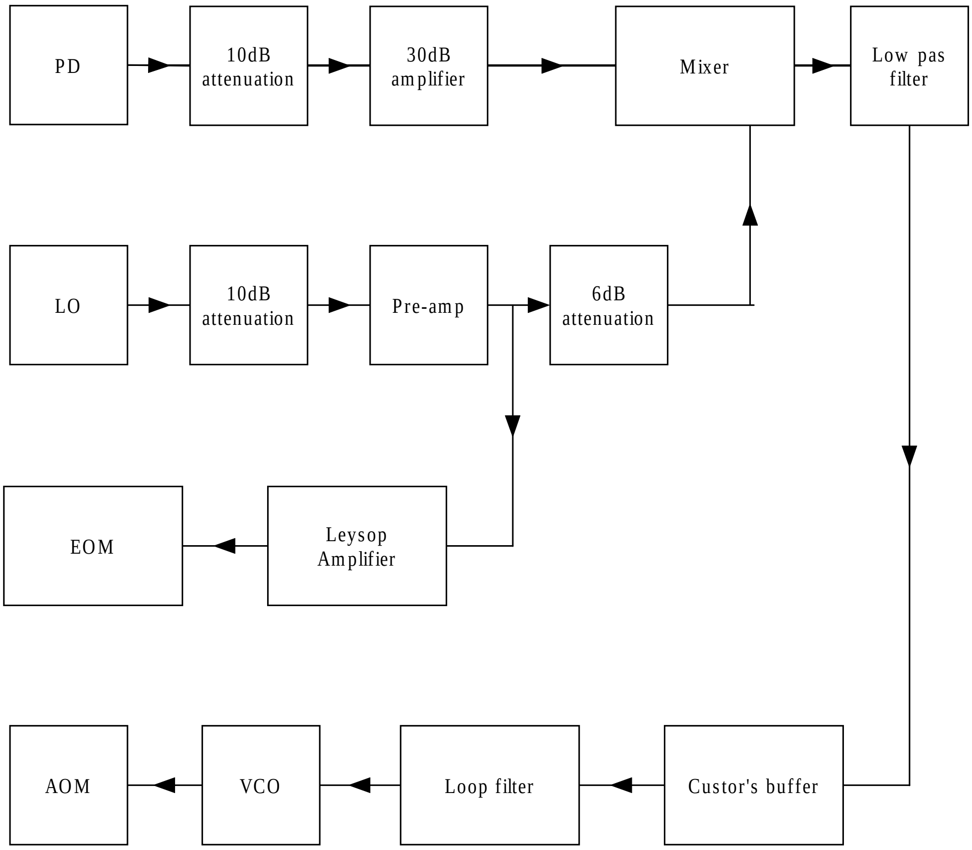

Figure 8.12: Schematic of the locking electronics

Novatech DDS3 source which produces a pure sine wave output. This drives the electro-optic modulator (EOM Linos PM25). The mixer (Mini-circuits ZRPD-1) multiplied the local oscillator signal by the photodiode signal. The optimum phase difference ($\pi/2$) between the two signals was achieved by adding lengths of co-axial cable into the local oscillator path as a delay line. The low pass filter (Mini-circuits) removed any interference signal at twice the local oscillator frequency. The home-made loop filter amplifies the error signal. The loop filter was developed from a design from the original Drever-Hall paper [100].

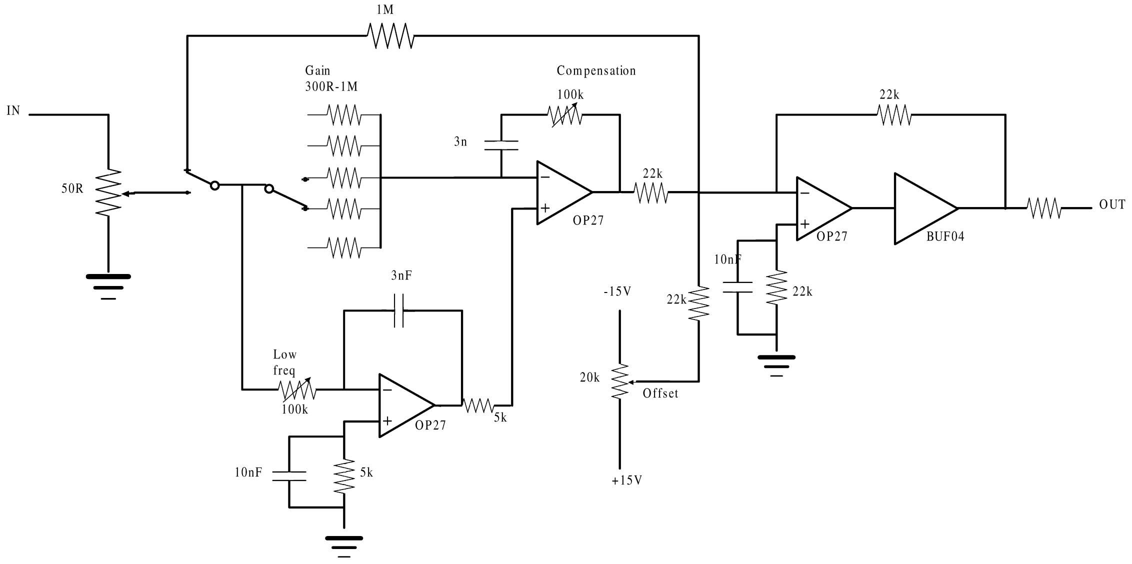

Figure 8.13: Loopfilter with bypass topology.

The circuit diagram for the loop filter is shown in Figure 8.13. This system (known as having bypass rather than cascade topology) allows the high frequency excursions of the laser from the set point to be dealt with quickly, whilst the low frequency excursions can have a much larger gain. This is necessary since low frequency noise has a much larger effect on the linewidth [100]. The high frequency amplifier (compensation) has one input coming directly from the signal and the other (acting as AC ground) from the low frequency amplifier.

The attenuators and amplifiers (MAN-1LN) were all from Mini-circuits. Custor's buffer was home-made and serves to allow equipment (in this case the mixer) which cannot drive a 50Ω load to drive a 50Ω load (in this case the loop filter).

8.4 Results

8.4.1 Laser stabilisation at NPL

The error signal obtained from the work at NPL, with the cavity of 800 finesse, is shown in Figure 8.14 (top trace). The bottom trace shows the transmission of the cavity. The small sidebands imposed on the laser are too small to be made out on this trace. Since the cavity has a relatively low finesse and the sidebands are at a comparable frequency to the linewidth, the error signal appears broader than that calculated for a high finesse cavity and the carrier and sideband peaks are blended together. This does not alter the signal qualitatively. To obtain this trace, the laser was scanned over the cavity resonance. When the laser is locked, it is not scanning.

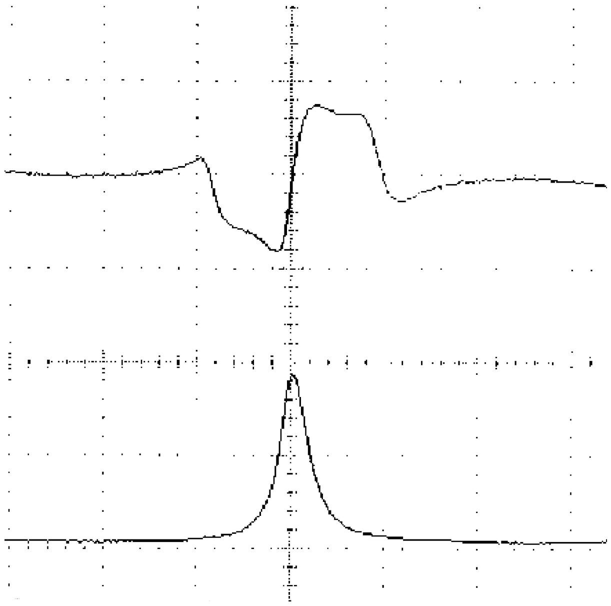

Figure 8.14: Pound-Drever-Hall error signal (top) and transmission of carrier and sidebands (bottom) obtained at NPL with the cavity of 800 finesse. The sidebands are 10MHz away from the carrier.

By use of the variable resistors in the loop filter, the amplification of the error signal can be altered. This changes the steepness of the locking slope and so the tightness of the laser lock can be controlled. For a very weak lock, the laser is effectively free running and no reduction in linewidth is observed. Figure 8.15 shows a Fast Fourier Transform of the error signal. This provides a measure of the amount of noise on the laser, since deviations in frequency will cause the error signal to change. The upper trace shows the noise spectrum for the weakly locked laser from 0 to 102.4kHz. Note the high noise at low frequency and the sharp feature at 82kHz. This feature is due to an internal dither within the laser which is utilised for its own preliminary lock. A subharmonic of this feature is visible at around 40kHz. The lower trace shows the noise reduction possible for optimum gain settings within the loop filter. The gain on the error signal can be set independently for different frequency ranges by using the variable resistors in Figure 8.13. The reduction is roughly 10dB at high frequency rising to upwards of 60dB approaching DC (see Figure 8.16).

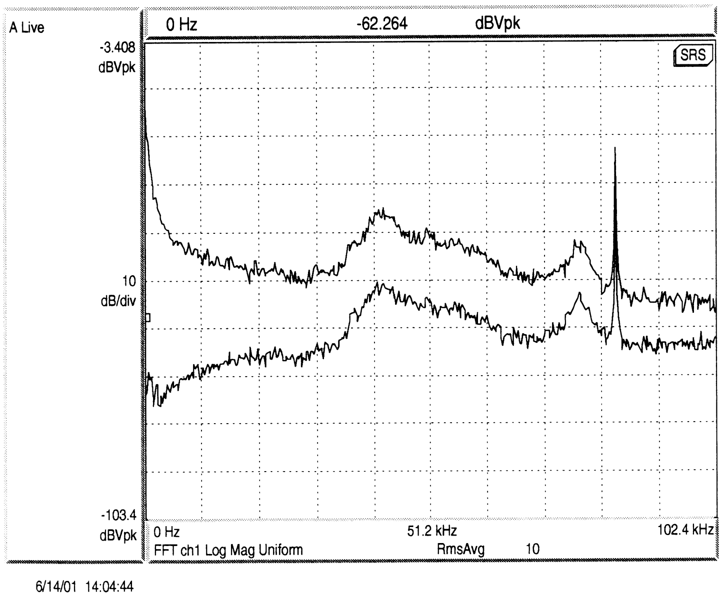

Figure 8.15: Fast Fourier Transform of the error signal with a weak lock (top) and a strong lock (bottom), 0-102.4kHz.

An alternative method of inspecting the lock is to observe the beat frequency on the photodiode of the carrier and sidebands. As can be seen from Figure 8.17, the beat signal of 10MHz is clearly visible when the lock is very weak. This corresponds to a portion of the carrier being reflected from the cavity as well as the sidebands. Figure 8.18 shows the Fourier transform of the photodiode signal around the same frequency but with a strong lock. The beat between the carrier and sidebands is 30dB smaller, since the carrier is locked to the centre of the peak of the Airy function. This corresponds to almost complete transmission of the carrier so the beat signal is much reduced.

If the gain on the lock is increased too much then the laser frequency will

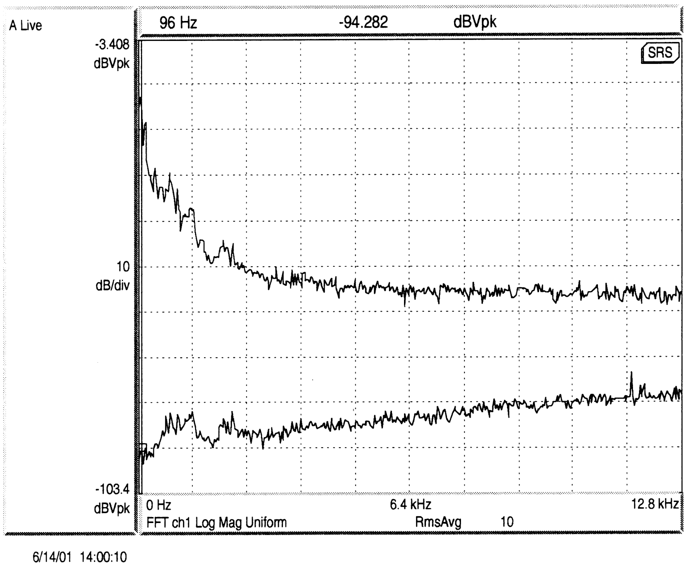

Figure 8.16: Fast Fourier Transform of the error signal with a weak lock (top) and a strong lock (bottom), 0-12.8kHz

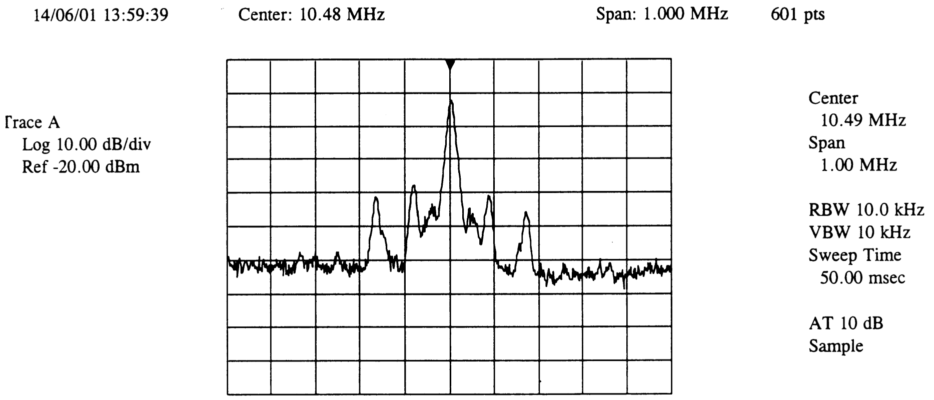

Figure 8.17: Fourier transform of the beat signal from a weak lock. The centre of the graph is at 10.49MHz and the width of the graph is 1MHz.

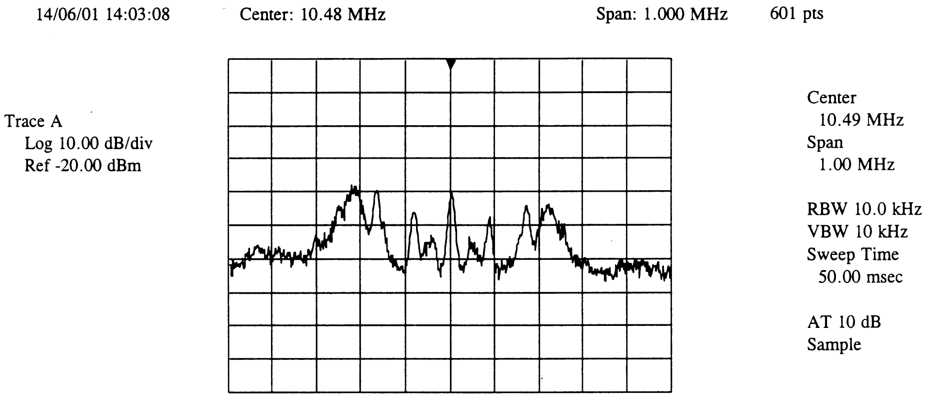

Figure 8.18: Fourier transform of the beat signal from a good lock. The centre of the graph is at 10.49MHz and the width of the graph is 1MHz.

oscillate. This can be seen in Figure 8.19, the large peaks at 250kHz corresponding to the oscillation of the laser frequency and implying a bandwidth of the lock below this value. It is believed that the bandwidth may be limited by the time taken for the acoustic wave to propagate from the transducer to the position of the laser beam through the crystal in the AOM [102].

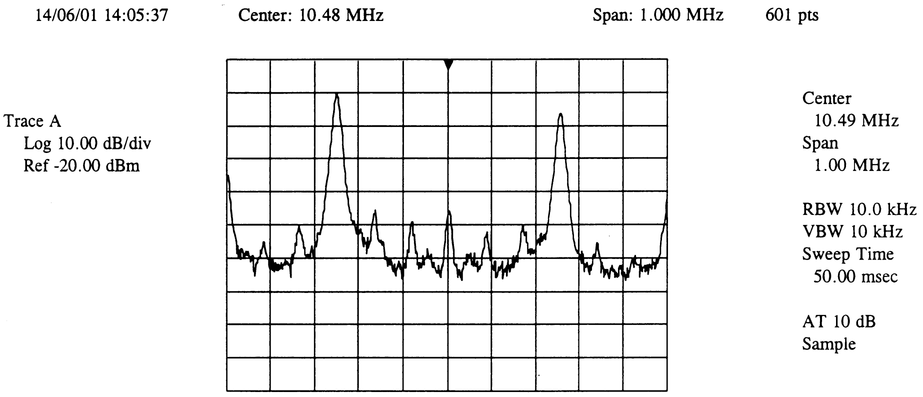

Figure 8.19: Fourier transform of the beat signal from a very strong lock leading to oscillation. The centre of the graph is at 10.49MHz and the width of the graph is 1MHz.

The oscillation arises as a general result from servo-control theory. The lock has a certain gain at any particular frequency. To explain how this leads to instability at high gains, consider a bode plot (log-log plot of gain against frequency) for an op-amp. The gain will be constant up to a given frequency, after which it will begin to roll off. This roll off is an artefact of the op-amp behaving like an RC low pass filter (the gain drops as $1/f$). As each stage of the amplifier rolls off then an extra 6dB/octave is added to the drop off in gain. There is also a phase shift associated with each roll off. At each roll off, the response shifts by $\pi/2$. If the phase shift is π at the point where the gain crosses the axis (i.e. at unity gain) then any fluctuations will build up rather than be damped down. The servo system then drives the system with positive feedback. The transmitted light intensity will drop in this case. For more detailed information see [103].

8.4.2 Measurement of the absolute linewidth of a Ti:Sapphire laser at NPL

After my association with NPL, P Blythe and S Webster did an experiment to measure the absolute linewidth of the Ti:Sapphire laser with two Pound-Drever-Hall locks. The work is as yet unpublished, but follows closely the method taken in [102] which was done on the same laser with a single lock. Their experiment used a ^{171}Yb^{+} ion in an rf trap. The overall goal of their project is to create a frequency standard based on the S$_{1/2}$-F$_{7/2}$ transition at 467nm in this ion. This octupole transition has an extremely long lifetime (estimated $\sim$ 10 years) and so may make an extremely accurate frequency standard. A possible accuracy of parts in 10^{18} is claimed.

The narrow linewidth of the S$_{1/2}$-F$_{7/2}$ transition means that it can be used as an excellent discriminator to measure the laser linewidth (which will be many times larger than the linewidth of the transition). The Yb^{+} ion was trapped and laser cooled. The 934nm light from the Ti:Sapphire laser was frequency doubled and used to drive the S$_{1/2}$-F$_{7/2}$ transition. As the laser was stepped over the transition in steps of 400Hz, the transition probability was monitored by a quantum jump technique. This procedure was repeated many times. The probability of excitation at each step was plotted to give a line profile for the laser. It was found that the double locked laser displayed the same linewidth as the single locked laser (2.3kHz). This was in spite of the fact that each lock taken singly seemed to stabilise the output of the laser considerably. It is postulated that the limit on the final linewidth of the locked laser is not the comparatively unstable ($\sim$ 100kHz) beam of the unlocked laser, but environmental effects such as vibration of the cavity.

8.4.3 Laser stabilisation at IC

After setting up a Pound-Drever-Hall lock at NPL, I repeated a similar scheme for locking a Ti:Sapphire laser at IC. This laser is to be used for future experiments in the group on sideband cooling and finally on decoherence studies in a Penning trap. The wavelength of the laser is 729nm and it will drive the $S_{1/2}$-$D_{5/2}$ transition in Ca^+.

The laser to be stabilised is a Coherent MBR-110. This was pumped by a frequency doubled YAG laser with maximum output power of 5W (Coherent Verdi). The Ti:Sapphire laser itself consists of a laser cavity in a bow tie configuration. This was built into a monolithic block of aluminium and single mode operation is ensured by incorporation of a uni-directional device. There is a thin etalon in the cavity to provide coarse tuning of the laser wavelength. The laser is locked both to the etalon and to a temperature-stabilised cavity (with invar spacers) which is provided as part of the laser. When the laser is correctly locked, its linewidth (in the 'off the shelf' state) is claimed to be around 100kHz (although in reality probably nearer to 1MHz).

The Fabry-Perot cavity for the external Pound-Drever-Hall lock has a nominal finesse of 250 000 as quoted by the manufacturers (REO). It was manufactured by optically contacting the high reflectance mirrors (radius of curvature 0.35m) onto a ULE spacer of length 0.1m. The cavity was placed in a home made vacuum can and evacuated to 1.5×10^{-6} mbar (as at NPL). The cavity was temperature stabilised in a manner similar to that at NPL, using a home made control circuit (Figures 8.10 and 8.11). The AOM, VCO and EOM were as described for NPL. The local oscillator was a signal generator (HP 8643A) which gave 91mV output. This was amplified by an ENI 300L amplifier to 13V. In turn this was input to a homemade transformer (air core) which acted as a tuned circuit with a resonance at 6.137MHz. This gave an output voltage of 400V which was fed to the EOM. The loop filter was home made as at NPL.

As described, this equipment produced an error signal which is shown in Figure 8.20. Noise at a frequency of 22kHz was present on the error signal. This is the high frequency jitter observable in Figure 8.20. It is believed that this noise is stopping the laser from locking to the cavity. As yet, the source of the noise is not known.

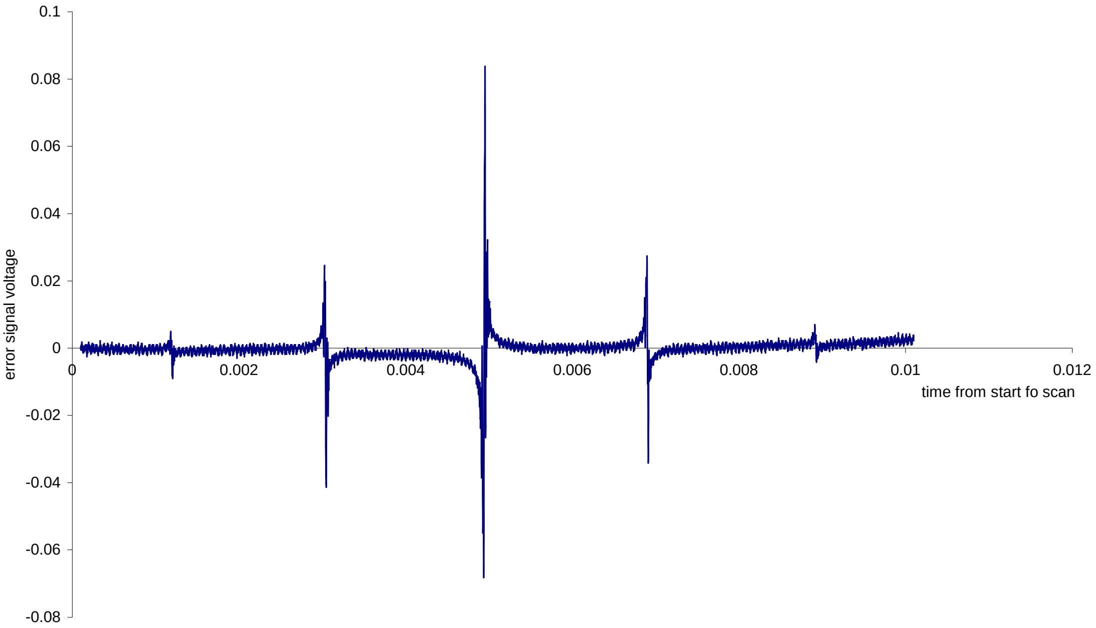

Figure 8.20: Pound-Drever-Hall error signal as produced with the high finesse cavity at IC. The frequency difference between the carrier and sidebands is 6MHz.

Chapter 9

Conclusion

The work described in this thesis has gone a considerable distance to set the stage for the rest of the project. Much of my work has been to build up the equipment for a system that can achieve the eventual goal of studying decoherence in a Penning trap. The decoherence inherent in a Penning trap may be less than that for rf traps which have been studied elsewhere.

We have demonstrated laser cooling of Ca^+ ions in a Penning trap. This is only the third ion for which this has been achieved, and it is noteworthy that both of the ions previously cooled had a level structure which facilitates laser cooling in a manner which Ca^+ does not. Ca^+ was chosen for our future work since the lasers needed to address the ion are all solid state, and the ion also has a metastable excited state that can be used for the qubit transition. In order to operate the Penning trap, it was found necessary to gain experience with the equipment first using a Paul trap. The Paul trap is easier to operate since it requires fewer lasers to laser cool the ion properly in the absence of a large magnetic field. Our method was then to increase the magnetic field incrementally, trapping in a combined Paul/Penning trap. Once a high enough field was reached the trap could be switched to a pure Penning trap.

Simulations of laser cooling in a four level species have been presented. This system was chosen to mimic certain aspects of the structure of Ca^+ ions in a magnetic field. In particular optical pumping was considered as two cooling lasers were used.

Two Pound Drever Hall locking systems were built. Work on one was done on a Ti:Sapphire laser system at NPL, where they planned to test the effect on the linewidth of a double lock. A second similar system was built from scratch at IC to narrow the linewidth of Coherent Ti:Sapphire laser.

Future work on the Penning trap is detailed in Section 7.2.4 and includes locking the lasers to cavities and building a more accurate wavemeter. It is hoped this will allow a single Ca$^+$ ion to be trapped and laser cooled in a Penning trap. Further in the future, a superconducting magnet will be used in the trap. This will give a much more stable magnetic field than the current conventional magnet. It will be necessary to have this more stable field to do sideband cooling and measure decoherence in the motional states. Development of the narrow linewidth Ti:Sapphire laser will continue, with the goal of locking it to the high finesse cavity in order to perform sideband cooling.

Appendix A

Visual Basic code for calculating Voigt profiles

Below is the macro to define a function ‘Voigt’ for Excel which calculates the integral of ‘fun1(x)’.

```
Function Integral (a, b, n)
If Int(n/2)*2<>n Then n=n+1
h=(b-a)/n
p=fun1(a) + fun1(b)
z=4
For r=1 To n-1
p=p + z * fun1(a+r*h)
z=6-z
Next
Integral=h*p/3
End function
```

Defining Fun1

```
Fun1 = Gaussian2(x, alpha, widthgauss)*Lorentzian2(x,widthlorentz)
```

where

```
Gaussian2 = 2/widthgauss*0.4679*Exp(-0.693*(2*(alpha-x)/widthgauss)^2)
```

and

```
Lorentzian2 = 2/(3.14159*widthlorentz)*1/(1+(2*x/widthlorentz)^2)
```

defines the function Voigt in Excel with parameters

—a— lower integration limit
—b— upper integration limit
—n— number of strips
—widthgauss— FWHM of Doppler broadened width
—widthlorentz— FWHM of natural lineshape
—alpha— is the position on the Voigt profile.

Bibliography

[1] R Feynman *Int J Theor Phys* **21** 467 (1982)

[2] R Feynman *Found Phys* **16** 507 (1986)

[3] P Benioff *J Stat Phys* **22** 563 (1980)

[4] P Benioff *J Stat Phys* **29** 515 (1982)

[5] J I Cirac and P Zoller *Phys Rev Lett* **74** 4091 (1995)

[6] A Steane *Phys Rev Lett* **77** 793 (1996)

[7] P W Shor *Phys Rev A* **52** R2493 (1995)

[8] C Monroe, D M Meekhof, B E King, S R Jefferts, W M Itano and D J Wineland *Phys Rev Lett* **75** 4091 (1995)

[9] R W Hamming *Coding and information Theory* Prentice Hall (1986)

[10] L Szilard *Z Phys* **53** 840 (1929)

[11] C H Bennett *Int J Theor Phys* **21** 905 (1982)

[12] R Landauer *IBM J Res Dev* **5** 183 (1961)

[13] A Church *Am J Math* **58** 345 (1936)

[14] A Turing *Proc Lond Math Soc Ser* **43** 544 (1936)

[15] D Deutsch *Int J Theor Phys* **24** 1 (1985)

[16] D Deutsch *Proc R Soc A* **425** 73 (1989)

[17] D Deutsch *Proc R Soc A* **400** 97 (1985)

[18] S Lloyd *Science* **273** 1073 (1996)

[19] C Zalka *Proc R Soc Lond A* **454** 313 (1998)

[20] B M Boghosian and W Taylor *Physica D* **120** 30 (1998)

[21] L K Grover *Phys Rev Lett* **79** 325 (1997)

[22] P W Shor *Proc 35th Ann Symp on Found of Comp Sci* (1994)

[23] M B Plenio and P L Knight *Phys Rev A* **53** 2986 (1996)

[24] J Preskill *Quantum information and computation* available at http://www.theory.caltech.edu/ preskill/ph229

[25] R Laflamme, E Knill, D G Cory, E M Fortunato, T Havel, C Miquel, R Martinez, C Negrevergne, G Oritz, M A Pravia, Y Sharf, S Sinha, R Somma and L Viola *arXiv:quant-ph/0207172*

[26] N A Gershenfeld and I L Chuang *Science* **275** 350 (1997)

[27] J Zhang, Z Lu, L Shan and Z Deng *arXiv:quant-ph/0208102*

[28] T Pellizari, S A Gardiner, J I Cirac and P Zoller *Phys Rev Lett* **75** 3788 (1995)

[29] R Rucker *Mind Tools* Penguin Books (1988)

[30] L M K Vandersypen, M Steffen, G Bretya, C S Yannoni, M H Sherwood and I L Chuang *Nature* **414** 883 (2001)

[31] F M Penning *Physica* **3** 873 (1936)

[32] E R Harrison *Am J Phys* **27** 314 (1959)

[33] P K Ghosh *Ion Traps* Clarendon Press (1995)

[34] R C Thompson and D C Wilson *Z Phys D* **42** 271 (1997)

[35] L S Brown and G Gabrielse *Rev Mod Phys* **58** 233 (1986)

[36] N W McLachlan *Theory and applications of Mathieu functions* Clarendon Press (1947)

[37] H G Dehmelt *Adv At Mol Phys* **3** 53 (1967)

[38] M A Rowe, A Ben-Kish, B Demarco, D Leibfried, V Meyer, J Beall, J Britton, J Hughes, W M Itano, B Jelenkovic, C Langer, T Rosenband and D J Wineland *Quantum Information and Computation* **2** 4 257 (2002)

[39] C F Roos, D Leibfried, A Mundt, F Schmidt-Kaler, J Eschner, R Blatt *Phys Rev Lett* **85** 5547 (2000)

[40] C J S Donald, D M Lucas, P A Barton, M J McDonnell, J P Stacey, D A Stevens, D N Stacey and A M Steane *Europhys Lett* **51** 388 (2000)

[41] J D Prestage, G J Dick and L Maleki *J Appl Phys* **66** 1013 (1989)

[42] Ch Roos, Th Zeiger, H Rohde, H C Nagerl, J Eschner, D Leibfried, F Schmidt-Kaler and R Blatt *Phy Rev Lett* **83** 4713 (1999)

[43] M J McDonnell, J P Stacey, D A Stevens, D N Stacey and A M Steane physics/0003085

[44] D J Heinzen and D J Wineland *Phys Rev A* **42** 2977 (1990)

[45] B E King, C S Wood, C J Myatt, Q A Turchette, D Leibfried, W M Itano, C Monroe and D J Wineland *Phys Rev Lett* **81** 1525 (1998)

[46] G Morigi, J Eschner and C Keitel *Phys Rev Lett* **85** 4458 (2000)

[47] C F Roos, D Leibfried, A Mundt, F Schmidt-Kaler, J Eschner and R Blatt *Phy Rev Lett* **85** 5547 (2000)

[48] H Rohde, S T Gulde, C F Roos, P A Barton, D Leibfried, J Eschner, F Schmidt-Kaler amd R Blatt *J Opt B* **3** S34 (2001)

[49] D Kielpinski, C Monroe, D J Wineland *Nature* **417** 709 (2002)

[50] H G Dehmelt *Adv Atom Mol Phys* **5** 109 (1969)

[51] M H Holzscheiter *Physica Scripta* **T22** 73 (1988)

[52] J Andre *J Physique* **37** 719 (1976)

[53] D J Larson, J C Bergquist, J J Bollinger, W M Itano and D J Wineland *Phys Rev Lett* **57** 70 (1986)

[54] T W Hänsch and A L Schawlow *Opt Commun* **13** 68 (1975)

[55] D J Wineland and H G Dehmelt *Bull Am Phys Soc* **20** 637 (1975)

[56] S Stenholm *Rev Mod Phys* **58** 699 (1986)

[57] F Diedrich, J C Bergquist, W M Itano and D J Wineland *Phys Rev Lett* **62** 403 (1989)

[58] H C Nagerl D Leibfried, H Rohde, G Thalhammer, J Eschner, F Schmidt-Kaler and R Blatt *Phys Rev A* **60** 145 (1999)

[59] C Monroe, D M Meekhof, B E King, W M Itano and D J Wineland *Phys Rev Lett* **75** 4714 (1995)

[60] S Gulde, H Haffner, G Lancaster, A Mundt, A Kreuter, C Russo, C Bechner, F Schmidt-Kaler, I L Chuang and R Blatt *Proc ICAP* (2002)

[61] C Monroe, D Leibfried, B E King, D M Meekhof, W M Itano, D J Wineland *Phys Rev A* **55** R2489 (1997)

[62] D J Wineland, C Monroe, W M Itano, B E King, D Leibfried, D M Meekhof, C Myatt and C Wood *Fortschr Phys* **46** 363 (1998)

[63] B DeMarco, A Ben-Kish, D Leibfried, V Meyer, M Rowe, B M Jelenkovic, W M Itano, J Britton, C Langer, T Rosenband and D J Wineland *quant-ph/0208180*

[64] J F Poyatos, J I Cirac and P Zoller *Phys Rev Lett* **81** 1322 (1998)

[65] A Sørensen and K Mølmer *Phys Rev Lett* **82** 1971 (1999)

[66] D Jonathan, M B Plenio and P L Knight *Phy Rev A* **62** 042307 (2000)

[67] D Jonathan and M Plenio *Phys Rev Lett* **87** 127901 (2001)

[68] A Beige *quant-ph/0205070*

[69] Q A Turchette, C S Wood, B E King, C J Myatt, D Leibfried, W M Itano, C Monroe and D J Wineland *Phys Rev Lett* **81** 3631 (1998)

[70] K Mølmer and A Sørensen *Phys Rev Lett* **82** 1835 (1999)

[71] C A Sackett, D Kielpinski, B E King, C Langer, V Meyer, C J Myatt, M Rowe, Q A Turchette, W M Itano, D J Wineland and C Monroe *Nature* **404** 256 (2000)

[72] C K Law and J H Eberly *Phys Rev Lett* **76** 1055 (1996)

[73] A Ben-Kish, B DeMarko, V Meyer, M Rowe, J Britton, W M Itano, B M Jelenkovic, C Langer, D Leibfried, T Rosenband and D J Wineland *quant-ph/0208181*

[74] A B Mundt, A Kreuter, C Becher, D Leibfried, J Eschner, F Schmidt-Kaler and R Blatt *Phys Rev Lett* **89** 103001 (2002)

[75] D Kielpinski, C Monroe and D J Wineland *Nature* **417** 709 (2002)

[76] M A Rowe, A Ben-Kish, B DeMarco, D Leibfried, V Meyer, J Beall, J Britton, J Hughes, W M Itano, B Jelenkovic, C Langer, T Rosenband and D J Wineland *Quant Inf and Comp* **2** 257 (2002)

[77] D P DiVincenzo *Phys Rev A* **51** 1015 (1995)

[78] A Steane *Rep Prog Phys* **61** 117 (1998)

[79] D P DiVincenzo *Phys Rev A* **51** 1015 (1995) table 1

[80] S Urabe, M Watanabe, H Imajo and K Hayasaka *Opt Lett* **17** 1140 (1992)

[81] C Roos, T Zeiger, H Rohde, H C Nagerl, J Eschner, D Leibfried, F Schmidt-Kaler and R Blatt *Phys Rev Lett* **83** 4713 (1999)

[82] Q A Turchette, D Kielpinski, B E King, D Leibfried, D M Meekhof, C J Myatt, M A Rowe, C A Sackett, C S Wood, W M Itano, C Monroe and D J Wineland

[83] D J Wineland, C Monroe, W M Itano, B E King, D Leibfried, D M Meekhof, C Myatt and C Wood *Fortschr Phys* **46** 363 (1998) *Phys Rev A* **61** 063418 (2000)

[84] D Kielpinski, V Meyer, M A Rowe, C A Sackett, W M Itano, C Monroe and D J Wineland *Science* **291** 1013 (2001)

[85] X P Huang, J J Bollinger, T B Mitchell and W M Itano *Phys of Plasmas* **5** 1656 (1998)

[86] D M Meekhof, C Monroe, B E King, W M Itano and D J Wineland *Phys Rev Lett* **76** 1796 (1996)

[87] R C Thompson *Adv in At Mol and Opt Phys* **31** 63

[88] D J Wineland, C Monroe, W M Itano, D Liebfried, B King, D M Meekhof *Journal of Research of the National Institute of Standards and Technology* **103** 259 (1998)

[89] J J Bollinger, J N Tan, W M Itano, D J Wineland and D H E Dubin *Physica Scripta* **T59** 352 (1995)

[90] H F Powell, D M Segal, R C Thompson *Phys Rev Lett* **89** 093003 (2002)

[91] H C Nagerl, C Roos, D Liebfried, H Rohde, G Thalhammer, J Eschner, F Schmidt-Kaler, R Blatt *Phys Rev A* **61** 023405 (2000)

[92] P A Barton, C J S Donald, D M Lucas, D A Stevens, A M Steane, D N Stacey *Phys Rev A* **62** 032503 (2000)

[93] Private communication with R Learner

[94] L Ricci, M Weidemüller, T Esslinger, A Hemmerich, C Zimmermann, V Vuletic, W König, T W Hänsch *Opt Comm* **117** 541 (1995)

[95] A S Arnold, J S Wilson and M G Boshier *Rev Sci Inst* **69** 1236 (1998)

[96] D J Bate *PhD Thesis* p156 (1991)

[97] C Donald *PhD thesis* Oxford (2000)

[98] K Dholakia, G Z K Horvath, D M Segal, R C Thompson *J Mod Opt* **39** 2179 (1992)

[99] T W Hänsch and B Couilland *Opt Comm* **35** 441 (1980)

[100] R W P Drever, J L Hall, F V Kowalski, J Hough, G M Ford, A J Munley and H Ward *Appl Phys B* **31** 97 (1983)

[101] R V Pound *Rev Sci Instrum* **17** 490 (1946)

[102] S A Webster, P Taylor, M Roberts, GP Barwood and P Gill *Phys Rev A* **65** 052501 (2002)

[103] P Horowitz and W Hill *The Art of Electronics* p244